CHEMICAL REVIEWS

pubs.acs.org/CR

Open Access

This article is licensed under CC-BY-NC-ND 4.0

Review

Overcoming the Charge Confinement-Transport Trade-Off in Perovskite Light-Emitting Diodes

Published as part of Chemical Reviews special issue "Emerging Energy Materials: Halide Perovskites".

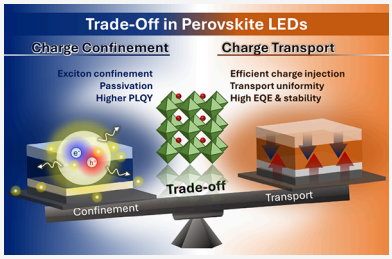
Kyung Yeon Jang, Bo-Hyun Choi, Kyoo-Hyung Lee, Chan-Yul Park, Qingsen Zeng, and Tae-Woo Lee*

Cite This: https://doi.org/10.1021/acs.chemrev.6c00202

Read Online

ACCESS | Metrics & More | Article Recommendations

ABSTRACT: Nanocrystalline metal halide perovskites are promising light emitters for light-emitting diodes (PeLEDs) because they suppress the intrinsic problem of exciton dissociation through charge confinement within nanocrystalline domains. Although these nanostructures have enabled high-emission efficiencies, such confinement strategies typically result in significantly reduced charge transport. This limitation is attributed to numerous grain boundaries, which induce severe charge carrier scattering and trapping, alongside insulating organic ligands typically introduced for defect passivation and size reduction. Poor charge transport increases the required operating voltage and accelerates device degradation pathways under an electrical bias, leading to limited operational lifetimes. This Review examines material design strategies intended to mitigate the competition between charge confinement and transport across various nanocrystalline perovskites. Specifically, we investigate fundamental crystal nucleation and growth mechanisms and evaluate methods to optimize grain size, aiming to minimize the grain boundary to increase charge transport while maintaining charge confinement. Passivation strategies for defect states are also evaluated, emphasizing the engineering of organic ligands to enhance their electrical conductivity while maximizing the passivation efficacy. In addition, the integration of core/shell architectures is discussed as a promising strategy. By controlling the shell composition, these structures promote efficient charge transport while maintaining high radiative recombination rates. Together, these material design strategies aim to overcome the confinement and transport trade-offs in PeLEDs.



CONTENTS

1. Introduction B
2. Theoretical Background C
2.1. Charge Confinement C
2.2. Trade-Off between Charge Confinement and Charge Transport D
2.2.1. Grain Boundary Scattering D
2.2.2. Trap-Limited Charge Transport E
3. Practical Material Design for PeLEDs F
3.1. Crystal Size for Optimal Charge Confinement F
3.2. Ligand-Mediated Confinement and Transport F
3.3. Impact of Transport Limitations on Device Architecture G
4. Nanoscale-Polycrystalline Perovskites H
4.1. Solvent Engineering I
4.2. Additive Engineering J
4.3. Nanocrystal Pinning K
4.4. Post-treatment M
5. Quasi-2D Perovskites N
5.1. Carrier Transport in Quasi-2D MQW Films N
5.2. Suppressing Precursor Aggregation and Speciation Heterogeneity R
5.3. Crystallization Control S
5.3.1. Coordination/Inhibitor-Mediated Nucleation Delay S
5.3.2. Solvent-Removal and Solvation Engineering to Moderate Supersaturation S
5.3.3. Antisolvent-Triggered Forced Supersaturation for Synchronized Nucleation T
5.3.4. Substrate-Guided Nucleation and Phase Distribution Control T
5.4. Postprocessing to Refine *n*-Phases and Prevent 3D-Like Phase Growth U
6. Colloidal Perovskite Nanocrystals V
6.1. Nucleation and Growth Control in Colloidal PNCs W
6.1.1. Hot-Injection Synthesis W
6.1.2. Room-Temperature Synthesis X

Received: February 28, 2026
Revised: June 19, 2026
Accepted: June 24, 2026

ACS Publications

© XXXX The Authors. Published by American Chemical Society

Downloaded from pubs.acs.org/chreay/article-pdf/doi/10.1021/acs.chemrev.6c00202/6880579/acs.chemrev.6c00202.pdf by guest on 10 October 2026

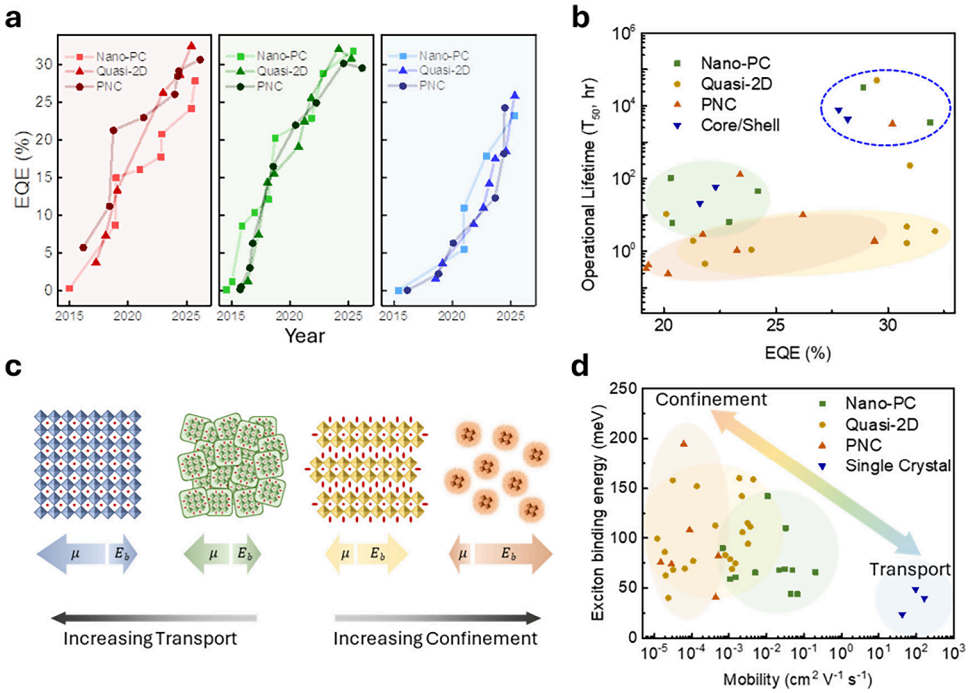


Figure 1. Overview of the charge confinement-transport trade-off in perovskite light-emitting diodes (PeLEDs). (a) Progress in reported external quantum efficiency (EQE) for nanoscale-polycrystalline perovskite (Nano-PC), quasi-2D perovskite, and perovskite nanocrystal (PNC) PeLEDs over the years. Data points are color-coded by emission wavelength, with red (620−700 nm), green (510−545 nm), and blue (below 485 nm) emitters denoted accordingly. EQE values calculated under Lambertian assumptions or enhanced by outcoupling structures are excluded. (b) Distribution of reported operational lifetime (T_{50} at initial brightness of 100 nit) versus EQE, categorized by perovskite structure. (c) Schematic comparison of representative nanocrystalline perovskite across the confinement-transport, illustrating the general trend from high mobility/low exciton binding energy to stronger confinement/higher exciton binding energy. (d) Correlation map of exciton binding energy and carrier mobility for nanocrystalline perovskites, visualizing the inverse tendency between confinement and transport.

6.1.3. Antisolvent Precipitation and Emulsion Synthesis X
6.1.4. Cold-Injection and Pseudo-emulsion Synthesis X
6.1.5. Purification Y
6.2. Surface Engineering Z
6.2.1. Acidic Counterpart Ligand Engineering Z
6.2.2. Multifunctional Additives Z
6.3. Ordered Assemblies in Perovskite Nanocrystals AB
6.3.1. Nanocube Superlattices AB
6.3.2. Anisotropic Nanoplatelet Superlattices AC
6.3.3. Rhombic Dodecahedral (RD) Superlattices AC
6.4. Challenges toward Superlattice PeLEDs AC
6.4.1. Confined Assembly of Long-Range Ordered Superlattice Thin Films AD
6.4.2. Interparticle Coupling Engineering via Ligand Chemistry AD
7. Core/Shell Perovskites for Balancing Charge Confinement and Transport AE
7.1. *In Situ* Core/Shell Perovskite AE
7.2. 3D/2D Perovskite Heterostructure AE
7.3. Core/Shell Perovskite with Cs_4PbBr_6 Phase AF
8. Thermally Evaporated Perovskites for LEDs AF
8.1. Crystallization-Mediated Exciton Confinement and Internal Charge Transport AG
8.2. Device Architecture for Efficient Charge Transport and Stable PeLEDs AH
9. Conclusion and Outlook AJ
Author Information AK
Corresponding Author AK
Authors AK
Author Contributions AK
Notes AK
Biographies AK
Acknowledgments AK
References AL

1. INTRODUCTION

Metal halide perovskites feature an ABX_3 crystal structure, where A is a monovalent cation, B is a divalent metal cation, and X is a halide anion. These materials are extensively investigated as light emitters for light-emitting diodes (LEDs) because of their tunable emission across the visible spectrum and narrow emission line widths that yield high color purity.[1,2] These materials are compatible with solution-based processing,[3−5] roll-to-roll manufacturing,[6,7] and thermal evaporation,[8−10] which provides flexibility in device fabrication and a potential pathway to scalable, cost-effective production advantages.[11] Following early observations of perovskite electroluminescence at temperatures below 200 K in the 1990s,[12−16] the first bright room-temperature perovskite LEDs (PeLEDs) were reported in 2014.[17,18] However, the initial device efficiency remained low with an external quantum efficiency (EQE) of ∼0.1%.[17,18] This low efficiency is attributed to the intrinsic properties of bulk three-dimensional (3D) perovskites, which exhibit low exciton binding energies (E_b).[19] Consequently, electron−hole pairs

Downloaded from pubs.acs.org/chreav/article-pdf/doi/10.1021/acs.chemrev.6c00202/6880579/acs.chemrev.6c00202.pdf by guest on 10 October 2026

https://doi.org/10.1021/acs.chemrev.6c00202
Chem. Rev. XXXX, XXX, XXX−XXX

thermally dissociate into free-carriers and undergo nonradiative recombination.

To address these fundamental material limitations, the use of nanocrystalline perovskites was proposed to improve luminescence efficiency, as documented in early patents filed in November 2014.[20,21] Building upon these structural concepts, the first efficient PeLEDs exhibiting an EQE of 8.53% were achieved through precise stoichiometric control and additive-based nanocrystal pinning.[3] These synthetic strategies yield nanoscale polycrystalline perovskites (nano-PCs). The confined nanoscale grains directly suppress the thermal ionization of excitons and reduce the subsequent exciton quenching.[3]

Consequently, material designs incorporating nanocrystalline perovskites have been widely adopted in PeLEDs.[22−24] Subsequent research has focused on combining charge confinement with defect passivation across three representative nanocrystalline perovskites, including nano-PCs, quasi-2D perovskites, and colloidal perovskite nanocrystals (PNCs), ultimately achieving EQEs approaching the theoretical limit.[25] Performance improved rapidly, and EQEs approaching 30% have been reported,[22,26−33] indicating that perovskites can function as efficient emitters (Figure 1a). Perovskite emitters are therefore often compared with organic light emitters and inorganic quantum dots, which serve as practical benchmarks for display performance targets.[25]

However, achieving a high EQE does not guarantee a long operational lifetime for the PeLEDs. The majority of reported high-EQE devices exhibit operational lifetimes below 100 h (Figure 1b), indicating that radiative recombination efficiency alone does not determine device lifetime.[25,34] Multiple factors collectively contribute to PeLED degradation during operation, including ion migration, redox reactions, and the deterioration of charge transport layers and electrodes. In terms of material design for mitigating these degradation pathways, one contributing factor is charge transport in the emissive layer (EML), which deteriorates as charge confinement increases because of additional barriers such as grain boundaries, organic spacers, or insulating ligands. Poor charge transport can accelerate the above degradation pathways by raising the operating voltage, intensifying the local electric field, and increasing Joule heating. Therefore, perovskite material design must address a fundamental trade-off between charge confinement and charge transport to achieve a high EQE and long operational lifetime.

Comparison of exciton binding energies and carrier mobilities across different perovskite structures illustrates this trade-off (Figure 1c, d). Single crystal perovskites typically exhibit relatively low exciton binding energies of ∼40 meV, alongside high charge-carrier mobilities exceeding ∼100 $cm^2\ V^{-1}\ s^{-1}$.[35] However, introducing structural confinement increases exciton binding energy while decreasing mobility. Nano-PCs exhibit a moderate level of confinement, resulting in an exciton binding energy of 40 to 70 meV and mobilities ranging from 10^{-3} to 10^{-1} $cm^2\ V^{-1}\ s^{-1}$. In contrast, quasi-2D perovskites and PNCs show much higher exciton binding energies, ranging from 70 to 150 meV. However, their mobility is significantly limited, with quasi-2D perovskites exhibiting mobilities between 10^{-5} and 10^{-2} $cm^2\ V^{-1}\ s^{-1}$, and PNCs ranging from 10^{-5} to 10^{-3} $cm^2\ V^{-1}\ s^{-1}$. These trends indicate that nano-PCs require enhanced charge confinement to boost exciton binding energy while preserving their charge transport ability, whereas quasi-2D perovskites and PNCs must overcome transport limitations inherent to their strongly confined structures.

This trade-off relationship can be directly observed in device performance trends. Strongly confined quasi-2D perovskite and PNC PeLEDs easily achieve EQEs exceeding 20%[22,26−31] and occasionally approach ∼30%.[36] Yet, these highly confined devices typically operate at elevated driving voltages and exhibit pronounced efficiency roll-off, consistent with severe charge transport limitations.[37−39] Short operational lifetimes are also commonly reported reflecting bias-induced degradation,[37,40−42] although the underlying degradation mechanisms involve additional factors beyond transport itself. In contrast, nano-PC PeLEDs show moderate EQEs typically below 25%, but exhibit lower operating voltages and reduced roll-off, consistent with their higher charge transport ability, and tend to show comparatively longer operational lifetimes extending over tens of hours (Figure 1b).

To meet the commercial requirements for PeLEDs, achieving both high EQE and long operational lifetime is a primary requirement, and one of the key material design challenges in achieving this is overcoming the trade-off between charge confinement and charge transport. Recent studies have demonstrated both high EQE and extended operational stability, indicating that precise material design can address the fundamental trade-off between charge confinement and transport. While operational stability is influenced by a broader set of degradation mechanisms, mitigating the confinement/transport trade-off addresses the electrically driven contributions to these pathways and, therefore, constitutes one necessary component of stable operation. The following sections explore the physical principles governing charge transport within the emissive layer and review material design strategies aimed at overcoming the confinement-transport trade-off.

2. THEORETICAL BACKGROUND

This section summarizes the principal mechanisms of charge confinement and transport in perovskite emitters and then outlines how the grain size and defect density govern these processes.

2.1. Charge Confinement

Grain size is a primary parameter that controls exciton formation and recombination. In unconfined bulk perovskite crystals, charge carriers are thermally ionized into free carriers, resulting in dominant bimolecular recombination. In confined structures, electron−hole pairs remain bound as excitons. This spatial confinement enables monomolecular excitonic recombination. Bimolecular recombination is relatively slow, leaving carriers with longer lifetimes and a higher susceptibility to trapping at defect sites. In contrast, excitonic recombination is faster and increases the probability of the radiative recombination. Consequently, reducing the crystal size is structurally beneficial to light emission.[25,43]

Under a charge confinement regime, the exciton binding energy can be defined using the Brus-type effective-mass model (particle-in-a-sphere).[44−46] In this model, the exciton binding energy is mainly determined by the Coulombic interaction between the electron and hole. Since these charge carriers are confined to a small spatial region, their opposite charges give rise to Coulombic attraction, which becomes stronger as the grain size decreases. This electrostatic force dominates the exciton binding energy, resulting in a strong dependence on the grain size:[44−46]

Downloaded from pubs.acs.org/chreav/article-pdf/doi/10.1021/acs.chemrev.6c00202/68805793/acs.chemrev.6c00202.pdf by guest on 10 October 2026

https://doi.org/10.1021/acs.chemrev.6c00202
Chem. Rev. XXXX, XXX, XXX−XXX

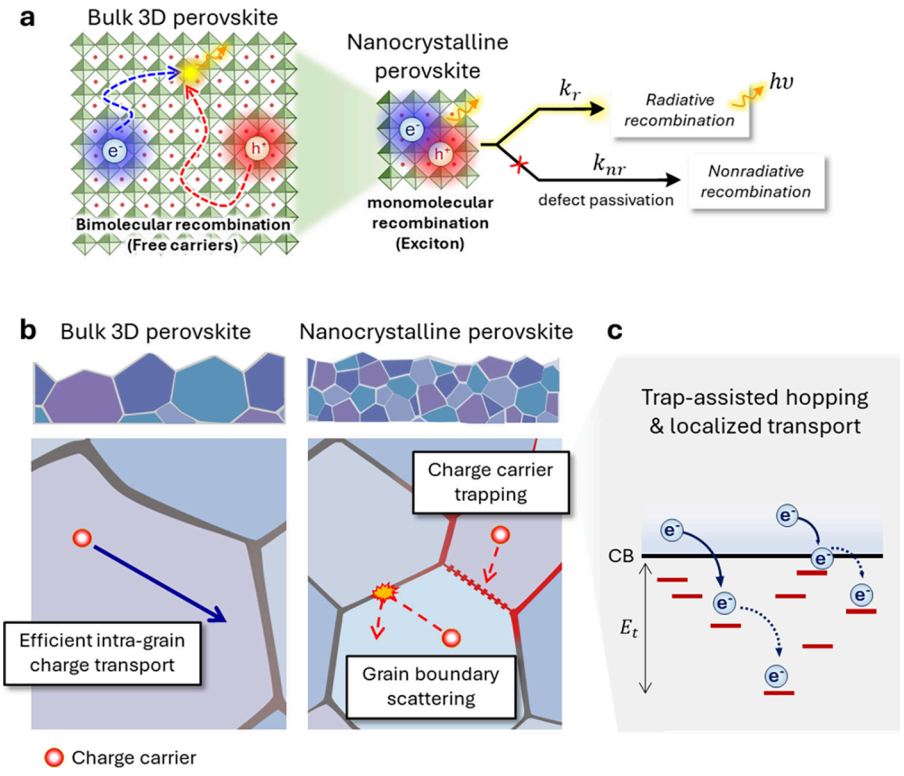


Figure 2. Grain-size-dependent trade-off between charge confinement and charge-carrier transport. (a) Schematic comparison of electron−hole recombination mechanisms in bulk 3D and nanocrystalline perovskites. In bulk 3D perovskites, electron−hole pairs thermally dissociate into free-carriers and subsequently undergo slow bimolecular recombination. In nanocrystalline perovskites, spatial confinement binds electron−hole pairs into excitons, which enables fast monomolecular recombination. Effective defect passivation is required to suppress the nonradiative recombination rate (k_{nr}) so that the accelerated excitonic radiative recombination rate (k_r) dominates the emission process for nanocrystalline perovskites. (b) Schematic illustration of charge-carrier transport limitations induced by grain size reduction. Bulk 3D perovskites support efficient internal charge transport. Conversely, nanocrystalline perovskites exhibit prominent grain boundary scattering, charge-carrier trapping at defect sites, and (c) trap-assisted localized hopping transport.

$$E_b(R) \approx \frac{\alpha e^2}{4\pi\varepsilon_0\varepsilon_r R}$$

where R is the effective domain radius, e is the elementary charge, ε_0 is the vacuum permittivity, ε_r is the effective relative dielectric constant experienced by the electron−hole pair. Furthermore, α is a dimensionless prefactor, which is typically assigned a value of 1.786 for ground-state $1S_e-1S_h$ exciton envelopes within the standard Brus approximation. Because the Coulomb interaction scales as $1/R$, decreasing R strengthens electron−hole attraction and increases E_b, which favors excitonic radiative recombination.[47,48]

Besides, practical radiative recombination can be described by the photoluminescence quantum yield (PLQY), which is determined by the competition between radiative and nonradiative recombination under optical excitation:

$$\mathrm{PLQY} = \frac{k_r}{k_r + k_{nr}}$$

where k_r and k_{nr} are the radiative and nonradiative recombination rates, respectively. An increase in E_b can promote bound electron−hole recombination and increase k_r.[47,48] High PLQY also requires suppression of k_{nr}, which is strongly affected by defect density. Grain size reduction increases the surface-to-volume ratio and can raise the density of surface-related defects.[49,50] These defects can accelerate trap-assisted Shockley−Read−Hall (SRH) recombination, increasing k_{nr} and quenching emission. Therefore, defect passivation is required to reduce nonradiative losses while retaining confinement-enhanced excitonic recombination (Figure 2a).[25]

2.2. Trade-Off between Charge Confinement and Charge Transport

Although smaller grains strengthen charge confinement, perovskite films typically exhibit reduced charge-carrier mobility as the grain size decreases. This reduction arises mainly from the increased density of grain boundaries and surfaces, which introduces additional (i) momentum randomizing scattering and (ii) trap-mediated carrier immobilization.[51,52] Both effects become more pronounced as the domain size decreases and the surface-to-volume ratio increases (Figure 2b).[53]

2.2.1. Grain Boundary Scattering. The Drude transport model is typically employed to describe the decrease in charge-carrier mobility associated with reduced grain sizes. This model treats charge carriers as quasi-free particles whose momentum is randomized by scattering events.[50,54,55] Accordingly, the mobility is expressed as

$$\mu = \frac{e\tau}{m^*}$$

where e is the elementary charge, m^* is the effective mass of the carrier, and τ is the momentum relaxation time, defined as the average interval between momentum-randomizing scattering events.[56] Within the interior of a perovskite grain, charge carriers transport efficiently through delocalized band-edge states, which

Downloaded from pubs.acs.org/chreav/article-pdf/doi/10.1021/acs.chemrev.6c00202/68805793/acs.chemrev.6c00202.pdf by guest on 10 October 2026

https://doi.org/10.1021/acs.chemrev.6c00202
Chem. Rev. XXXX, XXX, XXX−XXX

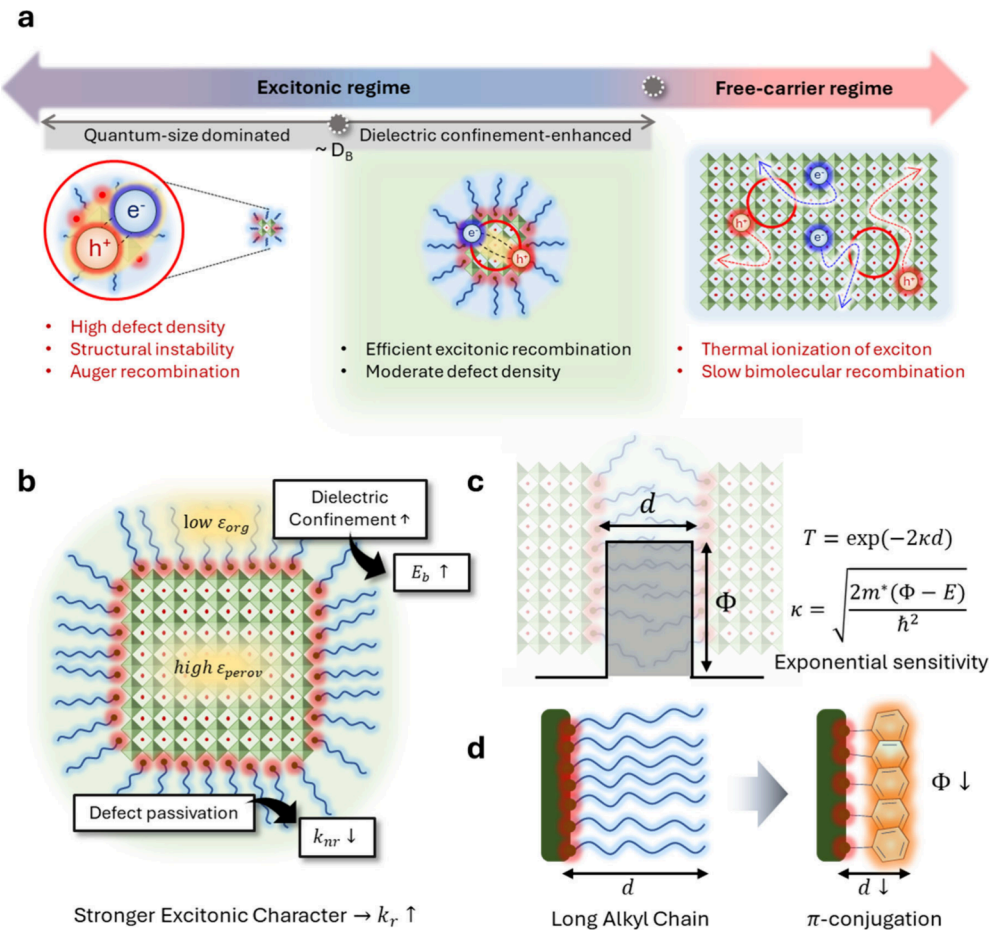


Figure 3. Practical material design principles for perovskite light-emitting diodes. (a) Transition of charge-carrier confinement regimes according to perovskite crystal size. The dielectric confinement-enhanced regime is identified as optimal for balancing radiative efficiency and structural integrity of the perovskite lattice. (b) Synergetic effects of dielectric confinement and surface defect passivation mediated by organic ligands. The dielectric mismatch between the organic ligand (ε_{org}) layer and the perovskite lattice (ε_{perov}) enhances the exciton binding energy (E_b). Simultaneously, ligands passivate surface defects, reducing the nonradiative recombination rate (k_{nr}) to maintain high luminescence efficiency. (c and d) Interfacial charge transport barriers and structural optimization strategies of ligands. (c) The ligand layer acts as a rectangular potential barrier with width d and height Φ. The carrier tunneling probability (T) is exponentially dependent on these barrier parameters. (d) Replacing long insulating alkyl chains with π-conjugated structures enhances electronic coupling and orbital overlap, effectively reducing the barrier height Φ and facilitating efficient interdomain charge transport.

is consistent with the intrinsically rapid charge transport of the bulk perovskite lattice.[57] However, structural imperfections, interfacial disorder, and chemical inhomogeneity near grain boundaries introduce additional scattering channels.[58]

Consequently, grain boundaries act as discrete scattering centers that increase the overall scattering rate. This increased scattering decreases τ and correspondingly reduces the charge-carrier mobility μ. As the average grain size decreases, carriers encounter these boundaries more frequently over a specific transport distance. Thus, boundary-induced scattering increasingly dominates and limits long-range charge transport. As a result, perovskite films with smaller grains and higher grain boundary densities typically exhibit lower effective mobilities because boundary scattering significantly shortens τ. This physical mechanism can suggest one reason for substantially lower charge-carrier mobilities in nanocrystalline perovskite films compared to the intrinsic mobility of perovskite single crystals.[59,60]

2.2.2. Trap-Limited Charge Transport. In addition to momentum scattering, reduced grain size decreases charge carrier transport by increasing carrier trapping at surface and grain-boundary defect states. As the surface-to-volume ratio increases, undercoordinated sites and defect-rich regions become more prevalent. These structural imperfections introduce electronic states within the bandgap that act as carrier traps.[51,52] Such traps slow the overall charge transport relative to the intrinsic band mobility of delocalized carriers.

This behavior is typically described by the 'multiple trapping and release (MTR)' model. In this model, carriers drift through delocalized transport states but are intermittently captured by localized traps with an activation depth E_t (Figure 2c).[61] While trapped, carriers are immobilized and do not contribute to long-range drift. They eventually return to delocalized states through thermally activated detrapping. Deeper traps with larger E_t increase the residence time in trapped states. This extended residence time increases the average transit time and reduces the effective mobility. The trapping-induced mobility reduction can be expressed as

$$\mu_{eff} = \mu_0 \frac{n_{free}}{n_{free} + n_{trap}}$$

https://doi.org/10.1021/acs.chemrev.6c00202
Chem. Rev. XXXX, XXX, XXX−XXX

Downloaded from pubs.acs.org/chreay/article-pdf/doi/10.1021/acs.chemrev.6c00202/68805793/acs.chemrev.6c00202.pdf by guest on 10 October 2026

where μ_0 is the intrinsic mobility of delocalized transport states, n_{free} is the density of carriers in delocalized states, and n_{trap} is the density of trapped carriers.[61,62] As the overall trap density increases, n_{trap} increases relative to n_{free}, and effective mobility μ_{eff} decreases even if intrinsic mobility μ_0 remains unchanged. Trap-limited transport therefore reduces mobility primarily by increasing the fraction of time carriers spend immobilized in localized states.

In perovskite thin films, traps are typically concentrated at grain boundaries and interfaces, where energetic disorder is higher.[63] These regions can promote short-range hopping through localized states and further suppress long-range transport, particularly when trap densities are sufficient to disrupt bandlike conduction.[61,62] Under electrical bias, trap-rich boundary regions can also promote carrier accumulation and injection imbalance by localizing injected carriers, which are relevant to electrically driven devices.[64]

In nanograined perovskite emitter films, both scattering and trapping mechanisms operate simultaneously. Grain boundaries shorten the momentum relaxation time τ through enhanced scattering, which is characteristic of Drude-type behavior. Concurrently, microstructural defects increase the trapped carrier density n_{trap} in accordance with the MTR model. Together, these processes produce a substantial decrease in the effective mobility across the emissive layer. Thus, although grain size reduction enhances charge confinement, it introduces microstructural features that restrict charge transport. This relationship reinforces the fundamental confinement-transport trade-off in perovskite light-emitting diodes.

3. PRACTICAL MATERIAL DESIGN FOR PELEDS

Charge-carrier scattering and trapping at grain boundaries, along with the insulating organic ligands and additives employed to increase charge confinement and passivate defects, inherently impede charge transport in nanocrystalline perovskites. These limitations promote local carrier accumulation and injection imbalance, which subsequently activates nonradiative recombination pathways. Therefore, the PeLED design must concurrently address radiative recombination and charge transport within the EML. Accordingly, this chapter identifies the optimal design principles for nanocrystalline perovskite emitters and their coordinating organic ligands.

3.1. Crystal Size for Optimal Charge Confinement

Reducing the perovskite crystal size induces charge confinement, but an optimal size range must be identified. Excessive size reduction increases the surface-to-volume ratio, which raises the defect density and decreases the structural stability.[49,50] Surface defects can be partially compensated by increasing the concentration of surface ligands or additives, but high ligand coverage and numerous grain boundaries can hinder charge transport. In addition, strong confinement and excessively high exciton binding energy can promote Auger recombination at high carrier densities.[43,65] Therefore, the optimal crystal size is expected to lie in an intermediate range corresponding to a weakly confined regime, which can balance the charge confinement and charge transport.

On the basis of the assumption of a large dielectric mismatch between the perovskite crystal and the surrounding medium, lower and upper bounds of the optimal crystal size are proposed for the dielectric confinement-enhanced regime. For the lower-size bound, the crystal dimension is referenced to the exciton Bohr diameter, D_B. For typical halide perovskites, this diameter is generally known to be approximately 10 to 12 nm, although it varies depending on the composition.[66−69] Crystals with dimensions below D_B correspond to the quantum-size-dominated regime. This regime exhibits excessively high quantum and dielectric confinements alongside structural instability, making these crystals highly susceptible to the previously described limitations. Consequently, the lower-size criterion should exceed D_B. For the upper-size bound, the boundary is defined near the transition from free-carrier-dominated bimolecular recombination to exciton-dominated monomolecular recombination (Figure 3a).[48] Although the exact transition from bimolecular to excitonic recombination is not sharply defined, grains measuring several tens of nanometers can still function as efficient light emitters because excitonic and bimolecular recombination pathways partially coexist within this intermediate size range.[32,70] Therefore, further investigation and discussion are required to precisely define the structural and photophysical boundaries associated with this upper size range (Figure 3a).

3.2. Ligand-Mediated Confinement and Transport

Organic ligands directly influence two coupled physical factors that govern the PeLED performance. First, ligands passivate undercoordinated surface sites, suppress trap-assisted nonradiative recombination, and improve overall radiative efficiency. Furthermore, ligands define the local dielectric environment. The dielectric mismatch between the inorganic perovskite lattice and the surrounding organic layer induces a strong dielectric confinement. This confinement increases the electron−hole interaction and the corresponding exciton binding energy.[71,72] In nanocrystalline perovskites, the combined effects of dielectric confinement and surface defect passivation allow for maintaining high radiative efficiencies despite their large surface-to-volume ratio (Figure 3b).

Conversely, the ligand layer introduces an interfacial barrier that impedes carrier transfer between neighboring perovskite domains and hinders charge transport. If the ligand layer is approximated as a rectangular potential barrier with a width d and height Φ, the carrier tunneling probability T can be estimated using a WKB (Wentzel−Kramers−Brillouin) expression,[73−75]

$$T = \exp(-2\kappa d),\ \kappa = \sqrt{\frac{2m^*(\Phi - E)}{\hbar^2}}$$

where m^* is the carrier effective mass, E is the carrier energy, d is the ligand-defined interdomain separation, and Φ is the barrier height. The exponential dependence indicates that modest increases in ligand length (increasing d) or barrier height (increasing Φ) strongly suppress interdomain coupling and reduce charge transport (Figure 3c). Consequently, the backbone length and the terminal-group structure are essential design parameters for electrical operation. Longer alkyl chains typically increase d and strengthen the insulating character of the barrier. In contrast, electronically coupled structural motifs such as π-conjugated groups increase electronic coupling across the ligand layer. These conjugated groups enhance orbital overlap and effectively reduce the barrier height Φ (Figure 3d). Therefore, practical ligand design must rigorously balance surface passivation and dielectric confinement against resistive transport losses.

Downloaded from pubs.acs.org/chreav/article-pdf/doi/10.1021/acs.chemrev.6c00202/68805793/acs.chemrev.6c00202.pdf by guest on 10 October 2026

https://doi.org/10.1021/acs.chemrev.6c00202
Chem. Rev. XXXX, XXX, XXX−XXX

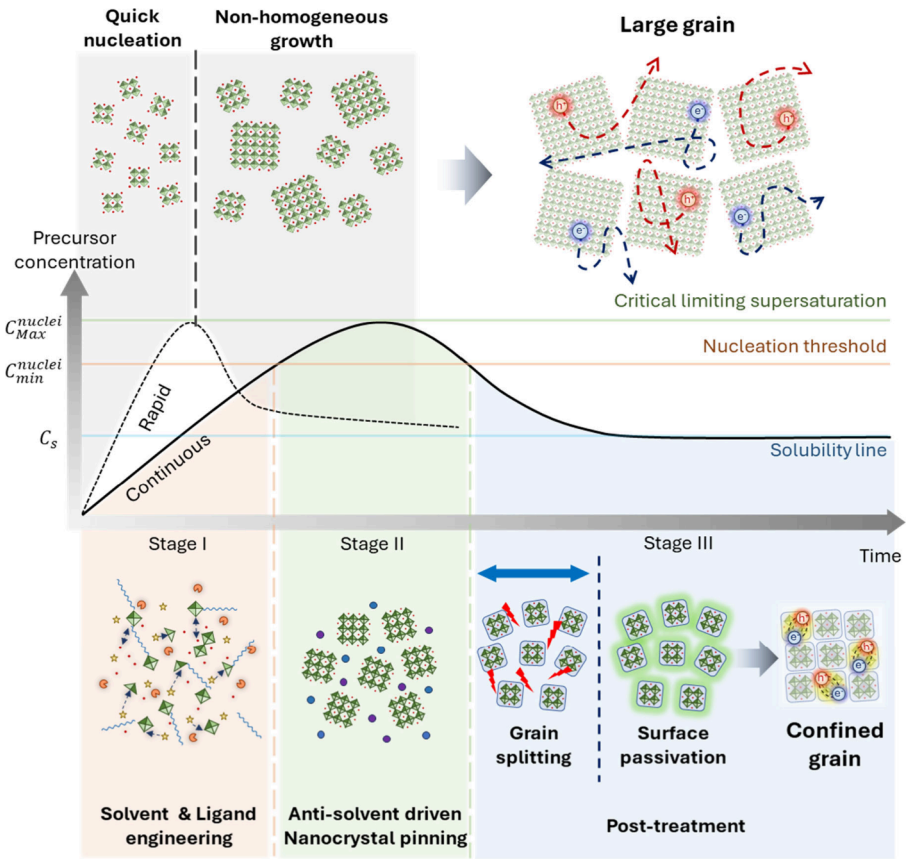


Figure 4. Modulation of crystallization dynamics based on LaMer's theory for spatial confinement of excitons.

3.3. Impact of Transport Limitations on Device Architecture

The limited charge transport ability of perovskite accelerates operational degradation in PeLEDs. Charge transport in the EML is characterized by the carrier mobility (μ), which under an applied electric field E sets the drift velocity $v = \mu E$ and the electronic conductivity $\sigma_{el} = Nq\mu$ for a carrier density N. More generally, when both electrons and holes contribute to charge transport, the electronic conductivity can be written as $\sigma_{el} = q(n\mu_e + p\mu_h)$, where n and p are the electron and hole densities. The current density J required for a target luminance is therefore expressed as

$$J = Nqv = Nq\mu E = \sigma_{el}E$$

so that perovskites with lower mobility operate at a higher electric field, and correspondingly a higher operating voltage, across the EML. Joule heating, whose power density scales as

$$p = J^2/\sigma_{el}$$

therefore intensifies as the electronic conductivity of the EML decreases at a given current density.[38,39] Ion migration in the EML is described by the ion drift velocity, and the ion mobility follows the thermally activated Arrhenius law

$$v_{ion} = \mu_{ion}E,$$

$$\mu_{ion} = \mu_0 \exp(-E_a/k_BT),$$

which together show that ion migration is accelerated both directly by the elevated electric field and indirectly by the temperature rise from Joule heating, with the latter exponentially enhancing μ_{ion}.[76] Furthermore, transport limitations within the EML can lead to local carrier accumulation under bias, which increases the probability of Auger recombination, electrochemical redox reactions, and thermal hot-spotting.[37,77]

To mitigate the issues arising from limited charge transport, ultrathin or vertically monograin emissive layers are typically employed. This architecture minimizes the necessary charge-transport distance across the perovskite film and effectively bypasses bulk transport limitations. However, this approach positions the recombination zone closer to the charge transport layers (CTLs), which could be vulnerable to energetic disorder, chemical interactions, and interfacial traps.[78] In addition, achieving a specific target luminance in thin perovskite layers can require a higher charge carrier density and a stronger electric field compared with thicker EML structures. These operating conditions increase the susceptibility of the device to non-radiative losses and electrically driven degradation.[77]

When interdomain charge transport improves, the injected carriers redistribute uniformly throughout the perovskite film. This spatial redistribution decreases the local charge carrier density and reduces the effective electric field applied across the perovskite layer, which subsequently suppresses the electrically driven degradation. Additionally, improved transport allows for the use of thicker emissive layers. These thicker layers support high-brightness operation[22,79] and enhance photon recycling to improve the overall light extraction efficiency.[80] Consequently, securing efficient charge transport in the perovskite EML is essential for sustaining high radiative efficiency under operational bias and additionally helps to mitigate electrically driven degradation pathways.

To satisfy these requirements, distinct material design strategies are necessary for different nanocrystalline perovskites, including nano-PC perovskites, quasi-2D perovskites, and

Downloaded from pubs.acs.org/chreav/article-pdf/doi/10.1021/acs.chemrev.6c00202/68805793/acs.chemrev.6c00202.pdf by guest on 10 October 2026

https://doi.org/10.1021/acs.chemrev.6c00202
Chem. Rev. XXXX, XXX, XXX−XXX

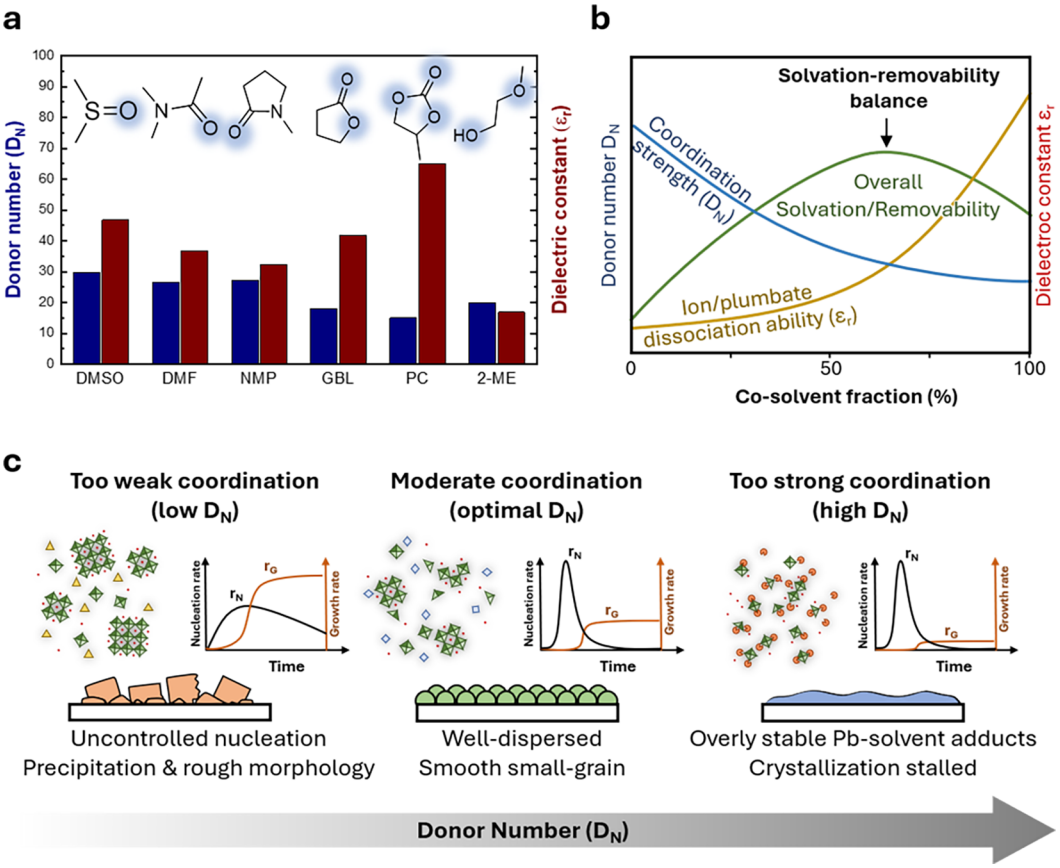


Figure 5. Solvent chemistry of perovskite crystallization. (a) Donor number (D_N) and dielectric constant (ε_r) of representative solvents used for perovskite film fabrication. (b) Schematic plot showing donor number, dielectric constant, and an overall solvation/removability balance as a function of cosolvent fraction. (c) Role of solvent-precursor coordination kinetics in determining morphology during crystallization.

PNCs. These material systems possess fundamental differences in the lattice dimensionality, intrinsic charge confinement, and charge transport. The subsequent sections detail how structural dimensionality, chemical composition, and organic surface chemistry are employed within each specific system to control the nanostructure, minimize the defect density, regulate interdomain coupling, and optimize charge transport.

4. NANOSCALE-POLYCRYSTALLINE PEROVSKITES

Among nanocrystalline perovskites, nano-PC systems exhibit relatively favorable charge transport but weak confinement. The central material design objective is therefore to strengthen charge confinement through grain size reduction without sacrificing the inherently favorable charge transport. Crystallization control strategies discussed in this section are described in relation to this requirement.

The crystallization of nano-PC perovskites is often discussed within LaMer's model, where the formation of a solid phase proceeds through a nucleation stage followed by crystal growth (Figure 4).[81−85] In the absence of deliberate kinetic control, rapid supersaturation of perovskite precursors can generate nuclei with a broad size distribution.[85] Although nucleation can generate a large population of small nuclei, only those that exceed a critical size persist as stable crystallites, and the remaining nuclei are dissolved or incorporated into larger domains.[85−87] Once nuclei form, subsequent growth, coalescence, and competitive grain enlargement broaden the grain size distribution and generate defective boundaries with under-coordinated metal sites, which promote nonradiative recombination.[88,89]

To mitigate these limitations, chemically guided crystallization-control strategies have been developed to increase spatial confinement in nanoscale polycrystalline perovskites by reducing the grain size and weakening interdomain coupling.[85,90] A widely adopted approach is to tune the strength of precursor-solvent coordination, which alters the stability of precursor complexes, thereby slowing the nucleation and growth kinetics and suppressing excessive grain growth.[91−93] In parallel, ligands and crystallization modulators can stabilize intermediate phases and introduce steric barriers between domains,[94,95] therefore reducing interdomain connectivity and suppressing grain growth.[96,97] Combined with solvent/ligand precursor engineering, which generates a high density of small nuclei by maximizing supersaturation in the initial nucleation regime (stage I), nanocrystal pinning (NCP) is beneficial for the formation of small grain size with narrow distribution (stage II).[3,85,98] In the NCP process, an antisolvent is introduced to abruptly reduce the solubility of the precursor, facilitating rapid nucleation while simultaneously limiting further grain growth by continued supply and redistribution of dissolved species.[99−101] As a result, coarsening pathways such as ripening and grain merging are strongly suppressed, and the microstructure is locked into a small-grain regime with a narrow size distribution.[3]

However, reducing the perovskite grain size inevitably increases the surface-to-volume ratio, leading to increased surface and grain boundary defects.[102−104] These defects introduce trap states that localize carriers and activate

https://doi.org/10.1021/acs.chemrev.6c00202
Chem. Rev. XXXX, XXX, XXX−XXX

Downloaded from pubs.acs.org/chreay/article-pdf/doi/10.1021/acs.chemrev.6c00202/68805793/acs.chemrev.6c00202.pdf by guest on 10 October 2026

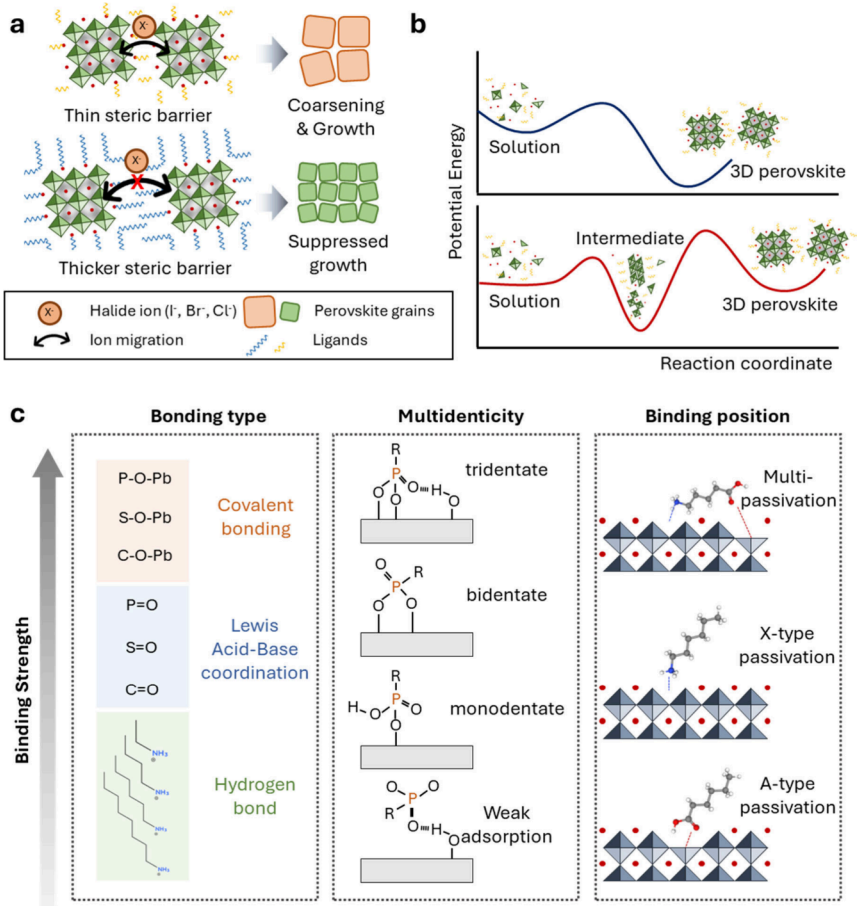


Figure 6. Effect of additive engineering. (a) Crystal growth suppression of nanoscale-polycrystalline perovskites induced by steric hindrance. (b) Schematic potential energy along the reaction coordinates for a direct pathway from solution to nanoscale-polycrystalline perovskite involving an intermediate state. (c) Summary of ligand interactions categorized by bonding type, multidenticity, and binding position, with an indicative binding-strength scale and representative passivation modes.

nonradiative pathways.[105−107] To address this issue, a variety of post-treatment processes have been developed, including surface passivation, ionic compensation, and interfacial reconstruction (stage III).[108−112] When combined with kinetic control over nucleation and growth, these approaches enable nanocrystalline perovskite thin films that retain strong confinement while suppressing trap-assisted nonradiative recombination.[113−115]

4.1. Solvent Engineering

Controlling the crystallization pathway of precursor solutions requires a detailed understanding of precursor-solvent coordination chemistry. The solvents for precursor solution act as Lewis bases that coordinate to Pb^{2+} cations, stabilizing the precursor not as fully dissociated ions but as a dynamic equilibrium of lead-halide coordination complexes and colloidal clusters.[91,116−120] Solvent-coordinated haloplumbate complexes in precursor solutions can vary in size depending on solvent coordinating strength, which can, in turn, alter the coordination structure of PbX_2 and modulate its aggregation behavior.[91,121−123]

The strength of solvent coordination to Pb^{2+} can be discussed using the Gutmann donor number (DN), which reflects Lewis basicity (Figure 5a,b).[91,124] In low-DN solvents, the solvent weakly coordinates to Pb^{2+}, leaving a larger fraction of coordination sites available for halide complexation.[118] As a result, halide-rich Pb-X complexes form readily, which typically accelerates nucleation and crystallization.[91,118,125] In contrast, high-DN solvents form stronger coordination complexes with Pb^{2+}, competitively suppressing halide coordination and thereby retarding crystallization.[91,118,126] Stronger coordination also improves the dispersion of precursor species and suppresses aggregation, resulting in smaller and more uniform complex populations in solution.[91,117] Beyond DN, the solvent dielectric constant (ε) controls ionic dissociation and electrostatic screening in the precursor,[119,120] shifting the equilibrium between ion-paired adducts, haloplumbate complexes, and colloidal clusters and thereby altering nucleation kinetics (Figure 5a,b).[119,125,126] Because the size and distribution of these precursor-solvent complexes strongly influence the nucleation density and subsequent growth kinetics, solvent coordination strength affects both precursor stability and the resulting film morphology (Figure 5c).[91,118,120]

However, excessively strong coordination with higher donor numbers can overstabilize the solvated complexes and raise the energy barrier for solvent removal during the crystallization process.[118] In that regime, supersaturation is reached more slowly, and nucleation is suppressed, which can lead to incomplete crystallization.[91,118,127] Trapped residual solvent and remaining coordination-stabilized intermediate phases reduce crystallinity.[128,129] To overcome this trade-off, cosolvent strategies are introduced.[130,131] Strongly coordinating solvents such as dimethyl sulfoxide (DMSO), *N*-methyl-2-pyrrolidone

Downloaded from pubs.acs.org/chreav/article-pdf/doi/10.1021/acs.chemrev.6c00202/6880579/acs.chemrev.6c00202.pdf by guest on 10 October 2026

https://doi.org/10.1021/acs.chemrev.6c00202
Chem. Rev. XXXX, XXX, XXX−XXX

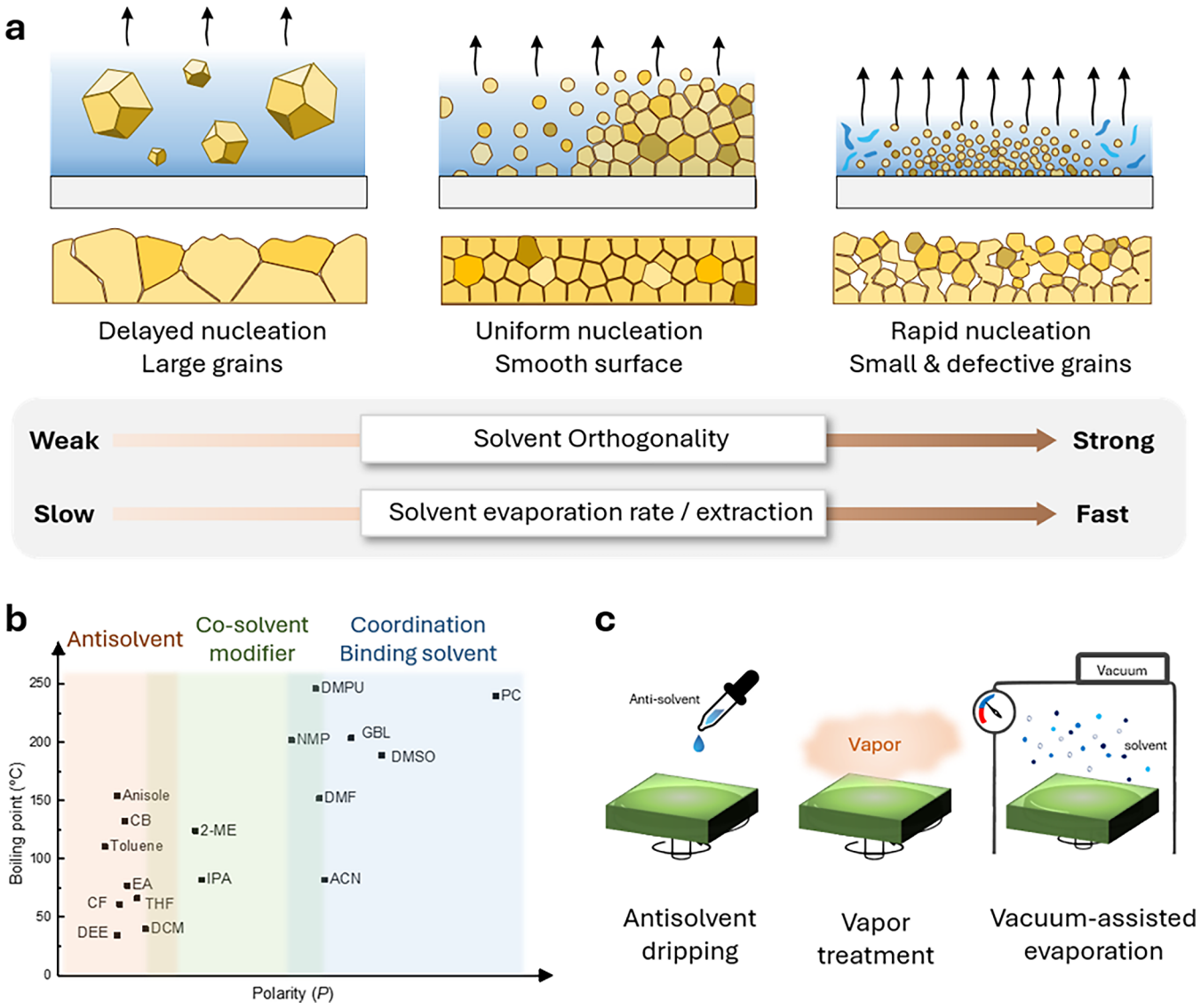


Figure 7. Antisolvent-assisted nanocrystal pinning (NCP) for nucleation of perovskites. (a) Schematic comparison of nucleation and resulting grain morphology as a function of solvent orthogonality and solvent evaporation/extraction rate. (b) Polarity-boiling-point solvent map grouped by antisolvent, cosolvent modifiers, and coordinating solvents. (c) Schematic overview of antisolvent treatment modes in solution processing, including antisolvent dripping, vapor treatment, and vacuum-assisted evaporation.

(NMP), or dimethylformamide (DMF) are combined with weaker-coordinating (or more readily removed) cosolvents such as 2-methoxyethanol (2-ME) or propylene carbonate (PC).[118,132] The mixed-solvent system stabilizes coordination-bound precursor complexes while reducing competition for Pb^{2+} coordination and enabling more facile solvent removal while still maintaining sufficient solvation of ionic species.[117,118,133] This combination facilitates solvent exchange and detachment from Pb^{2+} at the desired stage, enabling more controlled supersaturation, and nucleation.[91,118,120] This approach preserves precursor stability while improving kinetic control over nucleation and growth, providing a versatile method for tuning the crystallization dynamics in PeLED-relevant perovskite films.[120,133,134]

4.2. Additive Engineering

Introducing additives into the precursor enables chemical interactions with perovskite species that stabilize ligand-precursor complex-induced intermediate phases, thereby modulating the nucleation window and slowing subsequent growth kinetics.[135,136] Furthermore, additives provide steric hindrance at domain interfaces and grain surfaces, increasing the effective separation between neighboring perovskite domains and limiting coalescence-driven enlargement during the growth stage (Figure 6a).[137,138] Accordingly, ligand incorporation is correlated with a longer-lived intermediate state and introduces a physical barrier to subsequent growth, which favors the formation of smaller perovskite crystals that exhibit enhanced spatial confinement (Figure 6b).[138,139]

The effective binding strength of organic ligands in halide perovskite systems is governed by molecular architecture and binding functional groups, backbone chain length,[105,140] concentration and surface coverage, and the number of anchoring sites per molecule (Figure 6c).[141]

For ligand functional group chemistry, in commonly used phenylethylammonium bromide (PEABr), ammonium ($-NH^{3+}$) groups are commonly used as hydrogen-bond donors[142] that interact with halide species and intermediate

https://doi.org/10.1021/acs.chemrev.6c00202
Chem. Rev. XXXX, XXX, XXX−XXX

Downloaded from pubs.acs.org/chreav/article-pdf/doi/10.1021/acs.chemrev.6c00202/68805793/acs.chemrev.6c00202.pdf by guest on 10 October 2026

complexes, providing a relatively weak interaction that can broaden the nucleation window.[143,144] By contrast, oxygen-containing Lewis base functional groups such as carbonyl (C=O), sulfoxide (S=O), and phosphoryl (P=O)[83,145] can coordinate to Pb-containing species, typically yielding stronger ligand-bound intermediates.[136,146] Functional groups capable of even stronger anchoring, including acidic or protic groups such as carboxylic acids (−COOH), phosphonic acids (−PO-$(OH)_2$), and sulfonic acids (−SO_2(OH)), can further increase the effective binding strength through stronger interactions.[22,147−150]

Backbone chain length can modulate crystallization primarily by changing the dynamics of precursor complexation, including ligand exchange rates, aggregation behavior, and the formation of kinetically persistent intermediate species that mediate the liquid-to-solid transition.[131,151] As the backbone length between a headgroup and a tail increases, the precursor-ligand complex becomes more stable and persists longer because reduced conformational mobility and stronger intermolecular packing favor sustained contact and cooperative stabilization in the precursor environment, which in turn delays nucleation and growth.[131,151] Shorter chain ligands, by contrast, tend to exchange and reorient more rapidly, which can promote faster precursor conversion and less pronounced growth retardation.[151,152] Accordingly, these longer-lived precursor-bound states can increase nucleation density and suppress coarsening, enabling smaller grains and more uniform microstructures that are often desirable for emissive perovskite films.[139,153]

Multidentate ligands provide multiple simultaneous binding interactions, making them harder to displace from precursor or surface sites; this stabilizes ligand-bound intermediates and more effectively retards crystallization.[154,155] For example, in bidentate hexane-1,6-diyl-bis(oxy-4-triphenylphosphine-oxide) (2-TPPO) or tetradentate pentaerythrityl-tetrakis(oxy-4-triphenylphosphine oxide) (4-TPPO), multiple P=O donors can exhibit stronger effective coordination to Pb halide precursor species than a TPPO with a single P=O group molecule.[83,156] By further stabilizing precursor-ligand intermediates through multiple coordination sites, multidentate TPPO increases the relative intensity of the absorption peak assigned to $PbBr_x^-$ observed in UV−vis spectra, indicative of bromoplumbate complexes before full crystallization.[83,131] Besides, when multidentate groups coexist in a single ligand,[70,149,155,157,158] the binding mode can change qualitatively, and the net interaction energy can differ substantially depending on whether binding occurs through one group or through cooperative multipoint attachment.[157,159] For ligands including both ammonium and carboxyl groups, precursor-ligand intermediates can adopt multiple coordination modes.[157] The ammonium group mainly contributes hydrogen bonding, the carboxyl group provides the coordination interaction, or both groups act together through multipoint attachment.[157,160,161] In a previously reported density functional theory (DFT) analysis, the interaction energies were on the order of 0.25 eV for an ammonium-mediated binding and about 0.44 eV for a carboxyl-mediated binding, increasing to close to 0.86 eV when both groups engaged simultaneously, indicating a substantially stronger net stabilization under multipoint attachment.[157] Accordingly, zwitterionic or multifunctional ligands allow the binding mode and interaction strength to be tuned through the binding of multifunctional groups, enabling stronger intermediate stabilization and more effective growth suppression and thereby promoting smaller, more uniform domain sizes under controlled ligand coverage and coordination conditions.[149,157,159,162]

4.3. Nanocrystal Pinning

NCP can be rationalized within LaMer's model as a postnucleation kinetic freezing.[3,163] The process works near the end of Stage II (burst nucleation) and the onset of Stage III,[84,164] effectively pinning the microstructure in a nanocrystalline regime and limiting grain growth,[3] Ostwald ripening, and coalescence pathways that would otherwise dominate Stage III.[84,138,164,165] This kinetic pinning is commonly induced by introducing an orthogonal antisolvent during film formation.[166−169] The antisolvent is selected to be a poor solvent for the perovskite precursor species while remaining compatible with the polar solvent, such that solvent exchange rapidly increases supersaturation.[3,91,120,166,170] This abrupt change in solvent environment lowers the effective solubility and suppresses solute redistribution, driving dense nucleation while restricting the mass transport required for sustained growth.[85,120,135,166]

The effectiveness of NCP depends strongly on the rate of antisolvent-induced solvent exchange and polar solvent removal (Figure 7a).[81,87] Slow extraction keeps postnucleation reorganization and continued growth active, allowing ripening and coalescence to partially resume and shifting the morphology toward larger grains.[84,171,172] By contrast, excessively rapid extraction produces an abrupt and spatially uneven rise in supersaturation, which can trigger nonuniform nucleation and poor grain fusion.[84,85,96] Effective pinning, therefore, requires an extraction rate that is fast enough to generate dense nucleation but not so fast that nucleation becomes spatially heterogeneous.[84] Under this condition, solute redistribution is minimized, further grain enlargement is suppressed, and a more uniform nanocrystalline microstructure is obtained.[87,96,138,168] With this perspective, chlorobenzene and chloroform are often used to promote small grain sizes by accelerating solvent exchange and rapidly reducing precursor solubility (Figure 7b).[3,99,100,168] These antisolvents are generally weakly coordinating toward precursor complexes, while their volatility shortens the time window for solute redistribution, thereby suppressing subsequent growth and ripening.[100,101,173]

Beyond conventional NCP, which relies primarily on antisolvent orthogonality to reduce precursor solubility and induce kinetic pinning, an extended approach often referred to as additive-assisted nanocrystal pinning (A-NCP) has been developed (Figure 7c).[3,81,99,138,167,169] In this strategy, functional additives are incorporated into the antisolvent to further regulate crystallization.[135,169] Bulky additives can impose additional steric hindrance at nascent grain surfaces and interfaces, suppressing postnucleation grain growth beyond that achievable by antisolvent pinning alone.[3,99] In addition, these additives can preferentially reside at grain boundaries, where they passivate defect-rich regions and reduce nonradiative recombination by forming core/shell mimicked nanograins.[3,99]

As an alternative approach, a supersaturated solution with a small amount of perovskite precursor species, such as CsBr, can be used to further reduce grain size.[174,175] When this supersaturated antisolvent contacts the wet perovskite films, the local solubility decreases abruptly, promoting faster precipitation and a higher nucleation density. This rapid kinetic pinning further limits mass transport and favors smaller nanocrystals, often below 40 nm.[139,176]

Downloaded from pubs.acs.org/chreav/article-pdf/doi/10.1021/acs.chemrev.6c00202/68805793/acs.chemrev.6c00202.pdf by guest on 10 October 2026

https://doi.org/10.1021/acs.chemrev.6c00202
Chem. Rev. XXXX, XXX, XXX−XXX

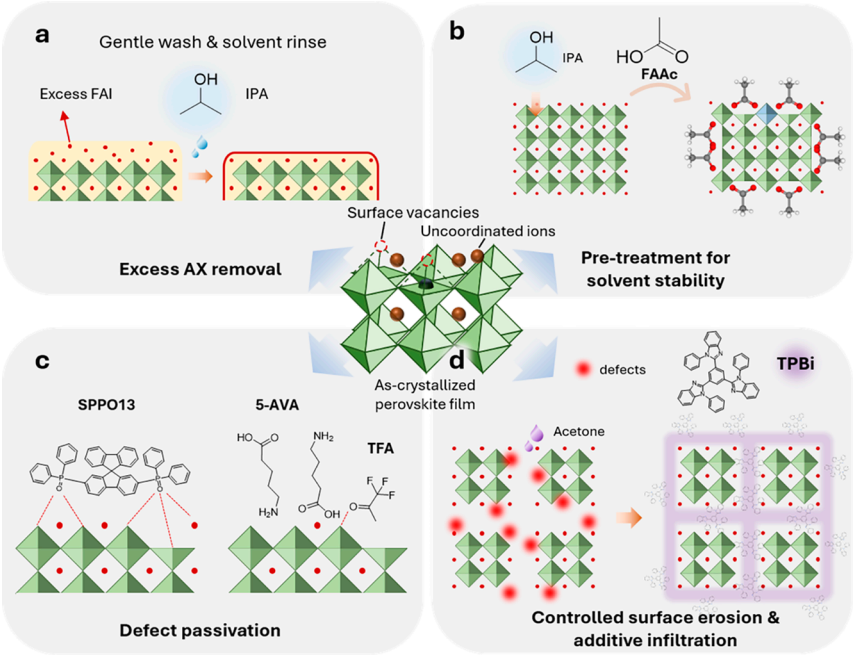


Figure 8. Schematic illustrations of post-treatment strategies for as-crystallized nanoscale-polycrystalline perovskite films. (a) Removal of excess AX species on the surface. (b) Surface pretreatment to improve solvent resistance. (c) Defect passivation using passivating molecular additives. (d) Surface resurfacing via controlled surface erosion, followed by additive infiltration.

In the A-NCP process, the antisolvent flow rate becomes especially important because it governs the penetration depth of the additive-containing solution into the precursor layer.[99,177] Limited penetration at low flow rates concentrates the additive near the surface, confining kinetic pinning and defect passivation largely to the surface region.[81,99,167,178] Greater penetration at higher flow rates distributes the additive throughout the film thickness and enables passivation at grain surfaces and grain boundaries across the layer.[81,99] This leads to a more uniform vertical grain size profile and a more homogeneous distribution of passivating species, forming core/shell-mimicked nanograins.[81,178]

Temperature offers an additional way to tune solvent removal by adjusting extraction and evaporation rates.[139] At lower temperatures, reduced evaporation and slower solvent–antisolvent interdiffusion make precipitation less abrupt, allowing nuclei and grains to rearrange and pack more uniformly, thereby reducing void formation and improving film continuity.[139,179−181] Thus, an orthogonal antisolvent can still produce a rapid rise in supersaturation and a nucleation burst, while the lower temperature helps yield a denser, more continuous film.[139]

However, when the antisolvent is dripped onto a wet film, the initial droplet contact and the subsequent lateral spreading can create position-dependent gradients in local solvent concentration and composition.[182−184] These gradients lead to spatial variations in the onset of supersaturation and nucleation density across the coated area.[182] At the droplet center, not fully crystallized perovskite film first encounters the antisolvent, driving rapid solvent exchange and earlier supersaturation.[182] This promotes fast, dense nucleation and earlier kinetic freezing for the developing nanostructure.[182] In contrast, away from the center, the antisolvent arrives later and in a more diluted form because it is delivered mainly through spreading and diffusion. As a result, supersaturation is reached more gradually, allowing more time for solute redistribution, crystal growth, and local structural reorganization before the film is fully crystallized. These spatial differences can produce distinct microstructures within the films.[182] Edge regions are therefore more likely to show increased roughness, phase heterogeneity including the formation of lower-dimensional components, and higher defect densities.[182,185,186] Microdroplet-based antisolvent deposition is a promising strategy to address spatial nonuniformity. Delivering antisolvent as microdroplets generated by a pressure-driven atomizer can minimize radial gradients during the supersaturation stage and promote the onset of nucleation at comparable times across the substrate area, thereby improving lateral homogeneity.[182,184,187]

To achieve more spatially uniform control over perovskite crystallization, crystallization kinetics can be regulated using vapor-phase treatments rather than liquid antisolvent dripping (Figure 7c). Vapor-phase nanocrystal pinning avoids localized liquid contact and instead enables gradual infiltration and diffusion of vapor molecules into the wet film.[168,188] This procedure allows for more balanced nucleation and growth, resulting in suppression of localized nanocrystal agglomeration and excessive surface roughening, thereby facilitating the formation of high-coverage films with densely connected crystalline domains.[168,188,189]

Vacuum-assisted solvent removal can further accelerate residual solvent extraction and shorten the time available for sustained growth and postnucleation coarsening (Figure 7c).[190,191] In the approach demonstrated for *in situ* formation of a Type I band-aligned nanocrystalline perovskite film, a nonstoichiometric, adduct-mediated precursor environment inhibits excessive crystal growth, while subsequent solvent-vacuum drying completes the solid-state transformation while preserving this nanocrystalline regime, yielding a dense and laterally uniform film microstructure.[190]

Downloaded from pubs.acs.org/chreav/article-pdf/doi/10.1021/acs.chemrev.6c00202/68805793/acs.chemrev.6c00202.pdf by guest on 10 October 2026

https://doi.org/10.1021/acs.chemrev.6c00202
Chem. Rev. XXXX, XXX, XXX−XXX

Table 1. Perovskite Solvent Characteristics

Solvent	Dielectric constant (ε)	Boiling point (°C)	Vapor pressure @ 25 °C (mmHg)	Donor Number	Hansen parameter (δD/δP/δH)	Role
Propylene carbonate (PC)	64.9	242	0.045	15.1	20/18/4.1	Medium coordination
Dimethyl sulfoxide (DMSO)	46.7	189	0.60	29.8	19.0/16.6./7.4	Coordination solvent (strong)
γ-Butyrolactone (GBL)	41.8	204	0.45	18.0	18/7.4/9	Medium coordination
Acetonitrile (ACN)	37.5	82	90	14.1	15.3/18.0/6.1	Cosolvent
Dimethylformamide (DMF)	36.7	153	3.87	26.6	17.4/13.7/11.3	Coordination solvent (strong)
N,*N*′-Dimethylpropyleneurea (DMPU)	36.1	246	1.5	33.0	18/14/7	Coordination solvent (strong)
N-Methyl-2-pyrrolidone (NMP)	32.2	202	0.345	27.3	18.0/12.3/7.2	Coordination solvent (strong)
Isopropyl alcohol (IPA)	17.9	82	45	21.1	15.8/6.1/16.4	Antisolvent
2-Methoxyethanol (2-ME)	16.9	125	9.5	-	16.2/9.2/16.4	Cosolvent
Dichloromethane (DCM)	8.93	40	430	1.0	18.2/6.3/6.1	Very volatile
Tetrahydrofuran (THF)	7.6	66	170	20	16.8/5.7/8.0	Dispersion solvent
Ethyl acetate	6.02	77	93	17.1	15.8/5.3/7.2	Antisolvent
Chlorobenzene (CB)	5.62	132	12	3.3	19.0/4.3/2.0	Antisolvent
Chloroform (CF)	4.81	61	200	-	17.8/3.1/5.7	Antisolvent
Diethyl ether	4.33	35	440	19.2	14.5/2.9/4.6	Strong antisolvent
Anisole	4.33	154	3	9	17.8/4.1/6.7	Antisolvent
Toluene	2.38	111	28	-	18.0/1.4/2.0	Antisolvent

4.4. Post-treatment

Post-treatment steps provide additional routes to improve charge injection and transport and, in some cases, to impose further structural confinement (Figure 8). In nanoscale polycrystalline perovskite films, reduced grain size can increase spatial confinement, but it can also increase the density of surface-related trap states.[81,186,192] In addition, excess AX species on the surface, which are electronically insulating and do not participate in perovskite lattice formation, can reduce effective electronic coupling and interfacial contact between the perovskite and the adjacent transport layer.[192−194] Post-treatments can therefore be used to passivate surface defects,[140,195−197] compensate ionic imbalance,[140,196,197] and induce surface reconstruction,[195,198,199] leading to improved electrical and optical characteristics.[178,192,200]

Residual organic salts and surface-coordination defects are representative targets of such post-treatments. For example, residual excess formamidinium iodide (FAI) can be removed by rinsing with isopropanol (IPA), which selectively dissolves unreacted organic salts without compromising the perovskite film (Figure 8a).[193,201] In addition, post-treatment with a coordinating ligand such as 2,7-bis(diphenylphosphoryl)-9,9′-spirobifluorene (SPPO13), which binds to undercoordinated metal centers to passivate surface defects, can also improve the electron-transport interface and provide additional benefits (Figure 8b).[202,203] These ligands can bind strongly to center metal of perovskites, improving chemical stability while also facilitating electron injection and improving charge balance.[108,204,205] Together, these effects can improve carrier transport, reduce nonradiative losses, and enhance operational stability.[109,206]

However, solution-based post-treatment steps can chemically perturb the metastable perovskite film, and solvent exposure can introduce additional degradation pathways.[199,207] Solvents that strongly solvate the perovskite lattice can damage the film, generate a high density of surface vacancies, and induce lattice distortion, thereby increasing nonradiative recombination.[109,184,208] For this reason, relatively nondestructive solvents with lower polarity and boiling points, such as chloroform, ethyl acetate, and 1,2-dichloroethane, are often chosen to modify the surface while preserving the perovskite crystal structure.[168,209]

In some cases, an additional pretreatment step is introduced to mitigate solvent-induced damage during post-treatment (Figure 8c).[204,210−212] For example, when additives such as 4-fluorophenethylammonium bromide (4-F-PEABr) are deposited from solution onto blue nanoscale-polycrystalline perovskite films before thermal annealing, the processing solvent can partially etch the surface and generate additional halide vacancies, which can introduce new loss pathways.[204,212] To reduce such damage, vapor-phase pretreatments have been employed before the solution post-treatment.[168,213] In a representative approach, a vapor-assisted crystallization (VAC) process is used to deliver additives such as formamidinium acetate (FAAc), to the perovskite surface, via exposure to an additive-containing solvent vapor (e.g., DMF).[197,214] This pretreatment can promote strong coordination between the additive and Pb^{2+} sites before the subsequent post-treatment step, thereby reducing solvent-induced film damage while preserving the benefits of post-treatment.[199,215]

In contrast, strongly polar and highly volatile solvents (e.g., acetone) are sometimes used intentionally to induce controlled surface erosion.[199,201,216] In this case, the objective is not limited to superficial defect passivation but rather to enable additive infiltration and in-depth modification of the perovskite film. The solvent promotes surface reconstruction and can open grain boundary diffusion pathways that facilitate the penetration of an additive such as 2,2′,2″-(1,3,5-benzinetriyl)-tris(1-phenyl-1-H-benzimidazole) (TPBi) into the film (Figure 8d).[199,201,217] TPBi preferentially accumulates along grain boundaries, where its aromatic, phenyl-rich framework can form a relatively hydrophobic barrier that suppresses moisture and oxygen ingress, thereby improving film stability, while also binding to the perovskite surface, suppressing dynamic lattice vibrations, and strengthening the perovskite lattice.[81,199,218] In addition, interfacial TPBi can reduce the electron-injection barrier at the transport-layer/perovskite contact, which can increase the

Downloaded from pubs.acs.org/chreav/article-pdf/doi/10.1021/acs.chemrev.6c00202/68805793/acs.chemrev.6c00202.pdf by guest on 10 October 2026

https://doi.org/10.1021/acs.chemrev.6c00202
Chem. Rev. XXXX, XXX, XXX−XXX

electron-injection efficiency and improve charge balance.[199,219,220] The characteristics of solvents for nano-PC perovskite engineering and the performance of nano-PC PeLEDs are summarized in Tables 1 and 2, respectively.

5. QUASI-2D PEROVSKITES

Quasi-2D perovskites provide strong charge confinement through their inherent multiple quantum well architecture,[221] but the same structural features that enable confinement also hinder charge transport. The central material design objective for this system is therefore to preserve confinement while restoring transport. In quasi-2D perovskites, both confinement and transport are governed by the distribution of *n*-phases, where low-*n* phases provide strong confinement but contain a high fraction of insulating organic spacers and often possess deep traps that obstruct transport and high-*n* or 3D-like phases enable better transport but weaken confinement. Phase-distribution engineering is therefore discussed in this section as the practical means of balancing these requirements.

Structurally, quasi-2D perovskites are commonly described by the formula $A'_2A_{n-1}B_nX_{3n+1}$ and consist of corner-sharing $[BX_6]^{4-}$ octahedral slabs separated by bulky organic spacer cations (A′). This natural quantum confinement, combined with the dielectric mismatch between the inorganic slab and the organic spacer, raises the exciton binding energy from ∼50 meV to over 300 meV relative to bulk 3D perovskites.[25] However, the confinement structure arising from this self-assembly also underlies a major drawback: phase distribution across multiple *n*-values. Formation energy differences between adjacent *n*-phases are often too small to thermodynamically select a single targeted *n*-phase, and spin-coating introduces spatially and temporally nonuniform solvent evaporation, intermediate complexation, and precursor redistribution.[222] As a result, even with stoichiometries designed for a target *n*-phase, films frequently solidify into polydisperse quantum-well ensembles containing multiple *n*-phases (Figure 9a). When the slab thickness approaches or falls below the exciton Bohr radius, a single-layer change in *n* can substantially shift the bandgap,[222,223] so that a broad *n*-phase distribution can lead to spectral broadening, reduced color purity, and nonradiative losses. During quasi-2D perovskite crystallization, thermodynamically stable 2D monolayer ($n = 1$) phases form first by preferentially incorporating A′ cations, rendering the residual solution A′-deficient (i.e., a composition shifted from the initial stoichiometry) and thereby promoting subsequent formation of 3D-like ($n = \infty$) phases.[25,224]

For PeLED applications, both excessive low-*n* formation ($n = 1-3$) and 3D-like ($n = \infty$) formation are detrimental: low-*n* phases suffer trap-assisted and Auger losses and low conductivity,[225,226] whereas 3D-like phases act as red-shifted funneling sinks.[4,227] Quasi-2D PeLED strategies therefore target medium-*n* ($n = 4-5$) or high-*n* ($n \geq 6$) as the dominant emissive species, while minimizing parasitic low-*n* and 3D-like phases, thereby yielding a phase-narrowed ensemble.[25,227,228] In the following, we first analyze the transport mechanism that motivates this design objective, and the subsequent sections analyze quasi-2D phase formation step by step to highlight the mechanisms that enable n-distribution narrowing and stabilization of the desired emissive phase.

5.1. Carrier Transport in Quasi-2D MQW Films

Unlike three-dimensionally connected ABX_3 perovskite, in which carriers move through a continuous corner-sharing octahedral network, the MQW architecture of quasi-2D perovskites divides the inorganic framework into $[BX_6]^{4-}$ slabs only a few octahedra thick, separated by insulating organic spacer layers. This slab and spacer architecture gives rise to three transport characteristics intrinsic to the MQW geometry: strong anisotropy between in-plane and out-of-plane carrier motion,[229] a tunneling-limited interdomain pathway across the organic spacer,[230] and an ultrafast funneling cascade that redistributes excitons and carriers across coexisting *n*-phases along the *n*-graded energy landscape.[5,231]

Transport within a quasi-2D domain is intrinsically anisotropic, reflecting the structural and electronic difference between the slab and the spacer. Carrier motion is more favorable parallel to the metal-halide slabs, where the corner-sharing $[BX_6]^{4-}$ network remains continuous. Experimentally, photoconductivity analysis of highly oriented PEA_2PbI_4 films yields long-range sum mobilities of ∼8 $cm^2\ V^{-1}\ s^{-1}$, indicating appreciable in-plane charge transport along well-aligned inorganic sheets.[232] Transport along the stacking direction is structurally hindered, as carriers must tunnel across the organic spacer that separates adjacent inorganic slabs. This spacer functions as an interlayer tunneling barrier, with its thickness controlling the barrier width and the energetic mismatch between the metal-halide band-edge states and the electronic states of the organic spacer determining the effective barrier height. In a simple WKB approximation, the tunneling probability scales as $T = \exp(-2\kappa d)$, where d represents the effective tunneling distance across the spacer. Thus, interlayer electronic coupling decreases steeply as the spacer becomes thicker, consistent with anisotropic transport measurements on quasi-2D lead-halide single crystals showing substantially lower out-of-plane mobility than in-plane mobility.[229] In practical quasi-2D PeLED emitting layers, however, the extracted mobilities are much lower, typically ranging from 10^{-5} to 10^{-2} $cm^2\ V^{-1}\ s^{-1}$, and depend strongly on the measurement method, defect density, spacer content, *n*-phase distribution, and crystallographic orientation. Therefore, charge transport in quasi-2D perovskite is better understood in terms of the in-plane/out-of-plane anisotropy than by any single mobility value. This anisotropy also explains why quasi-2D PeLED performance is sensitive to crystal orientation: in substrate-parallel slabs, vertical current must pass through stacked organic spacers, limiting macroscopic mobility, whereas vertically oriented slabs provide more continuous metal-halide pathways along the device current direction.[230] Orientation and the spatial distribution of *n*-phases across the emitting layer therefore become key factors governing charge transport, with strategies that promote vertical slab alignment through buried-interface engineering discussed below.

The third and most distinctive transport characteristic appears in films with a distribution of *n*-values, which is typical for spin-coated quasi-2D emitting layers. Because the bandgap of a quasi-2D phase decreases monotonically with *n* from the strongly confined low-*n* limit toward the bulk value at high-*n*,[233] a mixed-*n* film acts as an energetic cascade, in which wide-bandgap low-*n* domains serve as donors and narrow-bandgap high-*n* domains as acceptors, driving excitations downhill toward the lowest-energy domains. This process, commonly called 'energy funneling', actually proceeds through two transfer channels differing in the species being transported.[231] In the first channel, a bound electron−hole pair in a low-*n* well transfers its excitation to a higher-*n* acceptor by Förster-type dipole−dipole coupling across the organic spacer, so only the excitation energy moves, not the

Downloaded from pubs.acs.org/chreav/article-pdf/doi/10.1021/acs.chemrev.6c00202/68805793/acs.chemrev.6c00202.pdf by guest on 10 October 2026

https://doi.org/10.1021/acs.chemrev.6c00202
Chem. Rev. XXXX, XXX, XXX−XXX

Table 2. Summary of Nanoscale-Polycrystalline Perovskite Light-Emitting Diodes[a]

Composition	EL peak (nm)	Luminance (cd m^{-2}) /radiance	EQE (%)	$V_{on}/V_{1,000\ nit}/V_{10,000\ nit}$	Operational lifetime (T_{50})	Strategy	Molecular additive	Ref.
$CsPb(Br/Cl)_3$	461	2,707	3.05	3.9/4.5/-	9 min @ 100 cd m^{-2}	Molecular additive	MS, PS	148
$CsPbCl_{1.5}Br_{1.5}$	464	2,180	9.8	3.2/4.5/-	27 min @ 100 cd m^{-2}	Molecular additive	Br-MBA^+	95
$CsPbBr_3$	480	2,910	17.9	3.0/4.5/5.5	126 min @ 100 cd m^{-2}	Molecular additive	TFPPO, MBA^+, Br-MBA^+, DMA^+, Br-DMA^+	94
$CsPb(Br_{0.84}Cl_{0.16})_3$	489	1,500	10.3	2.9/5.4/-	390 s @ 100 cd m^{-2}	Solvent engineering		82
$CsPbBr_3$	512	8,872	25.19	2.5/4.1/5.7	55 min @ 100 cd m^{-2}	Molecular additive *in situ* core/shell	2-TPPO 4-TPPO	83
$PEA_{0.2}(CsPbBr_3)$+LiBr	515	41,340	30.98	2.4/3.2/4.0	203 h @ 100 cd m^{-2}	Antisolvent engineering	-	182
$PEA_2Cs_{1.6}MA_{0.4}Pb_3Br_{10}$	517	52,000	25.6	2.7/3.0/3.5	115 min @ 7,200 cd m^{-2}	Molecular additive	TFPPO	145
$CsPbBr_3$	518	16,436	10.5	2.8/4.0/5.5	250 h @ 100 cd m^{-2}	Molecular additive	CsTFA	147
$(FPEA_2PbBr_4)_{0.02}(FA_{0.72}Cs_{0.1}GA_{0.18}PbBr_3)_{0.98}$	525	>150,000	23.3	3.0/3.7/-	T_{95} ~ 243 h @ 100 cd m^{-2}	Polymer/Molecular additive	PAA, Niacinamide	90
$CsPbBr_3$	525	60,237	22.93	2.6/3.1/4.0	15.6 h @ 1,000 cd m^{-2}	Antisolvent engineering	-	176
$CsPbBr_3$	525	51,890	4.76	2.7/3.8/5.0	80 h @ 1,000 cd m^{-2}	Vapor treatment	PEO, Chloroform	168
$MAPbBr_3$	530	1,000	8.53	3.5/5.5/7.5	-	Compositional engineering NCP treatment	-	3
$MAPbBr_3$	530	6,950	8.21	2.8/4.2/-	T_{20} ~ 150 s @ 100 cd m^{-2}	Compositional engineering Solvent engineering	-	190
$MAPbBr_3$	~530	55,440	12.1	2.8/5.0/-	135 min @ 5 mA cm^{-2}	Molecular additive	PMA	139
$MAPbBr_3$	~530	~100,000	11.7	2.8/3.8/5.0	251 min @ 100 cd m^{-2}	Antisolvent engineering Molecular additive	TPBi	81
$FAPbBr_3$	536	~11,000	5.53	2.5/3.4/-	>96 h @ 3 mA cm^{-2}	Interfacial engineering	LiF	188
$(FA_{0.7}MA_{0.1}GA_{0.2})_{0.87}Cs_{0.13}PbBr_3$	540	470,000	28.9	2.2/2.4/2.7	520 h @ 1,000 cd m^{-2}	Molecular additive *in situ* core/shell	BPA	22
$CsPbI_3$	~700	10,152	23.4	2.0/3.0/4.0	234 h @ 6.3 W sr^{-1} m^{-2}	Molecular additive	ACl_2	158
$FA_{0.83}Cs_{0.17}PbI_3$	789	1282.8 W sr^{-1} m^{-2}	17.5		130 h @ 100 mA cm^{-2}	Ligand engineering	PPAI	140
$FAPbI_3$	789	1,593 W sr^{-1} m^{-2}	23.2		227 h @ 100 mA cm^{-2}	Molecular additive	EDEADI	105
$FAPbI_3$	~800	558.46 W sr^{-1} m^{-2}	22.32		103.3 h @ 25 mA cm^{-2}	Molecular additive	5-AVATFA	157
$FAPbI_3$	~800	1103.31 W sr^{-1} m^{-2}	~20		84.8 h @ 100 mA cm^{-2}	Solvent engineering		109
$FAPbI_3$	~800	964 W sr^{-1} m^{-2}	23.6		106.1 h @ 100 mA cm^{-2}	Surface post-treatment Cross-linking	Chloroform, TMTA	206
$FAPbI_3$	800	497 W sr^{-1} m^{-2}	23.8		32 h @ 107 W sr^{-1} m^{-2}	Molecular additive	MSPE	70
$FAPbI_3$	~800	~300 W sr^{-1} m^{-2}	19.2		43 h @ 100 mA cm^{-2}	Molecular additive	APS	149
$FAPbI_3$	802	393 W sr^{-1} m^{-2}	20.2		-	Molecular additive	$NH_2-PEG_4-NH_2$	155
$CsSnI_3$	935 951	36 W sr^{-1} m^{-2}	6.6		17 h @ 20 mA cm^{-2}	Molecular additive	SPPO13	108

https://doi.org/10.1021/acs.chemrev.6c00202
Chem. Rev. XXXX, XXX, XXX−XXX

Downloaded from pubs.acs.org/chreay/article-pdf/doi/10.1021/acs.chemrev.6c00202/6880579 3/acs.chemrev.6c00202.pdf by guest on 10 October 2026

Table 2. continued

Composition	EL peak (nm)	Luminance (cd m^{-2}) /radiance	EQE (%)	$V_{on}/V_{1,000\ nit}/V_{10,000\ nit}$	Operational lifetime (T_{50})	Strategy	Molecular additive	Ref.
$CsSnI_3$	948	15 W sr^{-1} m^{-2}	4.72		11.6 h @ 20 mA cm^{-2}	Molecular additive	Hesperetin	[142]

[a]Turn-on voltage (V_{on}) and driving voltages at 1,000 and 10,000 cd m^{-2} ($V_{1,000\ nit}$ and $V_{10,000\ nit}$) were extracted by digitization from the *J*−*V*−*L* curves of the corresponding references. 5-AVATFA (5-ammonium valeric acid trifluoroacetate); PPAI (phenylpropylammonium iodide); 2-TPPO (hexane-1,6-diyl-bis(oxy-4-triphenylphosphine oxide)); 4-TPPO (pentaerythrityl-tetrakis(oxy-4-triphenylphosphine oxide)); PAA (poly(acrylic acid)); MBA^+ (α-methyl-benzyl-ammonium); Br-MBA^+ (Bromo-α-methyl-benzyl-ammonium); DMA^+ (α,α-dimethyl-benzyl-ammonium); Br-DMA^+ (bromo-α,α-dimethyl-benzyl-ammonium); BPA (benzylphosphonic acid); PMA (phenylmethylamine); MS (methanesulfonate); PS (propanesulfonate); TMTA (trimethylolpropane triacrylate); EDEADI (2,2′-(ethylenedioxy) diethylammonium diiodide); TFPPO (tris(4-fluorophenyl)phosphine oxide); SPPO13 (2,7-bis(diphenylphosphoryl)-9,9′-spirobifluorene); TPBi (2,2′,2″-(1,3,5-benzinetriyl)-tris(1-phenyl-1-H-benzimidazole)); MSPE (2-[4-(methylsulfonyl)phenyl] ethylamine); CsTFA (cesium trifluoroacetate); ACl_2 (diaza-18-crown-6 dihydriodide); APS (3-amino-propanesulfonic acid); PEO (poly(ethylene oxide)); NH_2−PEG_4-NH_2 (3,6,9,12-tetraoxatetradecane-1,14-diamine)

carriers themselves.[231,234] In the second channel, free electrons and holes either generated by exciton dissociation or injected directly under electrical bias migrate down the *n*-graded band offsets and accumulate in the narrow-bandgap domains before recombination.[5,231] These two channels, excitonic energy funneling and free-carrier funneling, are different in mechanism but are not separate phenomena. These two processes share the same *n*-graded landscape and channel excitation downhill toward emissive high-*n* domains, while operating on ultrafast picosecond to subpicosecond time scales in mixed-*n* quasi-2D films.[231,235] They are also difficult to disentangle from ground-state bleach (GSB) signal in transient absorption spectra, which reflects their combined population. This experimental overlap suggests that funneling in mixed-n quasi-2D films often reflects coupled excitonic energy transfer and interphase carrier transfer, rather than a single uniquely separable pathway. The relative contribution of these channels depends strongly on the local exciton binding energy. Low-*n* wells with binding energies of several hundred meV are predominantly excitonic and described by FRET,[223] whereas high-*n* or 3D-like domains have lower binding energies owing to stronger dielectric screening, which increases the free-carrier contribution at room temperature. As binding energy decreases gradually with *n*, the mechanism shifts along the cascade but leads to the same outcome, fast downhill redistribution of excitation toward emissive high-*n* domains.

This cascade is central to quasi-2D PeLED operation because it redistributes excitons and charge carriers before radiative recombination in the emissive high-*n* domains. Ultrafast transient-absorption (TA) and time-resolved photoluminescence (TrPL) measurements on mixed-*n* lead-bromide quasi-2D films have resolved excited-population transfer from low-*n* donors to high-*n* acceptors on subpicosecond to picosecond time scales,[231,233] and have further revealed carrier redistribution across quantum wells with different *n* values.[236] Because these transfer times are far shorter than the typical 1−10 ns radiative lifetime of the high-*n* acceptor, funneling can be largely completed before recombination in suitably controlled mixed-*n* films. These short transfer time scales arise from two structural features of the MQW stack. In the excitonic channel, the nanometer-scale separation between donor and acceptor domains enables efficient Förster-type transfer when spectral overlap and transition-dipole orientation are favorable.[234,235] In the free-carrier channel, composition-dependent conduction and valence band offsets between adjacent n-phases provide a thermodynamic driving force for downhill redistribution, although the actual rate also depends on interdomain contact, disorder, and trap-mediated processes.[231] Thus, the spacer-defined MQW structure simultaneously limits macroscopic out-of-plane transport and enables ultrafast local energy and carrier funneling across *n*-dependent quantum wells, creating an internal asymmetry between rapid interphase redistribution and spacer-limited long-range charge transport.

This cascade plays a dual role in device operation. One beneficial consequence is that this funneling acts as an internal spectral filtering mechanism for the polydisperse *n*-phase ensembles formed during quasi-2D crystallization. Even when several *n*-phases coexist, excitations are redistributed into a smaller subset of emissive high-*n* acceptors within picoseconds, so the underlying phase distribution is often only weakly reflected in the device spectrum rather than appearing as a set of fully resolved emission peaks.[231] The corresponding drawback is that the same efficient funneling that masks phase polydispersity can also amplify the impact of a poorly controlled phase

Downloaded from pubs.acs.org/chreav/article-pdf/doi/10.1021/acs.chemrev.6c00202/68805793/acs.chemrev.6c00202.pdf by guest on 10 October 2026

https://doi.org/10.1021/acs.chemrev.6c00202
Chem. Rev. XXXX, XXX, XXX−XXX

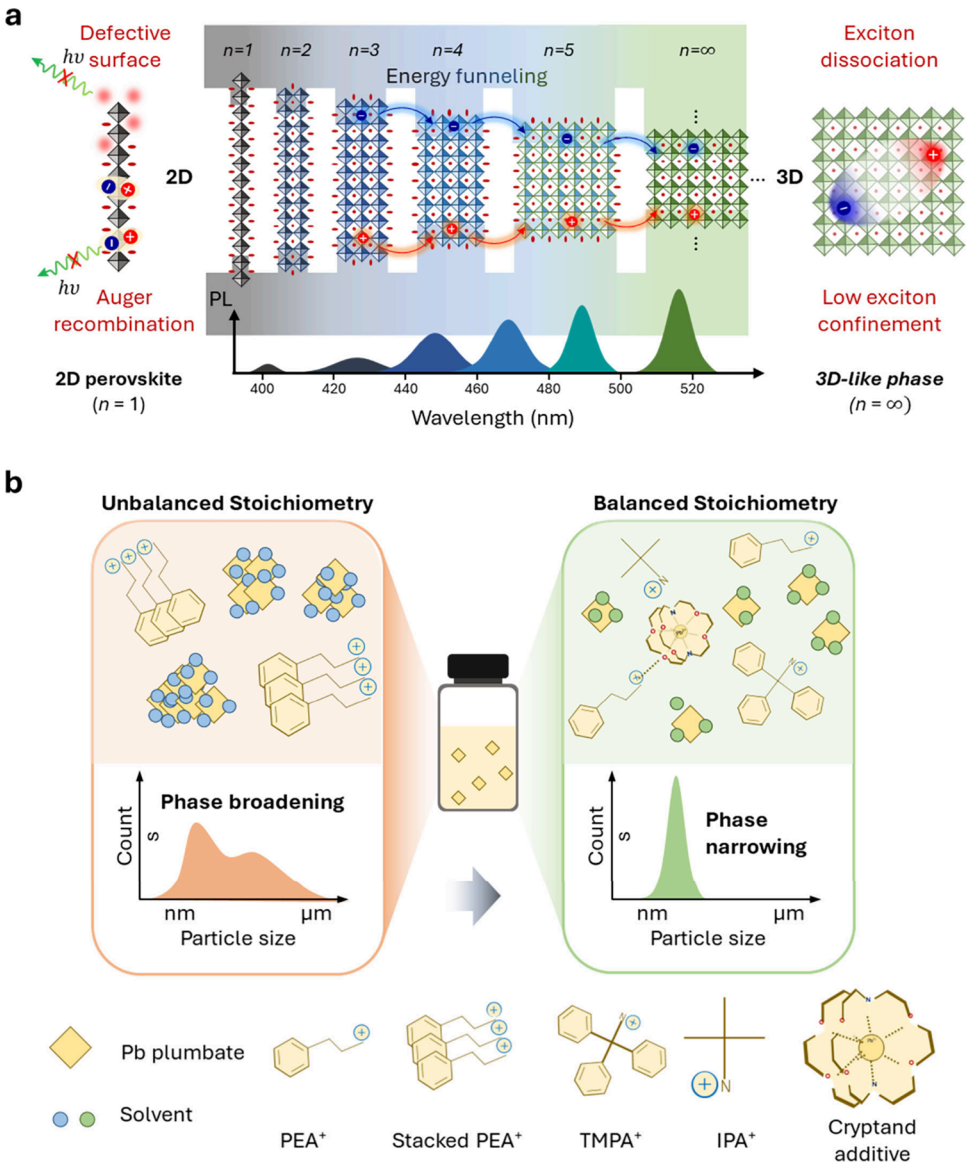


Figure 9. (a) Schematic of energy/carrier funneling in mixed quasi-2D perovskites, where photoexcited excitons transfer from wide-bandgap to narrow-bandgap phases. 3D-like ($n = \infty$) domains offer the lowest-gap recombination centers, but weaker confinement can increase trap-assisted losses under electrical bias, whereas monolayer 2D ($n = 1$) phases show stronger Coulomb interactions and defect sensitivity that can promote Auger and nonradiative recombination. (b) Additive-assisted precursor control for phase narrowing: suppressing precursor aggregation and homogenizing colloidal species reduces size dispersity, leading to a narrower n-phase distribution after crystallization.

distribution. When low-n phases are overrepresented, their larger spacer fraction, high density of organic−inorganic interfaces, and often poorer crystallinity can increase defect and trap densities, while stronger Coulomb interactions promote exciton−exciton annihilation and other Auger losses. These pathways compete with funneling and dissipate part of the excited population.[43,225] The high spacer content of low-n-rich films further lowers overall conductivity and aggravates the out-of-plane transport bottleneck, a limitation that becomes especially detrimental at the high current densities required for PeLEDs.[226] When present, 3D-like ($n = \infty$) domains occupy the bottom of the energy landscape and serve as weakly confined low-energy recombination sites for excitons and carriers, producing red-shifted emission that can degrade color purity, radiative efficiency, and operational stability.[4,227] The cascade therefore does not remove the need to control the n-distribution. Instead, it makes such control more important because the same mechanism that attenuates the spectral signature of phase polydispersity also routes the excited population into whichever domains lie lowest in energy.

Taken together, these three transport characteristics determine how device-level transport limitations manifest in quasi-2D PeLEDs. Limited out-of-plane transport raises the operating voltage needed to sustain a given current density, accelerating Joule heating and ion-migration-driven degradation.[37−39] The funneling cascade, meanwhile, concentrates injected carriers into the small population of emissive high-n domains, or into 3D-like domains in poorly controlled films, promoting Auger recombination and electrochemical side reactions that limit device operating lifetime at the high luminance levels (typically 10^2 -10^3 cd m^{-2}) required for display operation.[77,227] These coupled mechanisms point to three requirements for quasi-2D perovskite emitter design: (i) narrowing the n-distribution toward medium- or high-n domains

https://doi.org/10.1021/acs.chemrev.6c00202
Chem. Rev. XXXX, XXX, XXX−XXX

Downloaded from pubs.acs.org/chreay/article-pdf/doi/10.1021/acs.chemrev.6c00202/6880579/acs.chemrev.6c00202.pdf by guest on 10 October 2026

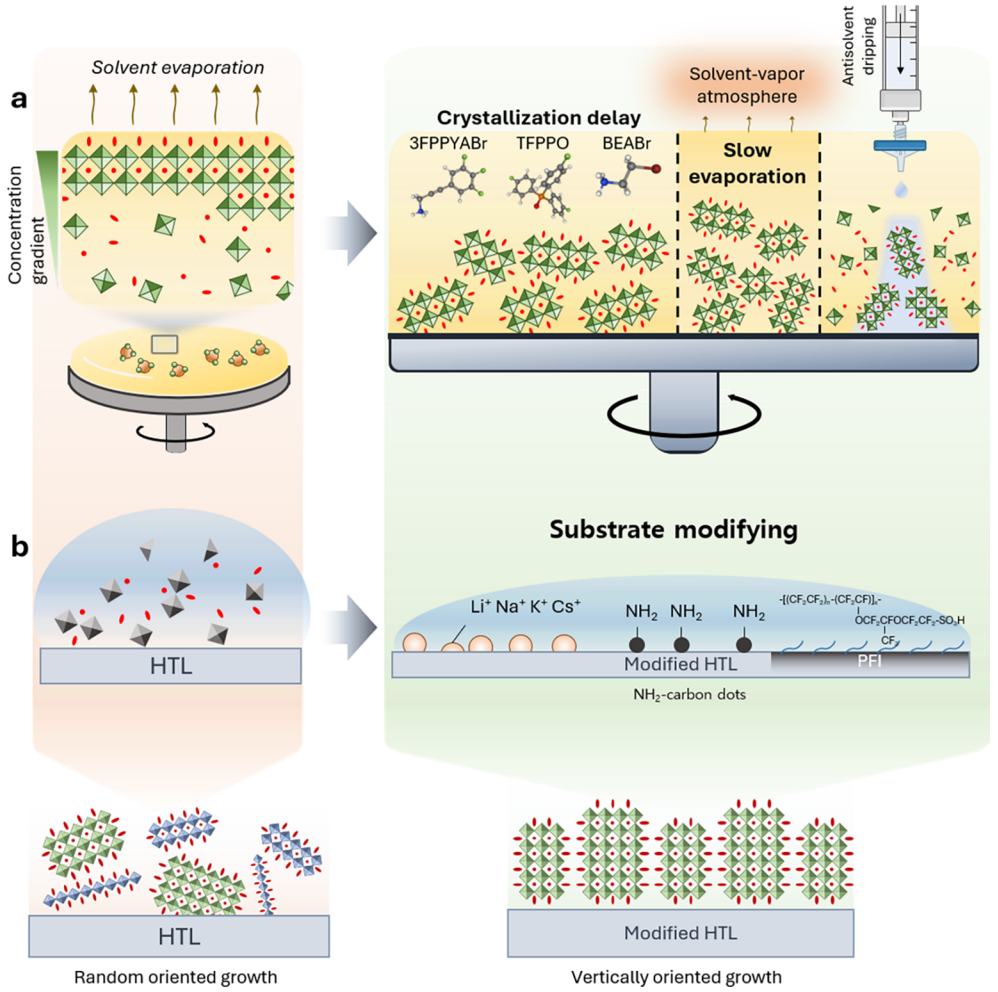


Figure 10. Nucleation-delaying additive, solvent engineering, synchronized nucleation by NCP, and interface-engineering strategies for phase narrowing in quasi-2D perovskites. (a) Schematic of strategies to control *n*-phase during spin-coating; nucleation-delaying additives, solvent-vapor atmosphere, and timed antisolvent dripping are used to moderate and then synchronize nucleation. (b) Schematic of substrate-guided nucleation control via HTL/interlayer modification, including ionic/functional additives and interfacial decoupling layers.

with sufficient confinement while limiting Auger losses and the formation of 3D-like low-energy sinks, (ii) orienting the inorganic slabs so that vertical current follows the in-plane channel, and (iii) engineering the buried interface, which influences both *n*-phase nucleation and slab orientation. The crystallization-control, additive, antisolvent, interfacial-engineering, and postprocessing strategies discussed below can each be understood as a different route toward these objectives.

5.2. Suppressing Precursor Aggregation and Speciation Heterogeneity

The *n*-phase distribution of quasi-2D perovskites is strongly affected by the precursor-solution state, before spin coating (Figure 9b).[237] During the crystallization of quasi-2D perovskites, multiple *n*-phases compete because their formation energies are often similar, leaving only a shallow thermodynamic driving force to select a single targeted *n*-value. The final *n*-phase ensemble is therefore additionally governed by crystallization kinetics, where solvent-Pb-X coordination/intermediate phases and the rate of supersaturation during spin-coating can kinetically bias early nuclei toward specific *n*-values.[227] The local A′ spacer cation aggregates[238] and heterogeneous solution speciation[239] which can create nucleation hot spots that preferentially stabilize certain *n*-phases, ultimately broaden the *n*-phase ensemble.

A′-spacer cations can readily self-aggregate in the precursor solution via π-π stacking,[4] van der Waals interactions,[240,241] and hydrogen-bond-assisted ion pairing,[242] creating spacer-rich local domains. During early crystallization, these local spacer-enriched regions lower the local nucleation barrier for low-*n* phases and induce nucleation toward strongly confined 2D motifs with more negative formation energies. Therefore, weakening spacer self-assembly by side-chain engineering reduces the thermodynamic driving force for 2D stacking, suppressing excessive low-*n* formation and helping narrow the *n*-phase distribution. This self-assembly leads to the A′ spacer cation-rich colloids, and these colloids create local A′-enriched regions during spin-coating, which favor early nucleation of low-*n* phases.[243] Therefore, suppressing A′ spacer cation-rich agglomerates is expected to mitigate excess low-*n* formation.

In addition to physically removing agglomerates via physical filtration, additives can be employed to suppress aggregation and thereby prevent *in situ* agglomerate formation. One practical strategy is cospacer engineering using a nonaromatic bulky A′ site cation without a conjugated ring tail.[224,240,244] For instance, the conventional aromatic spacer PEA^+ shows strong

https://doi.org/10.1021/acs.chemrev.6c00202
Chem. Rev. XXXX, XXX, XXX−XXX

Downloaded from pubs.acs.org/chreay/article-pdf/doi/10.1021/acs.chemrev.6c00202/68805793/acs.chemrev.6c00202.pdf by guest on 10 October 2026

interactions that can induce spacer cation aggregation, thereby promoting low-n phase formation.[224,240] Partial replacement of PEA^+ with a short-chain spacer (e.g., isopropylammonium) has been shown to suppress aggregation and narrow the n-phase distribution, consistent with an increased energetic penalty for forming the n = 1 phase.[224] Co-spacer designs using highly sterically hindered spacers (e.g., triphenylmethaneammonium) can further disrupt spacer stacking and suppress low-n nucleation.[240] In another approach, phase narrowing can be achieved without modifying the bulky A′ spacer cations by introducing an additive that interferes spacer−spacer interactions. For example, a cryptand that complexes with PEA^+ converts a bimodal colloidal size distribution into a single unimodal population, thereby homogenizing the precursor colloids and suppressing low-n phase formation.[244]

Pb-X-solvent coordination species can also form colloid-like aggregates, amplifying concentration and compositional gradients. Quasi-2D precursor solutions contain a diverse ensemble of plumbate complexes, and such heterogeneous speciation can translate into spatially varying nucleation conditions as solvent evaporation drives the solution toward supersaturation.[117,126] Such persistent heterogeneity increases the possibility that multiple n-phases nucleate and become kinetically locked in, resulting in undesirable low-n and 3D-like components.

Acids or zwitterionic additives can prevent the aggregation of Pb-X solvent species. Acids strongly interacting with Pb^{2+} can suppress aggregation by forming competitive Pb^{2+}-additive complexes, thereby reducing the population and size of colloidal aggregates.[245,246] Also, protonation by acid additives can change the local ionic coordination environment, which can promote partial dissolution or downsizing of the Pb-X framework.[247,248] This dual role of acidic additives can minimize precursor aggregation while steering nucleation toward a phase-narrowed crystallization pathway.[249] Even simple acids such as phenylphosphonic acid (PPA), which interacts with PbI_2, have been reported to reshape nucleation pathways and narrow n-phase distribution.[250] Zwitterions like 5-aminovaleric acid (5-AVA) can simultaneously coordinate Pb^{2+} and provide electrostatic/solvation stabilization, suppressing reagglomeration of Pb-X clusters and promoting a more uniform speciation landscape.[251] This homogenization reduces spatial variations in nucleation and growth during spin-coating, favoring phase narrowing.[251] A systematic study varied the acidic moiety of a zwitterionic additive (phosphonic acid, sulfonic acid, carboxylic acid, and thiol) and compared the resulting crystallization and device behavior.[162] The results indicate that excessively strong Pb^{2+} binding can impede growth or deteriorate crystallinity and morphology, necessitating an optimized binding strength window that balances aggregation suppression against growth inhibition.[162]

5.3. Crystallization Control

5.3.1. Coordination/Inhibitor-Mediated Nucleation Delay. Spin-coating dictates how the initial chemical distributions in the precursor are translated into an n-phase ensemble. Once the precursor is dispensed and spinning begins, the wet film rapidly thins under centrifugal force, while solvent evaporation progressively drives the solution toward supersaturation.[252] When a critical supersaturation is exceeded, nucleation is triggered in the quasi-2D perovskites. The first nucleation event strongly constrains the formation of n-phase distribution in the whole film, since the remaining precursor species after the initial nucleation act as the reservoir for subsequent growth and thereby bias the formation of the remaining quasi-2D phases.[253] Thus, controlling the nucleation timing, which can be achieved with crystallization delaying additives, solvent-vapor atmosphere, and antisolvent dripping, provides a practical route to narrow the n-phase distribution (Figure 10a).

During spin-coating, solvent is primarily removed from the top surface, inevitably generating vertical concentration gradients across the wet film, with higher concentrations at the surface and lower concentrations toward the substrate.[254,255] These gradients lead to biased local stoichiometry (A/A′), and Pb-X coordination/speciation. If nucleation begins before these gradients relax, different n-phases could be generated under locally biased conditions.[255,256] For example, A′ spacer cation-rich regions can preferentially trigger low-n nucleation by lowering the local nucleation barrier, whereas A′ spacer deficient regions may favor the growth of 3D-like components. Such early spatial nonuniformity can be imprinted into the solid film and ultimately manifests as a reason for broadened n-phase distribution.[257] Accordingly, the main objective of precursor engineering is to delay nucleation until the wet film reaches a more uniform chemical state, enabling nucleation to proceed more uniformly across the film.[255]

This nucleation delay can be implemented through three routes. First, competitive inhibitor-type additives can coordinate Pb^{2+} and/or interact with A/A′ cations, thereby retarding the conversion of solvated intermediates into the solid phase.[145,258] For instance, efficient Quasi-2D PeLEDs have been demonstrated using a fluorinated spacer cation 3-(3,4,5-trifluorophenyl)prop-2-yn-1-aminium bromide (3FPPYABr),[258] as well as by incorporating tris(4-fluorophenyl)phosphine oxide (TFPPO).[145] Although these molecules differ in structure and primary binding motifs, both can extend to the prenucleation window by stabilizing intermediate coordination states and reducing ion/cation mobility; for fluorinated spacers, this retardation is often attributed to $F\cdots NH_3^+$ interactions that slow spacer (e.g., PEA^+) diffusion/redistribution before nucleation.[258] Likewise, bifunctional spacer cation 2-bromoethylammonium bromide (BEABr) can also delay the crystallization, forming stronger coordination by hydrogen bonding and halogen−halogen bonding with $[PbBr_6]^{4-}$.[259] These strengthened interactions suppress the diffusion of molecules/ions during nucleation, which can efficiently slow the nucleation for the effective phase narrowing.[259] The resulting extended prenucleation window gives additional time to equilibrate intermediate phases throughout the film, reducing local spacer enrichment and suppressing premature low-n phase seeds.[260] In this sense, inhibitor additives not only slow down the crystallization, but they also help homogenize the chemical species in the prenucleation stage and make the favorable initial condition for the narrow phase distribution.[260,261]

5.3.2. Solvent-Removal and Solvation Engineering to Moderate Supersaturation. The second strategy is to engineer the solvent removal environment and solvent system to moderate how quickly the wet film reaches critical supersaturation. This approach aims to suppress rapid top-surface evaporation, thereby reducing vertical concentration gradients and locally biased stoichiometry/speciation that can otherwise become fixed before intermediates equilibrate across the wet film.[254] Regulating the solvent-vapor atmosphere during spin-coating has been shown to switch between distinct *in situ* crystallization modes by modulating solvent evaporation and

Downloaded from pubs.acs.org/chreav/article-pdf/doi/10.1021/acs.chemrev.6c00202/6880579/acs.chemrev.6c00202.pdf by guest on 10 October 2026

https://doi.org/10.1021/acs.chemrev.6c00202
Chem. Rev. XXXX, XXX, XXX−XXX

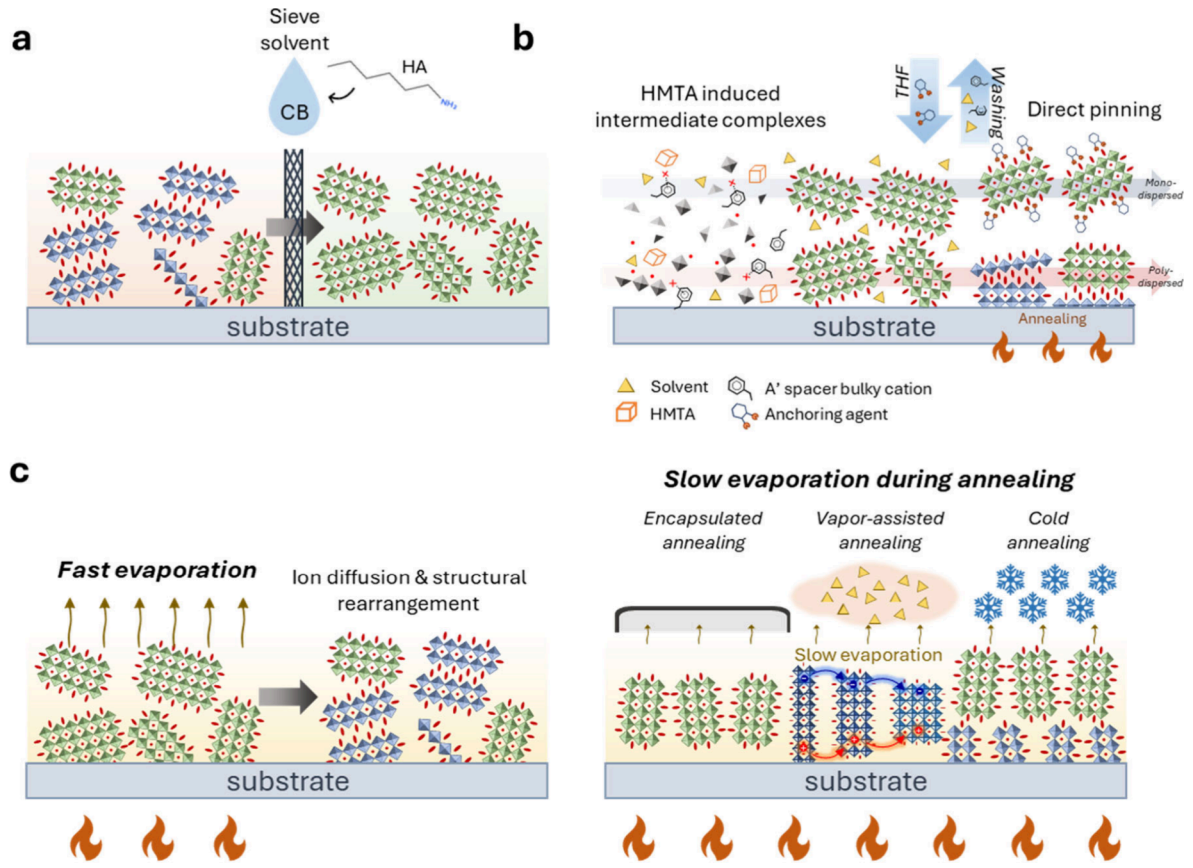


Figure 11. Postspin conditioning and annealing control for preserving a narrowed *n*-phase distribution in quasi-2D perovskite films. (a) Schematic of solvent-sieve postwashing applied to as-spun films to selectively dissolve unstable/defect-rich low-*n* components. (b) Schematic of intermediate-direct-pinning, where intermediate-rich films are briefly washed to remove excess intermediates/organics and residual solvents while an anchoring interaction kinetically pins the emerging phase ensemble. (c) Schematic comparison of annealing outcomes as a function of residual-solvent removal kinetics: fast evaporation can promote ion diffusion and structural rearrangement that broadens the phase ensemble, whereas slow-evaporation annealing modes (e.g., encapsulated, vapor-assisted, or temperature-field-controlled annealing) help preserve or steer the final *n*-phase distribution.

retention, indicating that nucleation is highly sensitive to the local solvent environment.[262] In addition, the *n*-phase distribution in quasi-2D perovskites can be tuned solely by regulating precursor supersaturation through solvent engineering (e.g., varying the DMSO/ethyl acetate ratio),[263] highlighting that phase selection depends not only on evaporation kinetics but also on solvent coordination and the overall solvation chemistry. Taken together, these results suggest that phase narrowing is not dictated only by spacer chemistry but also by how quickly the wet film approaches the nucleation threshold and how uniformly the solvent/solute speciation is maintained across the film before kinetic locking.

5.3.3. Antisolvent-Triggered Forced Supersaturation for Synchronized Nucleation. In contrast, antisolvent quenching promotes phase narrowing by synchronizing nucleation rather than delaying it.[264] By rapidly extracting the host solvent from the wet film, the antisolvent drives the precursor into a supersaturated state within a short time window, inducing rapid and widespread nucleation across the film.[260] Beyond acting as a purely kinetic quench, antisolvent processing can also chemically bias early stage phase selection by interacting with spacer cations and intermediate coordination species. Polar antisolvents such as ethyl acetate can engage in strong hydrogen-bonding interactions with spacer cations, thereby modulating crystallization and tailoring the phase distribution by suppressing excessive low-*n* components and promoting high-*n* growth.[265] From a practical standpoint, broadening the antisolvent processing window while preserving film quality is important for robust phase control. A green-solvent triethylene glycol (TEG) precursor system enables a wide antisolvent treatment time window (e.g., 70−100 s) while still yielding high-quality films and nearly identical device efficiencies, indicating that antisolvent-based phase control benefits from coupling forced supersaturation with a more forgiving kinetic window.[266] In addition, antisolvent dripping can serve as a timed delivery step for functional additives, enabling their introduction precisely at the nucleation and synchronization moment, and enabling concurrent phase regulation during the quench.[267,268]

5.3.4. Substrate-Guided Nucleation and Phase Distribution Control. Nucleation in quasi-2D perovskites is often heterogeneous across the film thickness and can be initiated preferentially at the buried interface via heterogeneous, interface-assisted nucleation. The buried interface can enrich precursor species through adsorption and local concentration, while interfacial wettability,[269,270] surface energy,[271] surface charge,[272] acidity,[273] and specific functional groups[271,274,275] can modulate interactions with Pb-X complexes and A-site cations (Figure 10b). These interfacial interactions reorganize the coordination environment of A/A′ cations and Pb-X species, reduce the effective nucleation barrier, and stabilize interfacial nuclei. Buried-interface nucleation therefore determines the

Downloaded from pubs.acs.org/chreav/article-pdf/doi/10.1021/acs.chemrev.6c00202/68805793/acs.chemrev.6c00202.pdf by guest on 10 October 2026

https://doi.org/10.1021/acs.chemrev.6c00202
Chem. Rev. XXXX, XXX, XXX−XXX

spatial distribution of nuclei and early stage phase selection, and in some cases, can contribute to phase narrowing while improving film continuity and coverage.[276] In practice, CTL-based buried-interface engineering can also influence charge injection and transport, imposing constraints or enabling synergistic gains depending on the interlayer design.[277−279] Buried-interface nucleation is commonly promoted by incorporating monovalent metal cations (Li^+,[280] Na^+,[281] K^+,[96] Cs^+[277]) as functional additives in the hole-transport layer. Additives bearing passivating groups can effectively reduce defect densities at the buried interface while simultaneously refining the phase distribution. These additives can reorganize the local Pb-X coordination environment and suppress interfacial compositional heterogeneity, thereby reducing premature nucleation of low-*n* phases or 3D-like domains at the interface. Suppression of these early pathways favors the formation of a more continuous medium-*n* network and results in a narrower phase distribution. Ionic salt additives formed via ionic pairing between monovalent metal cations and functional anions have been widely reported as a strategy enabling simultaneous nucleation promotion and interfacial passivation.[96,280]

Beyond phase regulation, buried interface nucleation can also modulate the crystal orientation, which constitutes a major bottleneck for carrier transport in quasi-2D perovskites. The in-plane orientation of layered perovskites impedes vertical carrier transport, whereas interface-directed nucleation, promoting out-of-plane growth, improves vertical transport pathways. The introduction of amine-terminated carbon dots into the hole transport layer has been reported to reduce phase inhomogeneity in quasi-2D blue PeLEDs while promoting out-of-plane growth through specific interfacial interactions. The resulting vertically aligned nanostructures, with a markedly reduced effective grain boundary density, have been associated with substantial improvements in carrier transport across the emissive layer.[282]

Another powerful approach to phase narrowing is to decouple the quasi-2D precursor from the buried interface, thereby suppressing substrate-imposed biases in the nucleation and phase selection. The insertion of an interfacial decoupling layer weakens the adsorptive and specific interfacial interactions that locally reorganize the Pb-X coordination and PEA^+ distributions. This, in turn, mitigates the tendency for preferential low *n* enrichment or heterogeneous phase separation at the interface. A perfluorinated ionomer (PFI) between the PEDOT:PSS and the EML mitigates the adverse influence of the substrate on phase distribution, yielding a more ordered *n*-phase landscape and substantially improved radiative efficiency in blue quasi-2D PeLEDs.[278]

5.4. Postprocessing to Refine *n*-Phases and Prevent 3D-Like Phase Growth

Although spin-coating can largely determine the nucleation timing and thereby preconfigure the initial *n*-phase distribution, as-spun quasi-2D perovskite films often remain in a semi-equilibrated state that still contains residual solvents and labile Pb-X coordination species. During this short postspin period, remnants of locally trapped low-dimensional phases—or seeds that later promote low-*n* formation during thermal annealing—can persist. Therefore, post-treatments applied in the narrow time window between the end of spin-coating and the onset of annealing can be viewed as a preconditioning step that (i) selectively dissolves unstable or defect-rich low-*n* components[283,284] or (ii) kinetically pins the precursor-derived distribution before thermally activated redistribution sets in.[30] A representative example (Figure 11a) is solvent sieve chemical washing,[283] in which a small fraction of hexylamine (HA) is blended into chlorobenzene and applied to the as-spun film, selectively removing defect-rich low-*n* phases and narrowing the *n*-phase dispersion.[283] This approach has also been correlated with markedly improved operational stability at high brightness; notably, an extrapolated T_{50} of ∼5.7 years at 100 cd m^{-2} has been reported alongside high efficiency, suggesting that postspin treatment can provide benefits beyond simple phase narrowing.[283,284]

Conceptually related, an alternative route is to intentionally halt quasi-2D phase formation after spin-coating and then trigger phase formation only after removing intermediates that would otherwise bias the film toward low-*n* phases. In the anchoring-assisted intermediate-direct-pinning (A-IDP) strategy (Figure 11b),[30] methylenediammonium dichloride ($MDACl_2$) in the precursor rapidly degrades into NH_4^+ and hexamethylenetetramine (HMTA), forming a metastable intermediate complex with PEA^+ and retarding low-*n* crystallization.[30] The intermediate-rich film is then washed with a semipolar, volatile solvent of tetrahydrofuran (THF) containing a surface-anchoring ligand, 1,2-*cis*-cyclohexyl dicarboxylic acid (CCA), which allows selective removal of excess intermediate/organic species and residual solvents, while simultaneously anchoring and pinning the emerging phase distribution to suppress diffusion-driven broadening during annealing.[30]

Even when the initial distribution is refined by such post-treatments, thermal annealing remains essential for removing residual solvents (e.g., DMF/DMSO) and stabilizing the crystal lattice for LED fabrication. However, because different quasi-2D *n* phases are often thermodynamically close in free energy, annealing can promote ionic redistribution and structural rearrangement, leading to additional phase redistribution. Thus, the key objective of postspin processing is (i) to preserve an already narrowed *n*-phase distribution during annealing and (ii) to further steer the final distribution through rationally designed annealing conditions.

One handle is to control the evaporation kinetics of residual solvents during annealing (Figure 11c). In encapsulation annealing (or encapsulation growth), the wet film is physically covered to retain coordinating solvent (e.g., DMSO) for longer, which can redirect the subsequent crystallization pathway: the contribution of low-dimensional domains decreases while the fraction of higher-*n*/3D-like components increases, consistent with a reshaped domain distribution reflected in near-band-edge absorption features.[285] Another handle is the deliberate design of the solvent atmosphere during annealing. Solvent vapor can open partial dissolution-recrystallization pathways and strongly affect the final phase distribution and defect formation. Notably, quasi-2D perovskite films can respond very differently under polar/nonpolar solvent atmospheres, implying that vapor polarity and coordination strength can either accelerate phase evolution/degradation or help preserve/improve phase purity, depending on the system.[286] Extending this concept, mixed-vapor annealing that combines a coordinating component with a nonpolar/weakly interacting component has been proposed to buffer intermediate-to-crystal conversion while enabling reorganization time. For instance, $DMSO/CS_2$ mixed vapor was shown to promote more thermodynamically controlled crystallization and a well-aligned cascade-like phase arrangement. CS_2 adsorption was also associated with a reduced surface

Downloaded from pubs.acs.org/chreav/article-pdf/doi/10.1021/acs.chemrev.6c00202/68805793/acs.chemrev.6c00202.pdf by guest on 10 October 2026

https://doi.org/10.1021/acs.chemrev.6c00202
Chem. Rev. XXXX, XXX, XXX−XXX

Table 3. Summary of Quasi-2D Perovskite Light-Emitting Diodes

Composition	EL peak (nm)	Luminance (cd m^{-2})	EQE (%)	$V_{on}/V_{1,000\ nit}/V_{10,000\ nit}$ [a] (V)	Operational lifetime (T_{50})	Strategy	Molecular additive	Ref.
(FA/Cs) Pb (Br/Cl)-p-FPEABr LiBr, GABr, NaBr	458	3,521	5.82	4.1/-/-	13.4 min @ 19.17 cd m^{-2}	Annealing engineering	-	287
(Cs/EA)$PbBr_3$ + PEABr +$MDABr_2$	489	1,000	22.5	2.3/3.0/-	2.5 h @ 100 cd m^{-2}	Molecular additive	MDA^{2+}	30
						Post-treatment	CCA	
(Cs/MA)$PbBr_3$ + PEA/IPABr	490	2,480	1.5	5.4/8.0/-	10 min @ 10 cd m^{-2}	Ligand engineering	IPABr	224
(Cs/GA)$Pb(Br/Cl)_3$ + PEABr	490	2,686.45	10.16	3.4/5.5/-	240 s @ 100 cd m^{-2}	Molecular additive	Cryptand	244
(Cs/EA)$PbBr_3$ + PEABr	490	2,150	15.6	3.0/4.3/-	55.3 min @ 60 cd m^{-2}	Molecular additive	GABA	162
(Cs/PA)$PbBr_3$ + PEA/ 3FPPYABr	490	1119	12.26	2.3/5.3/-	0.88 min @ 60 cd m^{-2}	Molecular additive	3FPPYABr	258
$CsPbBr_3$ + PEABr + BABr	490	3,194.7	8.77	3.2/5.0/-	5.58 min @ 37 cd m^{-2}	Antisolvent engineering	Ethyl Acetate	265
$CsPbBr_3$ + PEA/BEABr	493	2,540	16.98	3.0/4.0/-	730 s @ 0.5 mA cm^{-2}	Ligand engineering	BEABr	259
$CsPbBr_3$ + PMABr	493	8,300	12.8	2.8/3.6/4.5	-	Annealing engineering	Scotch Tape	285
(Cs/EA)$PbBr_3$ + PEABr	494	~9,000	12.09	2.3/3.0/-	1.9 h @ 100 cd m^{-2}	Interface engineering	PFI	278
$CsPbBr_3$ + PBA/PEABr	515	-	14.6	2.8/4.9/-	700 s @ 200 cd m^{-2}	Solvent engineering	-	262
$Cs_{1.6}MA_{0.4}Pb_3Br_{10}$ + PEABr	517	52,000	25.6	2.8/3.0/3.4	115 min @ 7,200 cd m^{-2}	Molecular additive	TFPPO	145
$CsPbBr_3$ + PEABr	520	5,000	24.27	2.5/4.9/5.9	-	Vapor-assisted annealing	Chlorobenzene	286
$FAPbBr_3$ + PEABr + CF_3SO_3K	531	147,872.8	29.5	2.6/3.2/3.7	50,317 h @ 100 cd m^{-2}	Post-treatment	Hexylamine	283
$FAPbBr_3$ + PEABr + KBr	532	38,000	20.4	2.8/3.3/4.0	-	Interface engineering	TEG	266
						Solvent engineering		
$CsPb(Br/I)_3$ + PEABr	656	3,024	32.14	5.8/6.4/-	47.7 h, 60.0 h, 43.7 h @ 5 mA cm^{-2}	Vapor-assisted annealing	DMSO CS_2	36

[a]Turn-on voltage (V_{on}) and driving voltages at 1,000 and 10,000 cd m^{-2} ($V_{1,000\ nit}$ and $V_{10,000\ nit}$) were extracted by digitization from the $J-V-L$ curves of the corresponding references. IPABr (isopropylammonium bromide); GABA (γ-aminobutyric acid); 3FPPYABr (3-(3,4,5-trifluorophenyl)prop-2-yn-1-aminium bromide); TFPPO (tris(4-fluorophenyl)phosphine oxide); BEABr (2-bromoethylamine hydrobromide); TEG (triethylene glycol); PFI (perfluorinated ionomer); MDA^{2+} (methylenediammonium); CCA (1,2-cis-cyclohexyl dicarboxylic acid)

defect density, leading to improved spectral stability and device performance.[36]

Finally, the annealing temperature field itself can be engineered to directly modulate the vertical phase distribution. Thermal-gradient annealing, implemented by introducing a low-temperature source during annealing, was reported to suppress the formation and accumulation of high-n domains near the upper interface and to realize a more favorable vertical distribution for efficient emission.[287] The performance of quasi-2D PeLEDs is summarized in Table 3.

6. COLLOIDAL PEROVSKITE NANOCRYSTALS

In colloidal PNCs, interparticle charge transport is intrinsically limited by the insulating organic ligands required for surface passivation and colloidal stability. Charge transport proceeds primarily via thermally activated hopping across a structurally and energetically heterogeneous network.[288] This inefficient transport mechanism often results in nonuniform internal electric fields, promoting local charge accumulation, which accelerates device degradation. Therefore, the main material design objective for this system is to maintain confinement and surface passivation while improving the interparticle transport.

To mitigate these transport limitations, ligand exchange strategies are utilized to replace native insulating ligands, such as oleic acid (OA) and oleylamine (OAm),[289] with shorter or more conductive structures.[290] Although these approaches improve carrier mobility, the structural disorder inherent in randomly packed films persists as a primary limiting factor. Consequently, long-range ordering of colloidal PNCs has been investigated to manage this issue.[291] Ordered assemblies minimize energetic disorder and facilitate charge carrier transport while preserving charge confinement and preventing leakage current.[292−295] The formation of such ordered structures is fundamentally dependent on nanocrystal monodispersity and the interaction between ligands.[294] Therefore, precise control over the size distribution and ligand engineering is essential for the assembly of coherent, long-range ordered superlattices. In this context, this section discusses synthesis approaches aimed at obtaining monodisperse colloidal PNCs, followed by an examination of purification and ligand engineering strategies designed to balance passivation and charge transport. Finally, the perspective of long-range PNC ordering to form a superlattice is summarized.

Conventional synthesis methods for perovskite nanocrystals (PNCs) include hot injection, room-temperature synthesis, ligand-assisted reprecipitation (LARP), and emulsion techniques. Hot-injection and room-temperature synthesis typically involve the reaction of two precursor solutions, dissolved in nonpolar solvents, with ligands. Typically, an A-site cation or

Downloaded from pubs.acs.org/chreav/article-pdf/doi/10.1021/acs.chemrev.6c00202/68805793/acs.chemrev.6c00202.pdf by guest on 10 October 2026

https://doi.org/10.1021/acs.chemrev.6c00202
Chem. Rev. XXXX, XXX, XXX−XXX

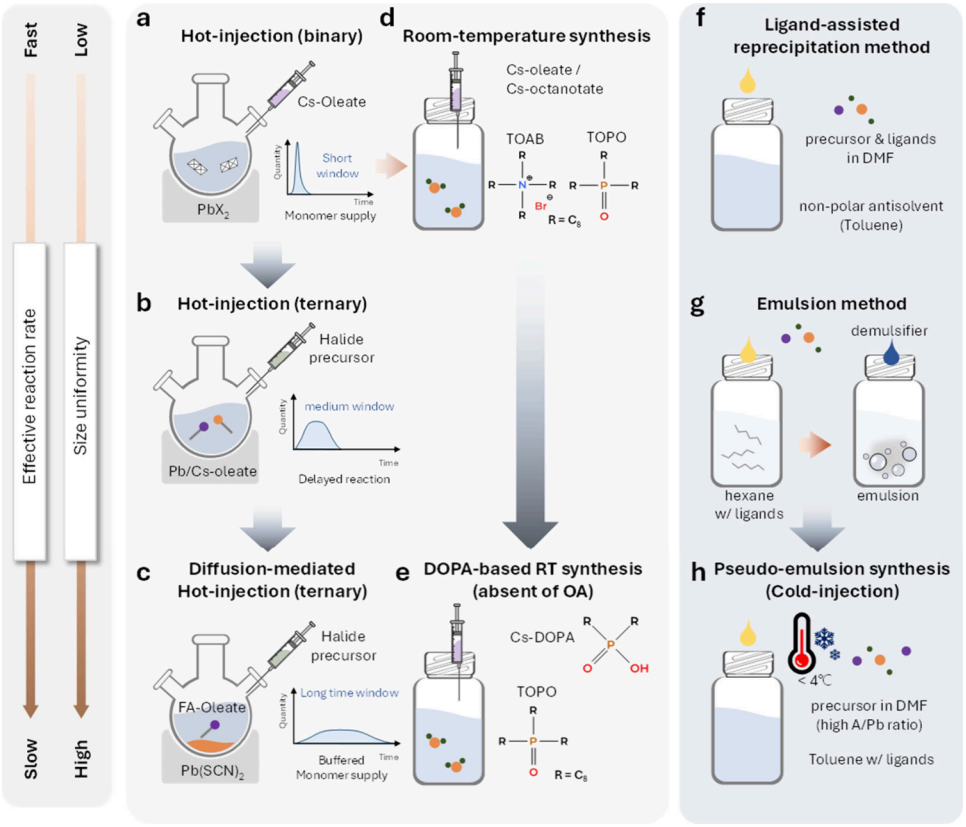


Figure 12. Development of fabrication methods for perovskite nanocrystals (PNCs). The left arrows indicate the overall trend that a slower effective reaction rate leads to higher size uniformity. (a–c) Schematics of hot-injection methods. (a) The conventional binary system injects Cs-oleate into the Pb-halide precursor, resulting in rapid reaction and growth with a short monomer supply window. (b) The ternary hot-injection system utilizes halide precursor injection into Cs/Pb-oleate, which slows down the reaction rate. (c) In the diffusion-mediated hot-injection method, the limited solubility of $Pb(SCN)_2$ provides monomers continuously. This significantly slows down the reaction rate and forms monodisperse PNCs. (d, e) Schematics of room-temperature (RT) synthesis. (d) PbX_2 is dissolved with the aid of organic additives such as tetraoctylammonium bromide (TOAB) or trioctylphosphine oxide (TOPO). Nucleation and growth are initialized by the Cs-precursor injection. (e) In diisooctylphosphinic acid (DOPA)-based RT synthesis, the absence of OA delays the dissociation of the PbX_2-TOPO complex, thereby slowing down the growth and yielding monodisperse PNCs. (f–h) Schematics of synthesis methods utilizing solubility differences. (f) The ligand-assisted reprecipitation method utilizes a polar precursor solution (in DMF) where perovskite precursors and ligands are dissolved together, which is then injected into toluene acting as a nonpolar antisolvent. (g) The emulsion method utilizes hexane with ligands as an antisolvent, and the immiscibility between hexane and the polar precursor solution leads to an emulsion state. Nucleation and growth are initialized after a demulsifier is injected. (h) The pseudo-emulsion synthesis (cold-injection method) utilizes a precursor solution in DMF (high A/Pb ratio) without ligands, and toluene with ligands as the antisolvent, while maintaining a low solution temperature below 4 °C.

halide anion[296,297] precursor is injected into a lead halide (PbX_2) precursor solution. In contrast, LARP[298,299] and emulsion methods[300] use perovskite precursors dissolved in polar solvents, which are subsequently injected into an antisolvent. These approaches rely on the precipitation of PNCs driven by differences in the solubility. The strategies for controlling PNC growth differ, depending on the specific mechanism governing each synthetic route.

6.1. Nucleation and Growth Control in Colloidal PNCs

6.1.1. Hot-Injection Synthesis. The conventional hot-injection method involves the rapid injection of a cesium oleate (Cs-oleate) solution into a heated PbX_2 precursor containing OA and OAm (Figure 12a).[289] Cs-oleate is generally prepared by reacting cesium carbonate or cesium acetate with OA under vacuum at temperatures exceeding 100 °C. FA-based compositions can be synthesized using a similar procedure by substituting Cs-oleate with FA-oleate.[301,302]

The nucleation and growth kinetics are primarily governed by the interaction between OA/OAm ligands and PbX_2. Acid–base interactions modulate the coordination environment of Pb^{2+} and halide anion.[303] Because the reaction between OA and OAm is exothermic, the concentration of ionized ligand species ($R\text{-}COO^-$ and $R\text{-}NH_3^+$) increases at lower reaction temperatures.[304] These ionized species bind strongly to the precursors and reduce ionic mobility. This interaction limits the formation of haloplumbates and suppresses both crystallization and growth.[303] Conversely, increasing the reaction temperature for the synthesis of PNCs decreases the concentration of ionized ligand species. This reduction lowers PbX_2 solubility and promotes the formation of haloplumbates.[303] Upon the injection of Cs-oleate, these plumbate species convert rapidly into $CsPbX_3$ nanocrystals. These nucleation and growth processes typically reach completion within seconds. This rapid rate makes precise size control difficult and often results in broad size distributions.[305]

Zinc halides (ZnX_2) are frequently added to the precursor solution to improve the size uniformity. Upon dissolution by OA/OAm, ZnX_2 provides additional halide species, while the Zn^{2+} ions act as spectator species that do not incorporate into the perovskite lattice. Under halide-deficient conditions, such as

https://doi.org/10.1021/acs.chemrev.6c00202
Chem. Rev. XXXX, XXX, XXX–XXX

Downloaded from pubs.acs.org/chreay/article-pdf/doi/10.1021/acs.chemrev.6c00202/68805793/acs.chemrev.6c00202.pdf by guest on 10 October 2026

a Pb:X ratio of approximately 1:2, incomplete halide coordination promotes Pb-rich terminations in the plumbates. This condition favors continued growth and broadens the size distribution.[214,305] In contrast, halide-rich conditions induce high-order coordination in the Pb-X species. This effect reduces the effective growth rate and suppresses the uncontrolled size evolution. Consequently, halide-rich conditions typically yield more confined nanocrystals with an improved size uniformity.[214,305] However, this strategy is limited in its ability to regulate the rapid kinetics required for larger PNCs, specifically, those exceeding 10 nm.

The reaction can be further decelerated by modifying the system from a binary to a ternary precursor system (Figure 12b). In this arrangement, Cs^+ and Pb^{2+} are provided as oleate salts, and nucleation is initiated by injection of a halide source.[289,296,306] The reaction rate decreases because the strong bonds between Pb and the oleate ligands must be broken before the formation of haloplumbates during the initial stage of the halide precursor injection. For the halide source, oleylammonium halides[299] were initially employed, and benzoyl halides have more recently been utilized as alternative molecular precursors.[296] Benzoyl halides undergo a chemical reaction to release halide ions gradually, enabling slower growth and superior size uniformity.[296]

The ternary system was further extended through a diffusion-mediated hot-injection strategy using lead thiocyanate ($Pb(SCN)_2$) (Figure 12c). Unlike PbX_2, $Pb(SCN)_2$ exhibits limited solubility due to strong Pb-SCN interactions and functions as a monomer reservoir.[306] As soluble monomers are consumed during nanocrystal growth, additional $Pb(SCN)_2$ dissolves to replenish the monomer pool, and this buffered monomer concentration promotes size-focused growth.[306] Under these diffusion-limited conditions, smaller nanocrystals grow more rapidly than larger ones, which suppresses Ostwald ripening and allows the reaction time to be extended over tens of minutes. This approach results in narrow size distributions with standard deviations of below 8%.[306]

6.1.2. Room-Temperature Synthesis. Hot-injection synthesis remains a widely used protocol for the preparation of phase-pure colloidal nanocrystals. However, the requirement for high reaction temperatures and inert or vacuum conditions increases the processing complexity. These limitations have prompted the development of room-temperature synthesis methods that can be carried out under ambient conditions (Figure 12d).

To enable the formation of perovskite at room temperature, alternative ligand systems are required. Initial room-temperature synthesis utilized tetraoctylammonium bromide (TOAB) to facilitate the solvation of $PbBr_2$ in toluene.[205] In this process, TOAB provides Br^- to $PbBr_2$ to form highly coordinated haloplumbates, while the large organic cation TOA^+ stabilizes the species dispersed in toluene. Subsequent injection of Cs-octanoate (Cs-OTAc) leads to the formation of colloidal PNCs. Because TOA^+ acts as a weakly binding ligand, the system maintains a high reaction rate by allowing Cs^+ to coordinate directly to the plumbates. TOPO or tetraheptylammonium iodide (THAI) along with oleylammonium iodide have been utilized as alternative coordinating agents for PbX_2 in room-temperature synthesis.[307−309]

To modulate the reaction rate, the choice of ligand directly influences the interaction between the Cs precursor and PbX_2. In room-temperature synthesis utilizing the TOPO system, replacing OA or OTAc with diisooctylphosphinic acid (DOPA) is a critical factor. When the TOPO forms the TOPO-$PbBr_2$ complex, conventional carboxylic acids exhibit high affinity for TOPO. These acids protonate TOPO to form TOPO-H, which immediately induces the formation of haloplumbates and initiates rapid nucleation and growth. In contrast, DOPA has a low affinity for TOPO, which prevents the abrupt formation of haloplumbates. Instead, upon injection of Cs-DOPA, a Cs-$[PbBr_3]$ complex is formed. This pathway facilitates the slow, controlled growth of colloidal nanocrystals (Figure 12e).[310]

6.1.3. Antisolvent Precipitation and Emulsion Synthesis. While conventional hot-injection or room-temperature methods utilize separate precursor solutions in nonpolar solvents, the LARP technique employs polar solvents such as DMF to dissolve perovskite precursors alongside amine and acid ligands. In this approach, PNCs are synthesized by injecting the polar precursor solution into a nonpolar antisolvent. The abrupt reduction in solubility upon injection triggers the rapid precipitation of precursors, resulting in the formation of the perovskite phase (Figure 12f).[298,299] A related strategy utilizes precipitation within a precursor emulsion. For instance, hexane is utilized as an antisolvent, and the immiscibility of DMF and hexane leads to a milky emulsion state of the precursor solution. To initiate precipitation, a demulsifier such as tert-butanol or acetone is introduced to the system, facilitating the isolation of the PNCs (Figure 12g).[300]

Control over nanocrystal dimensions and morphology is primarily achieved through ligand management. It has been observed that increasing the alkyl chain length of the amine ligand from butylamine to octylamine in the presence of OA reduces the size of spherical PNCs to below 10 nm.[290] Similarly, increasing the concentration of OA in the antisolvent has been demonstrated to decrease the size of PNCs from 35 to 3 nm.[311] Beyond size regulation, the specific choice of ligand species can be used to tune the nanocrystal shape. This enables the synthesis of diverse morphologies including spherical quantum dots, nanocubes, nanorods, and nanoplatelets.[312−314] However, these methods are also governed by sudden changes in solubility, which often lead to limited control over nucleation and result in nonuniform particle synthesis.

6.1.4. Cold-Injection and Pseudo-emulsion Synthesis. While conventional precipitation and emulsion methods have been limited by poorly understood nucleation kinetics, the recently developed cold injection (Ci) method addresses these limitations. By utilizing a pseudo-emulsion method,[31] this synthesis method produces $(FA/GA)PbBr_3$ PNCs featuring near-unity PLQY and high structural uniformity.

The coordination environment of the precursor solution, specifically the $ABr/PbBr_2$ ratio ranging from 1:1 to 2:1, significantly influences the resulting nanocrystal properties. At low $ABr/PbBr_2$ ratios, haloplumbates exhibit low coordination numbers and tend to aggregate into large, polydisperse colloids through interplumbate interactions. Conversely, increasing the $ABr/PbBr_2$ ratio promotes higher Pb^{2+} coordination, where the Pb centers are effectively shielded by the A-site cations. This shielding results in smaller, more uniform plumbate species that suppress rapid nucleation and uncontrolled growth upon injection into the antisolvent, ultimately leading to enhanced PLQY.[31]

The reaction temperature and ligand concentration within the antisolvent also serve as critical parameters for growth control. Because the acid−base exchange reaction between ligands is exothermic, lower injection temperatures increase the effective concentration of decylammonium and oleate species in the

Downloaded from pubs.acs.org/chreay/article-pdf/doi/10.1021/acs.chemrev.6c00202/68805793/acs.chemrev.6c00202.pdf by guest on 10 October 2026

https://doi.org/10.1021/acs.chemrev.6c00202
Chem. Rev. XXXX, XXX, XXX−XXX

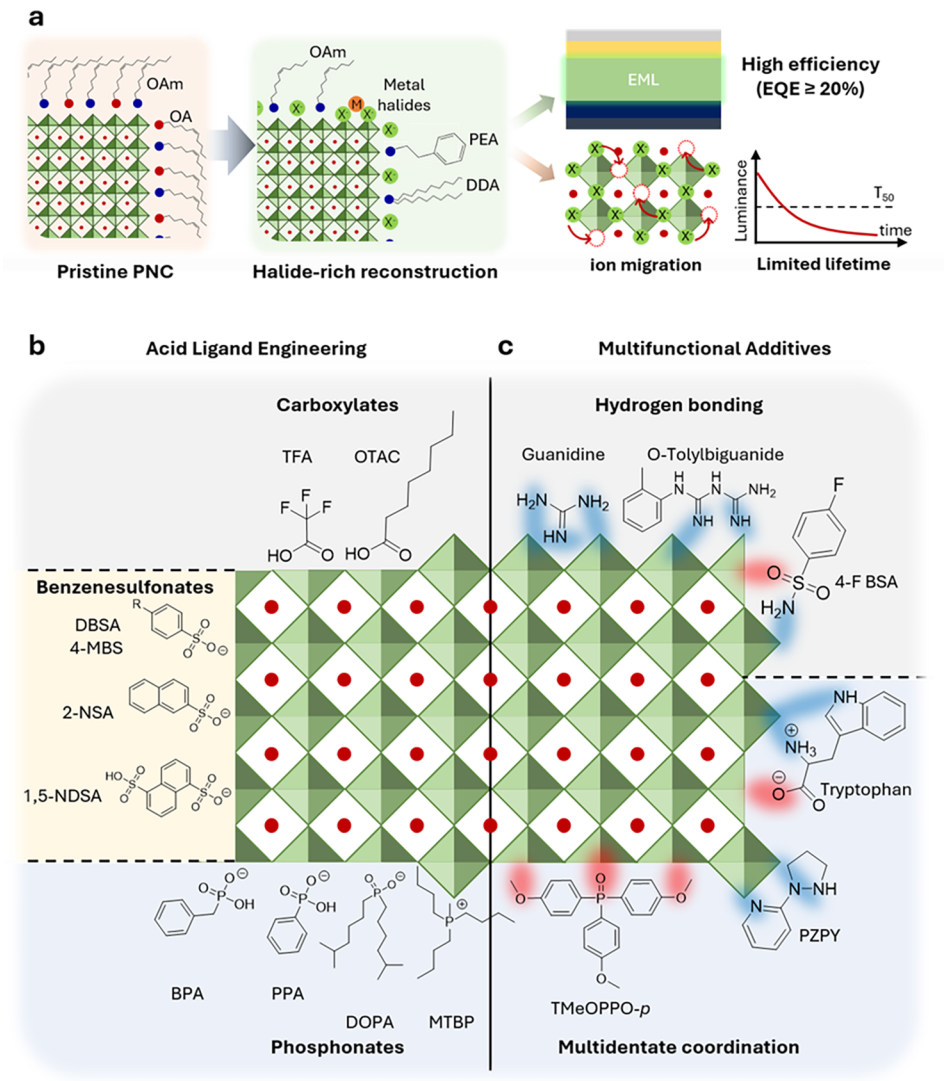


Figure 13. Surface engineering strategies for perovskite nanocrystals (PNCs). (a) Conventional surface ligand engineering trends. Replacing pristine insulating ligands (OA, OAm) with halide-rich surfaces facilitates high external quantum efficiency (EQE), but leaves the structure vulnerable to ion migration, resulting in limited operational lifetime. (b) Promising surface engineering strategies utilizing acidic ligands. Carboxylate, benzenesulfonate, and phosphonate ligands are employed to strongly anchor to the PNC surface, substituting vulnerable halide anions to enhance structural durability and charge transport. (c) Multifunctional additives. Implementing molecules capable of hydrogen bonding or multidentate coordination to provide robust surface passivation and reinforce the structural stability of the ionic lattice.

antisolvent. Upon introduction of the precursor solution, these high ligand concentrations, coupled with the reduced mobility of emulsifier molecules, prevent immediate precipitation at a low temperature. This stabilizes the pseudo-emulsion state for an extended duration, thereby slowing the growth kinetics.[31] The resulting PNCs exhibit uniform cuboid morphologies, in contrast to the noncuboid shapes and wide size distributions typically observed in room-temperature syntheses.

6.1.5. Purification. Postsynthetic purification and ligand engineering are necessary to utilize as-synthesized colloidal PNCs as an emissive layer. The purification process removes reaction residues, including high-boiling-point solvents such as 1-octadecene (ODE), excess ligands (e.g., OA, OAm, TOAB, and TOPO), nonperovskite phases, and unreacted clusters. Failure to remove these impurities prevents the formation of uniform, compact PNC films and results in highly insulating electrical properties.

Standard purification protocols typically employ a reprecipitation method using polar antisolvents such as ethyl acetate or methyl acetate.[315,316] In early studies, various solvents, including butanol and acetone, were investigated; however, their highly polar or protic nature often resulted in the generation of surface defects and the degradation of the perovskite lattice.[316] Consequently, ethyl acetate and methyl acetate have been established as the standard solvents for purification.

The purification procedure involved repeated cycles of precipitation and redispersion. By optimization of the antisolvent-to-crude solution ratio, colloidal PNCs can be selectively extracted. During centrifugation, larger impurities are discarded as precipitates, while the ODE, excess ligands, and small clusters are removed in the supernatant. It was observed that two washing cycles are generally sufficient to isolate the pure colloidal PNCs. Excessive washing should be avoided as it promotes the detachment of surface ligands, leading to a loss of colloidal stability and the formation of nonradiative surface traps.[317]

While the synthesis and purification protocols enable the production of monodisperse PNCs without residue, the

Downloaded from pubs.acs.org/chreay/article-pdf/doi/10.1021/acs.chemrev.6c00202/6880579/acs.chemrev.6c00202.pdf by guest on 10 October 2026

https://doi.org/10.1021/acs.chemrev.6c00202
Chem. Rev. XXXX, XXX, XXX−XXX

resulting nanocrystals remain capped with long-chain aliphatic ligands. Their insulating nature presents a significant barrier to charge carrier injection and transport in optoelectronic devices. Consequently, postsynthetic surface modification becomes necessary to provide effective defect passivation during purification. The following section discusses ligand engineering strategies designed to replace or modify these initial ligand shells.

6.2. Surface Engineering

Ideal surface ligands for colloidal PNCs must satisfy three primary criteria: 1) providing sufficient steric or electrostatic repulsion to ensure colloidal stability and prevent agglomeration; 2) exhibiting strong surface binding to effectively passivate defects and resist detachment; and 3) ensuring high conductivity to facilitate efficient charge injection and transport.

During the early stages of colloidal PNC development, research was directed toward substituting native OA and OAm ligands (Figure 13a). Because halide vacancies were identified as the predominant surface defects, strategies primarily focused on the supplementation of halide anions, typically paired with alkylammonium countercations or metal halides.[318−321] This approach was effective. For instance, postsynthetic treatment with oleylammonium halides was sufficient to achieve an EQE exceeding 20%.[321] Furthermore, quaternary ammonium halides, such as didodecyldimethylammonium bromide (DDAB), have been widely adopted as exchange ligands. Compared to native ligands, DDAB exhibits stronger binding energy and enhanced chemical robustness against acid−base equilibria due to its quaternary ammonium structure.[322,323]

Despite these improvements in device efficiency, a limited operational lifetime remains a significant challenge. Native carboxylate ligands (OAs) bind to the PNC surface in neutral or deprotonated forms but exhibit relatively low binding energies, making them susceptible to desorption or displacement by halide anions.[322] Consequently, ligand exchange often results in a halide-rich surface terminated by ammonium cations and halide anions. While this surface reconstruction facilitates high EQEs, it does not suppress the deleterious halide ion migration. This leads to short operational lifetimes of a few hours, even compared to PNCs passivated with pristine oleic acid.[319]

Therefore, to simultaneously achieve high efficiency and long-term stability, the perovskite surface must not be terminated exclusively with halide anions. Instead, it is necessary to implement comprehensive passivation strategies using cationic, anionic, or neutral ligands that provide a robust surface binding. High conductivity to facilitate efficient charge injection and transport is also considered. Developing ligand systems that balance these competing requirements is a critical objective for the advancement of colloidal PNC-based optoelectronic devices.

6.2.1. Acidic Counterpart Ligand Engineering. Rather than simply replacing deprotonated OA with halide anions, a more effective strategy involves the introduction of strongly binding acidic ligands. Unlike halide-rich surfaces that remain vulnerable to ion migration, these robust organic anchors firmly passivate the surface and suppress the lattice instability. This approach maintains high efficiency and extends the operational lifetime by providing a durable surface structure. Structural engineering of the side chains of these acidic ligands further allows for improved charge transport properties (Figure 13b).

Replacing OA, which contains a long C18 alkyl chain, with shorter aliphatic carboxylates allows for better surface access and higher binding energy, which suppresses the ligand desorption. The use of OTAc in room-temperature synthesis as a Cs precursor effectively replaces OA and promotes efficient charge transport.[205] In parallel, the incorporation of trifluoroacetate (TFA) utilizes the strong binding affinity of the $-CF_3$ group to surface Pb atoms.[324] This modification significantly enhances both PLQY and carrier mobility through superior surface passivation and shorter side-chain groups.

Beyond carboxylate engineering, benzenesulfonate derivatives have been widely adopted because of their stronger affinity for surface Pb atoms. For instance, dodecylbenzenesulfonic acid (DBSA) exhibits a calculated binding energy of 1.64 eV, which significantly surpasses the 1.47 eV of ammonium bromide.[325] Although DBSA retains a long alkyl chain that limits mobility, the superior passivation of surface halide vacancies can upshift the band structure to improve charge matching.[325,326] To address the transport limitations of long alkyl chains, DBSA can be substituted with shorter molecules such as 4-methylbenzenesulfonate.[327] Moreover, replacing the benzene ring with a naphthalene moiety, such as 2-naphthalenesulfonic acid, increases the current density by 3 orders of magnitude.[328] This strategy extends to bifunctional ligands, such as 1,5-naphthalenedisulfonic acid. This ligand enhances mobility and induces a parallel PNC orientation relative to the substrate, which increases the horizontal transition dipole moment ratio from 60% to 70%.[329]

Phosphonate-type ligands provide binding energies superior to those of carboxylates and amines.[330,331] For instance, PNCs synthesized with single phosphonic acid ligands exhibit exceptional PLQY stability even upon dilution, which confirms the robust anchoring capability of the phosphonate group.[332] While shorter aromatic side chain structures such as phenylphosphonic acid[333] or benzylphosphonic acid (BPA)[334] are utilized, they often require OA as a coligand to maintain colloidal stability. In contrast, DOPA is a promising alternative ligand that can fully replace OA without a loss of colloidal stability. DOPA is characterized by two shorter branched alkyl chains and a high adsorption energy of 1.9 eV, compared with 1.5 eV for OA.[335−337] By utilizing the strong binding of DOPA, surface reconstruction strategies were introduced for $CsPbI_3$ PNCs. This approach increases the activation energy for defect formation and allows for a rigorous surface etching. This process reconstructs imperfect octahedra and supplies oleylammonium iodide, whereas conventional OA-based PNCs would degrade under such conditions.[336] To further optimize performance, methyltributylphosphonium iodide is employed as a coligand. This quaternary salt complements the anionic binding of DOPA while improving the conductivity through reduced steric hindrance. Consequently, this dual-ligand system enables the realization of PeLEDs with both a high efficiency and enhanced stability.[336]

6.2.2. Multifunctional Additives. While the preceding section focused on acidic ligands that substituted anionic oleates, complementary surface passivation can be realized through chemically interactive additives. Distinct from primary ligands that rely on insulating long alkyl chains for colloidal stability, these additives are designed to maximize the passivation efficacy via compact molecular structures. This approach facilitates the simultaneous enhancement of the efficiency, stability, and charge transport. For this purpose, functional strategies utilizing hydrogen bonding[23,338,339] and multidentate chelation[340−342] have been employed. These moieties coordinate to the surface through lone pair donation

Downloaded from pubs.acs.org/chreav/article-pdf/doi/10.1021/acs.chemrev.6c00202/68805793/acs.chemrev.6c00202.pdf by guest on 10 October 2026

https://doi.org/10.1021/acs.chemrev.6c00202
Chem. Rev. XXXX, XXX, XXX−XXX

Table 4. Summary of Perovskite Nanocrystal Light-Emitting Diodes

Composition	EL peak (nm)	Luminance (cd m^{-2})/radiance	EQE (%)	$V_{on}/V_{1,000\ nit}/V_{10,000\ nit}$[a] (V)	Operational lifetime (T_{50})	Ligand/ molecules	Ref.
$CsPb(Br/Cl)_3$	467	~1,000	7.45	3.0/5.7/-	61 min @ 100 cd m^{-2}	CTTS	327
$CsPb(Br/Cl)_3$	490	2,843	23.5	-/3.5/-	43.41 min @ 100 cd m^{-2}	CsTFA	324
$CsPbBr_3$	508	44,452	8.95	2.8/5.0/-		DBSA, OTAc	326
$CsPbBr_3$	510	~10,000	22	2.5/3.7/6.0	60 min @ 1,200 cd m^{-2}	NaBr	318
$CsPbBr_3$	511	2,030	19.30	2.7/4.7/-	50 s @ 1,000 cd m^{-2}	DDAF	320
$CsPbBr_3$	515	330	3	4.0/-/-		DDAB	322
$(Cs/FA)PbBr_3$	515	55,800	11.60	2.7/3.3/4.3		DDAB, OTAc	205
$CsPbBr_3$	518	45,012	18.60	-/3.1/3.7	60 min @ 2,000 cd m^{-2}	DDAB, OTAc	319
$FAPbBr_3$	528	13,950	22.63	2.7/4.5/7.6	38 min @ 100 cd m^{-2}	NDSA	329
$FAPbBr_3$	531	29,280	12.9	3.6/4.9/6.2		BPA	334
$FAPbBr_3$	531	~23,000	23.4	2.7/3.6/4.7	132 min @ 100 cd m^{-2}	GA	23
$FAPbBr_3$	531	~20,000	29.6	2.7/3.6/4.7	4.2 h @ 100 cd m^{-2}	GA	31
$FAPbBr_3$	532	671,115	19.2	3.8/5.0/5.8	20 min @ 100 cd m^{-2}	NSA	328
$CsPbI_3$	630	21,590	21.8	2.5/3.7/5.6	11.7 h @ 100 cd m^{-2}	4-FBSA	339
$CsPb(Br/I)_3$	632	3,840.5	24.5	2.4/4.4/-		PPA	333
$CsPb(Br/I)_3$	635	12,910	22.8	2.21/3.1/4.8	63 min @ 100 cd m^{-2}	Tryptophan	341
$CsPbI_3$	644	4,140	28.5	2.5/4.7/-	30.4 h @ 100 cd m^{-2}	DOPA, TMPI	336
$CsPb(Br/I)_3$	649	500	21.30	2.9/8.0/-	180 min @ 100 cd m^{-2}	OAMI	321
$CsPbI_3$	686	43,691 mW sr^{-1} m^{-2}	26			PZPY	340
$CsPbI_3$	689	2,002	21.2	2.8/5.0/-	25 h @ 50 mA cm^{-2}	O-Tg	338
$CsPbI_3$	693	119,037 mW sr^{-1} m^{-2}	27			TMeOPPO-*p*	342

[a]Turn-on voltage (V_{on}) and driving voltages at 1,000 and 10,000 cd m^{-2} ($V_{1,000\ nit}$ and $V_{10,000\ nit}$) were extracted by digitization from the *J*−*V*−*L* curves of the corresponding references. CTTS (cetrimonium tosylate); CsTFA (cesium trifluoroacetate); DBSA (dodecylbenzenesulfonic acid); OTAc (octanoic acid); NaBr (sodium bromide); DDAF (didodecyldimethylammonium fluoride); DDAB (didodecyldimethylammonium bromide); NDSA (1,5-naphthalenedisulfonic acid); BPA (benzylphosphonic acid); GA (guanidine); NSA (2-naphthalenesulfonic acid); 4-FBSA (4-fluorobenzenesulfonamide) ; PPA (phenylphosphonic acid); DOPA (diisooctylphosphinic acid); TMPI (methyltributylphosphonium iodide); OAMI (oleylammonium iodide); PZPY (2-(1H-pyrazol-1-yl)pyridine); O-Tg (1-(o-tolyl)biguanide); TMeOPPO-p (tris(4-methoxyphenyl)-phosphine oxide)

or chelation, effectively passivating surface defects and strengthening the structural stability of ionic lattices (Figure 13c).

Guanidine represents a standard example of molecular additives capable of enhancing the perovskite stability. By adding 10% guanidine bromide into the precursor during synthesis, these cations were partially incorporated into the lattice to stabilize the crystal structure. The remaining molecules are located at the surface, forming strong hydrogen bonds with the PNC surface sites.[23,31] Building on this concept, o-tolylbiguanide, which contains repeated guanidino moieties, functions as a multidentate hydrogen-bonding agent.[338] Its structure facilitates robust interaction with surface halide anions, resulting in significantly increased binding energy. The steric hindrance arising from this multidentate binding suppresses the formation of the Cs vacancy defects. This mechanism mitigates ion migration and prolongs the operational lifetime of the device.[338] Furthermore, in 4-fluorobenzenesulfonamide, the sulfonamide and fluoro groups prevent protonation of the amine group and create an electron-deficient state. Consequently, the electropositive amine group can form hydrogen bonds with electronegative surface halide anions. Additionally, the Lewis basic S=O group coordinates with surface Pb ions. This strong binding motif improves both the efficiency and available current density.[339]

The use of multidentate ligands containing two or more binding sites is an effective strategy for surface passivation. Tryptophan is a representative example, featuring an electron-rich indole ring along with carboxyl and amino groups.[341] Its structure allows for strong coordination with PNCs, resulting in a high adsorption energy of 4.14 eV compared to 1.22 eV for OA and 1.87 eV for OAm. The addition of tryptophan significantly enhances the PLQY and increases the current density by 2 orders of magnitude compared to pristine PNCs.[341]

However, for additives with multiple binding sites, the structural match between the molecule and the perovskite lattice is critical. A geometric mismatch typically induces lattice strain or leads to an inefficient binding. To address these steric issues, 2-(1H-pyrazol-1-yl)pyridine (PZPY) utilizes its molecular flexibility.[340] The molecule adopts a twisted conformation to reduce steric hindrance, which allows for stable bidentate binding between the nitrogen atoms and the surface Pb^{2+} sites. This interaction suppresses Ostwald ripening in solution and improves both the efficiency and conductivity of the PNC films.[340] In addition, functional groups can be attached to triphenylphosphine oxide to achieve multisite binding. In such cases, matching the molecular length to the perovskite lattice parameters is essential to avoiding lattice distortion. For example, the use of tris(4-methoxyphenyl)phosphine oxide (TMeOPPO-p) with a para-methoxy group provides a suitable geometric fit with the lattice.[342] This structural compatibility results in superior efficiency and stability, as well as improved carrier transport properties.

The aforementioned ligand engineering and additive strategies primarily address surface defect passivation while maintaining charge transport at the single-particle level. However, even with optimized ligand compositions, the performance of PeLEDs is frequently limited by the insulating nature of the ligand shell and structural disorder of the film. Consequently, achieving high-performance PNC-based PeLEDs requires extending control from the molecular engineering of individual nanocrystals to the mesoscopic assembly of the film.

https://doi.org/10.1021/acs.chemrev.6c00202
Chem. Rev. XXXX, XXX, XXX−XXX

Downloaded from pubs.acs.org/chreay/article-pdf/doi/10.1021/acs.chemrev.6c00202/68805793/acs.chemrev.6c00202.pdf by guest on 10 October 2026

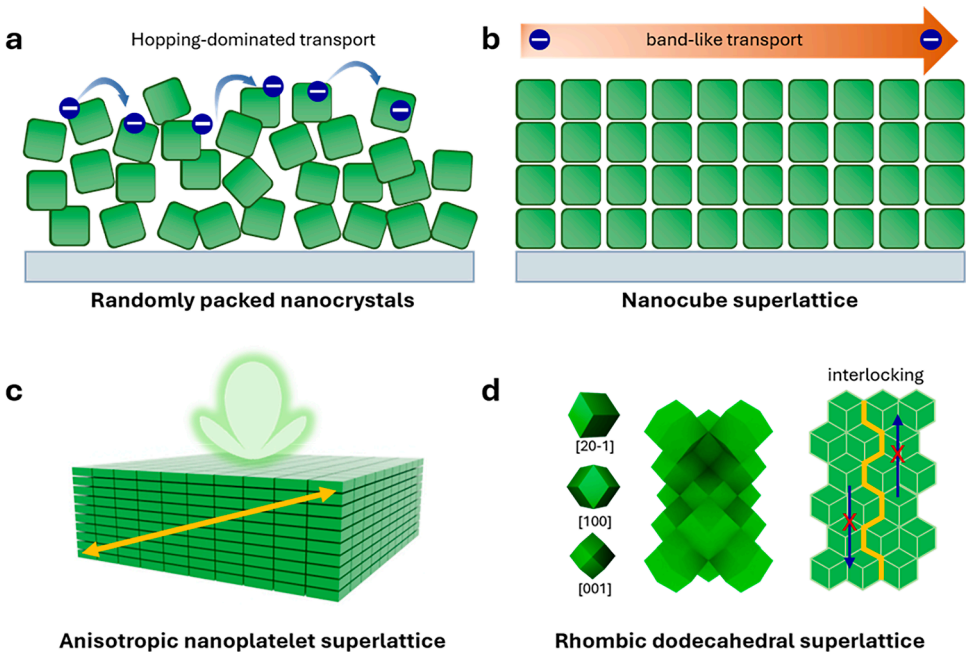


Figure 14. Charge transport mechanisms and structural configurations in perovskite nanocrystal assemblies. (a) A randomly packed nanocrystal film where charge carriers are transported via hopping mechanisms. (b) An ordered nanocube superlattice film. The spatial alignment of the nanocrystals enables transport behavior approaching a band-like regime. (c) Anisotropic nanoplatelet superlattice. The uniform alignment of the horizontal transition dipole moment throughout the film enhances the light outcoupling efficiency. (d) A rhombic dodecahedral superlattice. This interlocked geometry provides a structurally stable assembly that inhibits shear dislocation between the individual nanocrystals.

This approach necessitates a focus on the spatial arrangement of nanocrystals to facilitate efficient charge transport, as discussed below. The performance of the PNC PeLEDs is summarized in Table 4.

6.3. Ordered Assemblies in Perovskite Nanocrystals

To overcome the charge-transport limitations of disordered nanocrystal films, nanocrystal superlattices have emerged as spatially correlated assemblies with long-range translational order. In contrast to randomly packed films, where charge transport proceeds through thermally activated hopping across a structurally and energetically heterogeneous network (Figure 14a), superlattices impose a spatially correlated distribution of interparticle separations. This mesoscale organization establishes structural coherence across the assembly while preserving the quantum-confined electronic states of the individual nanocrystal cores.[343−345]

A central feature of PNC superlattices is the formation of an intermediate electronic-coupling regime. Superlattices increase interparticle electronic interactions without inducing nanocrystal fusion or destroying quantum confinement, thereby increasing carrier mobility and, in some cases, enabling bandlike transport (Figure 14b). Ordered packing reduces energetic disorder, suppresses interfacial trap formation, and alleviates current crowding relative to that of disordered films.[77] As a result, superlattice emissive layers promote more uniform charge redistribution and can sustain high luminance at a reduced operating voltage, which decreases local Joule heating and bias-driven degradation.[288,346,347]

Perovskite nanocrystals are well-suited to superlattice assembly, owing to their well-defined crystallographic symmetry and faceted morphologies. They typically adopt cubic or orthorhombic phases, enabling the synthesis of shape-controlled building blocks, such as nanocubes,[348,349] nanoplatelets,[350] and rhombic dodecahedra.[351] The presence of defined facets promotes dense and directional packing during self-assembly, which enables ordered emissive layers with tunable electronic couplings and collective optical responses.

6.3.1. Nanocube Superlattices. Perovskite nanocubes are the most widely studied building blocks for superlattice assemblies (Figure 14b).[352−354] Their near-isotropic shape and well-defined crystallographic facets support dense packing and facilitate the formation of both translational and orientational orders during self-assembly. Nanocube assemblies, therefore, provide a reproducible platform for tuning the interparticle spacing through ligand chemistry while maintaining structural coherence across the emissive layer.

The optoelectronic advantages of nanocube superlattices became evident in studies of monodisperse $CsPbBr_3$ nanocubes that spontaneously assembled into electronically coupled superlattices. Nanocubes that emitted at 510−515 nm assembled into superlattices that showed a red-shifted yet spectrally narrow green emission at approximately 530−535 nm.[354] The PLQY of the assembled films remained high at about 45%, which slightly exceeded that of films of isolated nanocubes at about 40% and was far higher than that of bulk $CsPbBr_3$ films below 0.1%. These results indicated that periodic ordering can preserve excitonic confinement while maintaining an efficient radiative recombination.[354]

Subsequent studies translated these concepts into electrically driven PeLED architectures. In one example, mixed-halide red-emitting $CsPb(Br/I)_3$ nanocubes were processed using a dual-ligand treatment using aniline hydroiodide and bromotrimethylsilane, which narrowed the size distribution, reduced the density of electronically insulating surface ligands, and promoted compact long-range ordering.[291] Although these films were not explicitly described as superlattices, they displayed increased periodicity and a narrower distribution of interparticle spacing consistent with partially ordered super-

https://doi.org/10.1021/acs.chemrev.6c00202
Chem. Rev. XXXX, XXX, XXX−XXX

Downloaded from pubs.acs.org/chreav/article-pdf/doi/10.1021/acs.chemrev.6c00202/6880579/acs.chemrev.6c00202.pdf by guest on 10 October 2026

lattice architectures. The resulting ordered nanocube films showed increased conductivity of about 4×10^{-4} S m^{-1} and enabled highly efficient and stable red PNC LEDs, with operating voltages of about 2.8 V at 1,000 nit and external quantum efficiencies above 24%.[291] The operational lifetime increased by nearly 2 orders of magnitude relative to earlier high-efficiency red PNC LEDs.[291] These improvements were obtained without extensive nanocrystal fusion or band-like transport, which indicates that mesoscale order, rather than maximal electronic coupling, can simultaneously improve efficiency, luminance, and operational stability.

6.3.2. Anisotropic Nanoplatelet Superlattices. Nanocube-based superlattices primarily improve charge transport and current redistribution characteristics in PNC LEDs. In contrast, anisotropic building blocks, particularly nanoplatelets, further enable superlattices to function as optically engineered emissive media (Figure 14c).[355−357] Shape anisotropy intrinsically generates transition-dipole anisotropy at the single-particle level. When nanoplatelets assemble into ordered films with orientational alignment, this dipolar anisotropy can propagate from individual nanoplatelets to the mesoscale assembly. The resulting assemblies enable collective optical responses that are inaccessible to isotropic nanocrystal solids.

One representative study used colloidal $CsPbBr_3$ nanoplatelets assembled into orientationally ordered superlattice thin films.[356] Directed self-assembly redistributed the orientations of horizontal and vertical transition dipoles and increased the fraction of horizontally oriented emissive dipoles to about 0.75, compared with about 0.67 in isotropic PNC solids. Optical modeling indicated that this redistribution could enhance the light outcoupling by more than 30%. LEDs that employed these emissive layers reached a peak external quantum efficiency of 24.96%.[356] The enhanced efficiency was attributed to shape-derived dipole anisotropy amplified by superlattice-scale orientation ordering.

Anisotropic nanoplatelet superlattices can also support polarized electroluminescence. In one study, $CsPbI_3$ nanoplatelet superlattices exhibited macroscopically polarized electroluminescence under electrical excitation. The polarization was attributed to coherent nanoplatelet stacking and in-plane symmetry breaking within the ordered assembly.[357] The observation of polarization under electrical bias indicates that superlattice-induced optical anisotropy remains preserved during charge injection and radiative recombination.[357]

These results indicate that anisotropic superlattices provide optical control but their electronic advantages remain less developed. Direction-dependent transport and sensitivity to stacking-induced disorder can limit performance at a high current density. Anisotropic superlattices therefore represent functionally complementary architectures to nanocube-based superlattices when optical regulation is the primary design objective.

6.3.3. Rhombic Dodecahedral (RD) Superlattices. A major limitation of superlattice-based PeLEDs is the mechanical fragility of long-range ordering during processing and device integration. During deposition, patterning, transfer, and multilayer stacking, nanocrystal lattices experience shear stresses and stress gradients that can cause interlayer slip, loss of registry, and fragmentation of ordered domains. Such responses have been reported for nanocube and nanoplatelet superlattices.[355,358] Although ligand chemistry can tune lattice cohesion and stiffness, the noninterlocking packing geometry of these assemblies still leaves them susceptible to shear-driven structural reorganization.[359,360]

Rhombic dodecahedral (RD) nanocrystals introduce a fundamentally different structural motif (Figure 14d). Their polyhedral geometry can form mechanically interlocked hexagonal close-packed (hcp) motifs, where multiple facet contacts restrict translational and rotational motions.[351] This geometric constraint increases resistance to shear-induced loss of registry under a mechanical perturbation. As such, RD superlattices provide a structural platform for stabilizing mesoscale order beyond that achievable in conventional nanocube or nanoplatelet superlattices.

Recent advances have overcome the long-standing barrier to integrating RD superlattices into electrically driven LEDs.[361] In pixelated PNC superlattice LEDs, ligand-fluoride costabilization enables the formation of shape-defined RD nanocrystals with enhanced surface binding energies (up to −3.59 eV) and suppressed ligand desorption, allowing the assembly of micrometer-scale, long-range ordered superlattice thin films with controlled thickness (∼25 nm). These superlattices exhibited markedly reduced energetic disorder and enhanced interparticle electronic coupling, leading to transport behavior approaching a band-like regime, as evidenced by temperature-dependent mobility crossover characteristics. Importantly, the enhanced structural coherence does not diminish radiative recombination efficiency; instead, the PLQY increases from 68.8% in spin-coated disordered controls to 82.3%. When integrated into LEDs, these superlattice architectures deliver a peak EQE of 30.9%, maximum luminance exceeding 1.1×10^5 cd m^{-2}, and a reduced turn-on voltage (∼2.2 V). Notably, these superlattice LEDs showed an extrapolated operational lifetime (T_{50}) of over 12,000 h at 100 cd m^{-2}, representing more than a 2-fold improvement compared to LEDs based on spin-coated disordered films.

These results demonstrate that superlattice ordering is not intrinsically incompatible with high luminescence efficiency; rather, it depends critically on achieving a balance between the interparticle electronic coupling and exciton confinement. In RD superlattices, this balance is enabled by the synergistic combination of geometric interlocking, strong surface passivation, and reduced energetic disorder, which collectively suppresses nonradiative recombination while facilitating efficient charge transport. This establishes RD superlattices as a viable platform for simultaneously optimizing the carrier transport, radiative efficiency, and operational stability in PeLEDs.

6.4. Challenges toward Superlattice PeLEDs

PNC superlattices provide a structural approach to mitigate the confinement-transport trade-off by introducing mesoscale order and a narrow distribution of interparticle spacing while preserving the nanocrystal integrity. However, realizing superlattice-enabled PeLEDs requires simultaneous control of assembly kinetics, ligand dynamics, and interparticle electronic coupling under device-relevant conditions. Implementation in devices requires progress in two coupled areas. First, assembly methods must produce laterally extended, long-range-ordered thin films. Second, ligand chemistry must stabilize an intermediate electronic coupling regime that improves transport without inducing nanocrystal fusion or a loss of confinement. These two challenges are intrinsically interconnected because superlattice ordering emerges under nonequilibrium assembly

Downloaded from pubs.acs.org/chreav/article-pdf/doi/10.1021/acs.chemrev.6c00202/6880579/acs.chemrev.6c00202.pdf by guest on 10 October 2026

https://doi.org/10.1021/acs.chemrev.6c00202
Chem. Rev. XXXX, XXX, XXX−XXX

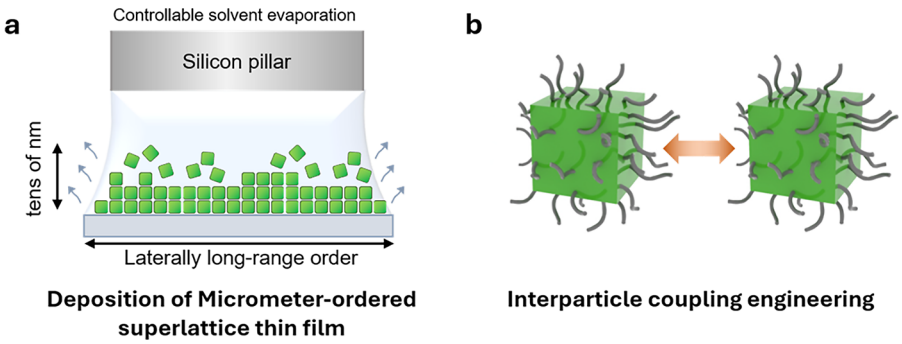


Figure 15. Key requirements for integrating PNC superlattices into LEDs. (a) Controlled solvent evaporation to form laterally long-range ordered thin films. (b) Interparticle coupling engineering by optimizing ligand chemistry to balance structural integrity and charge transport.

conditions, in which ligand binding, interparticle spacing, and electronic coupling continuously evolve during film formation.

6.4.1. Confined Assembly of Long-Range Ordered Superlattice Thin Films. Most superlattice-inspired PNC LED studies fabricate emissive layers by spin-coating.[291,354,356,357] Strategies including ligand engineering,[291] surface modification of charge transport layers,[356] and tuning of solvent evaporation kinetics[357] have been explored to increase local packing order in these rapidly deposited films. These approaches can increase film compactness and improve short-range ordering, but the spin-coating process typically completes within seconds and limits the nanocrystal diffusion and rotational rearrangement. The assembly becomes kinetically trapped and does not approach thermodynamic equilibrium, which restricts the development of a long-range periodicity. In many spin-coated PNC films, direct evidence of micrometer-scale order on the substrate remains limited. Electron microscopy and grazing-incidence X-ray scattering often indicate locally ordered domains within a largely disordered matrix with lateral correlation lengths shorter than those obtained by slow evaporation or bulk assembly.[291,362] As a result, collective optoelectronic effects that require coherent coupling across multiple nanocrystals, including superfluorescence and transport approaching bandlike behavior, are typically absent or strongly reduced. Local ordering can still improve charge transport uniformity and device stability, but it should be carefully distinguished from long-range ordered superlattices formed under near-equilibrium conditions. Demonstration of long-range order in confined superlattice thin films also requires a rigorous characterization. On-substrate scanning electron microscopy (SEM) and grazing-incidence small-angle X-ray scattering (GISAXS) are needed to quantify the lateral correlation length and lattice registry across the film. Optical and electrical signatures, such as superfluorescence or transport approaching bandlike behavior, can provide additional evidence for collective coupling. Without such corroboration, reports of superlattice formation in device-scale thin films should be interpreted with caution.

Long-range-ordered superlattice thin films require assembly methods that slow solvent removal and confine deposition to provide time for translational and orientational ordering. However, most long-range ordered PNC superlattices rely on assembly routes that yield micrometer-thick or free-standing assemblies rather than continuous substrate-supported films.[352,354,359,360] Recent confined assembly strategies have begun to address this limitation.[361] For example, capillary liquid-bridge-mediated assembly enables micrometer-scale in-plane ordering and ultrathin (10−50 nm) superlattice films (Figure 15a), thereby bridging the long-standing gap between structural coherence and device integration. Such approaches demonstrate that superlattice ordering can be preserved during pixelation and multilayer device fabrication.

However, challenges remain in extending these strategies to large-area manufacturing, high-throughput processing, and full-color-display integration. In particular, maintaining uniformity and registry across wafer-scale substrates as well as ensuring compatibility with industrial fabrication workflows are critical for practical applications. These challenges become even more severe in full-color superlattice displays, where mixed halide compositions introduce phase segregation and increased energetic disorder that can disrupt superlattice coherence and accelerate operational degradation. As a result, achieving stable long-range ordering in blue- or red-emitting superlattices requires substantially stronger surface stabilization and more robust interfacial control than those of monochromatic bromide systems.

6.4.2. Interparticle Coupling Engineering via Ligand Chemistry. Confined assembly of long-range ordered PNC superlattice thin films places stringent constraints on ligand chemistry (Figure 15b). Assembly typically occurs at high nanocrystal concentrations, often tens of mg mL^{-1}, while continuous solvent removal progressively decreases interparticle spacing during deposition. Under these conditions, stable ligand binding and sustained surface passivation determine whether ordered superlattice packing can emerge without structural degradation. Conventional PNCs capped with dynamically bound OA are particularly vulnerable during concentration-driven assembly.[300] These ligands bind weakly and can desorb as solvent is removed, which generates undercoordinated surface sites that promote nanocrystal fusion, defect formation, and chemical degradation and disrupt superlattice order.[361] Stronger binding ligands, including headgroups with higher coordination strength and multidentate motifs, can stabilize individual nanocrystals and preserve long-range order by maintaining passivation during confined assembly.[359] Cross-linking strategies can further stabilize interparticle spacing and suppress ligand migration,[363] but they can introduce additional transport barriers if the resulting network is electronically insulating or spatially nonuniform. In many cases, stabilization is accompanied by thicker or more insulating ligand shells, which can impede charge injection and interparticle charge redistribution in LEDs.

For superlattice-based PeLEDs, the objective is not merely to maximize interparticle electronic coupling but to stabilize an intermediate coupling regime that balances charge redistribution with exciton confinement. In this regime, coupling

Downloaded from pubs.acs.org/chreay/article-pdf/doi/10.1021/acs.chemrev.6c00202/68805793/acs.chemrev.6c00202.pdf by guest on 10 October 2026

https://doi.org/10.1021/acs.chemrev.6c00202
Chem. Rev. XXXX, XXX, XXX−XXX

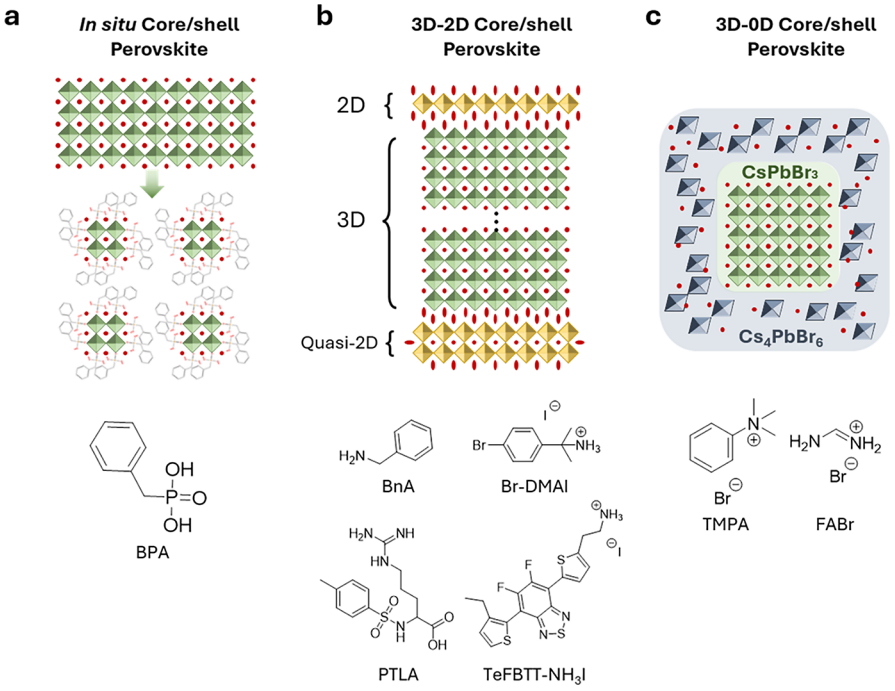


Figure 16. Schematic illustration of core/shell and heterostructure perovskites. (a) *in situ* core/shell nanocrystalline perovskites, (b) 3D-2D/quasi-2D core/shell perovskites, and (c) 3D-0D core/shell perovskites (e.g., $CsPbBr_3/Cs_4PbBr_6$). Representative ligands/additives for each strategy are shown below each panel.

facilitates charge redistribution, while robust binding and effective passivation prevent nanocrystal fusion and nonradiative losses. Defining and maintaining this optimal coupling window under continuous electrical bias remain significant challenges, as ligand rearrangement and ion migration can alter interparticle barriers during operation. Ultimately, preserving both structural order and electronic connectivity requires ligand engineering to precisely regulate the coordination strength, ligand packing density, and interparticle barrier thickness, thereby ensuring persistent binding, superior surface passivation, and minimized interparticle barrier thickness. Future superlattice PeLEDs will therefore require the simultaneous coengineering of assembly kinetics, ligand dynamics, and interparticle electronic coupling under operational conditions.

7. CORE/SHELL PEROVSKITES FOR BALANCING CHARGE CONFINEMENT AND TRANSPORT

Achieving high charge transport while maintaining carrier confinement and effective defect passivation has been a central objective in the development of PeLEDs. Core/shell architectures have attracted attention because they can preserve charge transport while strengthening confinement and passivation, directly addressing the central trade-off discussed in this review.[25] Recent studies on perovskite emitters have shown that hierarchical core/shell nanocrystals can substantially improve device performance metrics, with T_{90} values of approximately 12,000 h under 180 W m^{-2} blue-light exposure and 3,211 h under accelerated aging at 60 °C and 90% relative humidity.[349] These improvements were attributed to the core/shell structure-driven lattice stabilization and surface-chemistry control, which suppressed ion migration and redox reactions. Accordingly, core/shell perovskite architectures would represent a promising strategy for simultaneously achieving strong confinement and efficient charge transport.[364] However, because hierarchical designs employ insulating shell materials, their direct use as emissive layers in PeLEDs can impose transport limitations.[1] Alternative core/shell architectures that preserve charge transport are therefore of particular interest. In the following section, three classes of core/shell perovskite structures are discussed as candidates for simultaneously achieving strong confinement, effective passivation, and efficient charge transport.

7.1. *In Situ* Core/Shell Perovskite

One representative approach employed an *in situ* core/shell structure in nanoscale-polycrystalline perovskite films through a post-treatment (Figure 16a) using a weakly polar solvent, THF, in the presence of BPA.[22] Time-dependent TEM indicated a progressive reduction in the characteristic crystallite size from approximately 200 nm to about 10 nm, which was attributed to repeated BPA adsorption and fragmentation of perovskite domains.[22] This morphological evolution coincided with an increase in exciton binding energy from 90 to 220 meV, which is consistent with stronger confinement after nanocrystal formation.[22] BPA was proposed to bind defective surface sites through Pb−O−P covalent bonding and to form an organic shell.[22] Despite the introduction of an organic shell, charge transport was largely maintained, with a reported hole mobility of 2.99×10^{-2} cm^2 V^{-1} s^{-1}, which is comparable to that of the nanoscale-polycrystalline perovskite film (3.26×10^{-2} cm^2 V^{-1} s^{-1}).[22] This example indicates that *in situ* core/shell formation can strengthen confinement while limiting transport loss in polycrystalline films, and reports an operational lifetime of 31,808 h.[22]

7.2. 3D/2D Perovskite Heterostructure

Perovskite/perovskite heterostructures provide an emitter architecture in which recombination is confined to high-radiative-efficiency perovskite domains, while a low-dimensional (2D or quasi-2D) overlayer passivates surface defects without interrupting carrier transport (Figure 16b).[365] Because the 2D

https://doi.org/10.1021/acs.chemrev.6c00202
Chem. Rev. XXXX, XXX, XXX−XXX

Downloaded from pubs.acs.org/chreav/article-pdf/doi/10.1021/acs.chemrev.6c00202/68805793/acs.chemrev.6c00202.pdf by guest on 10 October 2026

phase typically has a wider band gap, 3D/2D stacks often form type-I band alignment[366] that confines carriers and excitons within the 3D region and shifts the recombination zone away from defect-rich interfaces.[367] The 2D component further acts as an energetic barrier that suppresses carrier leakage and associated efficiency roll-off at high current density while reducing interfacial quenching and ion-migration-related degradation.

An early stage 3D/2D hybrid perovskite was obtained by introducing benzylamine (BnA) into the precursor.[368] BnA was protonated by methylammonium and promoted the formation of n = 1, 2 phases.[368] The 2D component was preferentially distributed along grain boundaries and formed an effective barrier between adjacent 3D grains.[368] This grain boundary 2D barrier suppressed ion migration, reduced $J-V$ hysteresis and the initial luminance overshoot during operational lifetime testing, and increased the LED operational lifetime (T_{40}) by more than 21-fold.[368] These results indicate that 3D/2D perovskite heterostructures can improve the device performance under sustained electrical bias.

Related efforts also done by employing heteroepitaxy between $CsPbI_3$ quantum dots and a quasi-2D perovskite matrix, and controlled interfacial alignment/tilting at the QD matrix boundary.[369] A synthesis-on-substrate (SOS) process[94] was employed to synthesize, in a one-step solution route directly on the substrate, PNCs encapsulated by a surrounding quasi-2D phase.[369] A precursor containing both α,α-dimethyl-4-bromobenzylammonium (Br-DMA$^+$) and Br-PEA$^+$ was used, which enabled the concurrent formation of PNCs and quasi-2D perovskite on the substrate.[369] After antisolvent dripping, the PNCs and quasi-2D domains crystallized concurrently, and the strong dipole−dipole interactions between the ligands promoted an edge-on stacked configuration during crystallization.[369] The resulting edge-oriented ligands, together with the reduced interphase spacing between heterophases, produced a robust heteroepitaxial interphase and formed a de-epitaxy composite architecture.[369] This structural design improved the phase stability of the QDs through octahedral tilting during heteroepitaxial formation, while combining the enhanced charge-transport characteristics of the quasi-2D component (relative to a purely 2D phase) with the effective confinement of the QDs.[369] Consequently, the PeLEDs achieved a maximum EQE of 24.6% and a T_{50} of 6,300 min at 100 cd m^{-2}, demonstrating that concurrent high efficiency and effective charge transport can be achieved in a heteroepitaxial architecture.[369]

In a related approach, strongly coordinating additives were used to create an intragrain heterophase barrier. A strongly coordinating additive, p-toluenesulfonyl-L-arginine (PTLA), was found to segregate within perovskite grains and promote the formation of a lattice-expanded perovskite phase.[26] The resulting 3D/quasi-2D intragrain embedded structure introduced an internal barrier phase that suppressed electron and hole leakage.[26] At the same time, the carboxyl and amine groups of PTLA formed strong interactions with the Pb-X framework, which maintained structural connectivity with the 3D phase.[26] In an alternative approach, the 2D phase was formed separately after deposition of the 3D perovskite film by post-treating the film with a functional organic ligand, 2-(5-(7-(3-ethylthiophen-2-yl)-5,6-difluorobenzo[c][1,2,5]thiadiazol-4-yl)thiophen-2-yl)ethan-1-aminium iodide (TeFBTT) dissolved in an IPA/chlorobenzene mixture.[33] Post-treatment of the preformed $FAPbI_3$ film with the organic spacer TeFBTT induces spontaneous formation of a surface-capped 2D/3D heterostructure, in which a layered 2D perovskite phase conformally envelopes the underlying 3D grains.[33] The terminal -NH_3^+ group anchors TeFBTT at the perovskite surface through coordination/ionic interactions with the surface Pb−I framework, thereby promoting the assembly of a layered heterophase at the grain interface.[33] Notably, TeFBTT was molecularly engineered with band alignment in mind: fluorination of the benzothiadiazole unit shifts the frontier orbital levels to deeper energies, thereby improving energetic alignment with the inorganic $[PbI_4]^{2-}$ sublattice and favoring a Type-I interfacial alignment.[33] This design reduces the effective interfacial barrier and facilitates efficient funneling of carriers and/or excitations into the emissive 3D perovskite.[33] In parallel, the spacer-assisted interfacial reconstruction provides effective passivation of shallow trap states, increasing the radiative recombination probability.[33] As a result of the combined improvements in carrier transport and radiative recombination, the devices achieved a high radiance of 929 W sr^{-1} m^{-2} and a maximum EQE of 31.4%.[33]

7.3. Core/Shell Perovskite with Cs_4PbBr_6 Phase

Cs_4PbBr_6 is a secondary phase in the Cs−Pb−Br system and adopts a 0D structure with spatially isolated $PbBr_6$ octahedra, which is typically associated with poor charge transport. When its fraction is controlled, Cs_4PbBr_6 can be incorporated into 3D/0D heterophase nanocrystals in which $CsPbBr_3$ forms the emissive domain, and Cs_4PbBr_6 forms a surrounding phase (Figure 16c). Several reports suggest that $CsPbBr_3$ and Cs_4PbBr_6 can show favorable interfacial matching with an endotaxial relationship,[370] which can reduce mismatch strain and decrease the density of interface-related defects. In addition, Cs_4PbBr_6 has been reported to suppress ion migration in $CsPbBr_3$-based materials by passivating vacancy-type defects and by interrupting ion transport pathways at interfaces and grain boundaries.[371] In one approach, m-F-PEA accelerated crystallization and promoted early $CsPbBr_3$ formation, whereas trimethylphenylammonium bromide (TMPA) introduced steric constraints that hindered corner sharing of $PbBr_6$ octahedra and, together with Cs-rich local stoichiometry during growth, promoted 0D Cs_4PbBr_6 formation around $CsPbBr_3$ domains.[372] The resulting 3D/0D nanocrystals retained a hole mobility of 2.82×10^{-2} cm^2 V^{-1} s^{-1}. A related route employed partial substitution of the A-site cation with 20% FA$^+$, where preferential crystallization of $FAPbBr_3$ was proposed to generate nuclei for $FA_xCs_{1-x}PbBr_3$ growth and residual CsBr promoted conversion of the $PbBr_6$ network into isolated octahedra, yielding Cs_4PbBr_6 and a reported 3D/0D core/shell morphology with a hole mobility of 7.69×10^{-2} cm^2 V^{-1} s^{-1}.[38] $CsPbBr_3$/Cs_4PbBr_6 core/shell structures have also been prepared by thermal evaporation by adjusting the CsBr to $PbBr_2$ ratio during deposition.

8. THERMALLY EVAPORATED PEROVSKITES FOR LEDS

Thermally evaporated perovskites have emerged as an attractive platform for PeLEDs, particularly in the context of commercial manufacturing. Unlike solution processing, vacuum deposition is compatible with the established OLED production infrastructure, including thermal evaporation systems, shadow mask patterning, and multilayer device fabrication. This compatibility makes thermally evaporated PeLEDs promising for reproducible, large-area, and high-resolution devices, where process

Downloaded from pubs.acs.org/chreav/article-pdf/doi/10.1021/acs.chemrev.6c00202/68805793/acs.chemrev.6c00202.pdf by guest on 10 October 2026

https://doi.org/10.1021/acs.chemrev.6c00202
Chem. Rev. XXXX, XXX, XXX−XXX

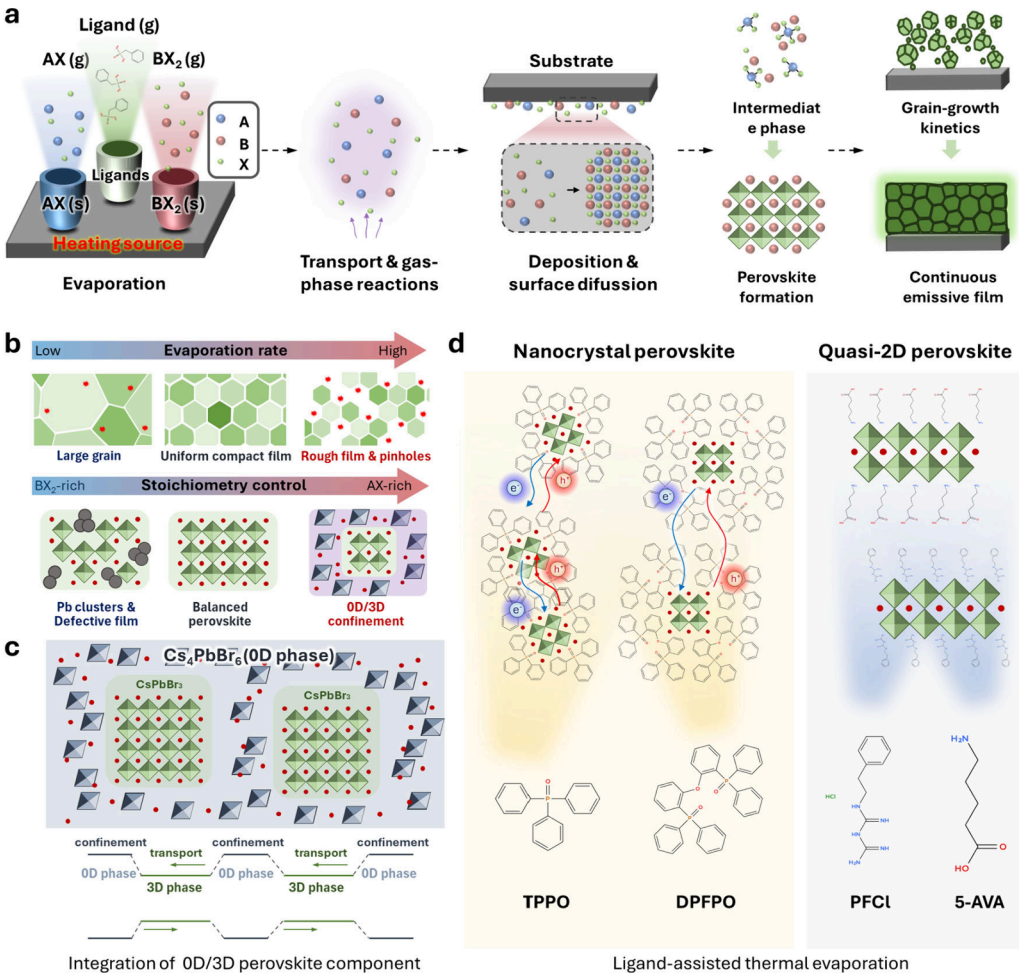


Figure 17. Strategies for regulating exciton confinement and charge transport in thermally evaporated perovskites. (a) Schematic illustration of *in situ* crystallization during perovskite thermal evaporation. (b) Control of evaporation rate and precursor stoichiometry as fundamental parameters for regulating perovskite growth. (c) Exciton-confined core/shell heterostructures. (d) Ligand-assisted nanocrystal and quasi-2D perovskite structures for enhanced exciton confinement and charge transport.

uniformity and integration with existing display technologies are critical.[373]

However, thermally evaporated PeLEDs should not be regarded simply as vacuum-processed counterparts of solution-processed devices. The absence of solvent-mediated film formation gives rise to distinct crystallization behavior, emissive layer microstructures, and device integration strategies. These differences are particularly important for balancing the exciton confinement with efficient charge transport. Accordingly, the following discussion focuses on how vapor-phase crystallization governs confined emission and perovskite-internal charge transport and how vacuum-compatible device architectures can further support charge transport and operational stability.

8.1. Crystallization-Mediated Exciton Confinement and Internal Charge Transport

Crystallization control in thermally evaporated perovskites is fundamentally different from that in solution-processed films. In solution processing, nucleation and growth are mediated by solvent coordination, precursor solvation, antisolvent extraction, and post-treatment. In contrast, thermally evaporated perovskites are formed through the arrival, surface diffusion, and reaction of vapor-phase precursors on the substrate (Figure 17a).[374] This vapor-phase growth mode provides direct control over deposition rate, precursor flux, film thickness, and layer sequence, but it can also lead to kinetically driven crystallization, precursor volatility mismatch, stoichiometric deviation, and nonuniform phase formation.[375,376] Furthermore, kinetically driven fast crystallization or incomplete precursor reaction generates halide vacancies, undercoordinated Pb sites, or defective grain boundaries, thereby promoting trap-assisted nonradiative recombination.[9] These defects are also the primary factors that limit charge transport inside thermally evaporated perovskite emissive layers, because trapped carriers cannot move through the perovskite network efficiently and may instead undergo nonradiative recombination before reaching the radiative recombination zone. Therefore, crystallization control in thermally evaporated PeLEDs should be understood not only as a morphology-control strategy but also as a prerequisite for effective radiative recombination and efficient charge transport.

One direct strategy for controlling exciton confinement in vapor-deposited perovskites is to regulate the deposition rate of each precursor. By tuning the precursor flux and evaporation rate, the nucleation density and grain growth kinetics can be adjusted (Figure 17b).[375,376] For LED applications, a moderately high evaporation rate at reduced substrate temperature can kinetically favor dense nucleation and suppress excessive grain growth, yielding smaller emissive domains suitable for exciton confinement.[10] However, an excessively high evaporation rate or

Downloaded from pubs.acs.org/chreav/article-pdf/doi/10.1021/acs.chemrev.6c00202/6880579/acs.chemrev.6c00202.pdf by guest on 10 October 2026

https://doi.org/10.1021/acs.chemrev.6c00202
Chem. Rev. XXXX, XXX, XXX−XXX

an imbalanced precursor flux can lead to local supersaturation and precursor aggregation, resulting in poor film morphology with pinholes.[377] Therefore, the deposition conditions must be carefully balanced to maintain controlled supersaturation, which promotes uniform film formation while increasing the nucleation density and reducing grain size. Smaller grains or nanodomains can spatially confine carriers and increase the probability of radiative recombination. However, excessive grain size reduction can also increase the total grain-boundary area, which may introduce additional trap states if the boundaries are not sufficiently passivated. When the defect density becomes too high, the confined domains no longer function as efficient radiative centers; instead, the increased number of defective grain boundaries simultaneously weakens exciton confinement and interrupts percolated charge transport pathways. Thus, grain-size control must be optimized together with defect suppression rather than simply maximizing the nucleation density or minimizing grain size.

Compositionally controlled 0D/3D heterostructures offer an effective route to preserve nanoscale confinement while mitigating defect-related losses in small-grained emitters. In vapor-deposited Cs−Pb−Br systems, excess AX content can promote such heterostructures, where CsBr, the AX precursor, not only supplies Cs and Br for $CsPbBr_3$ formation but can also induce a Cs-rich Cs_4PbBr_6 secondary phase when its flux is sufficiently high relative to $PbBr_2$ (Figure 17b,c).[8] Unlike colloidal nanocrystal systems, where long-chain organic ligands are typically required to stabilize nanocrystals in solution, vapor deposition can generate confined perovskite domains through inorganic secondary phases or compositionally controlled heterostructures. For example, an emissive 3D perovskite phase can be spatially embedded within or surrounded by a wider band gap 0D secondary phase, producing a core/shell-like confinement effect without relying on conventional long-chain ligands.

However, this ligand-free confinement should also be considered a trade-off. The 0D phase can spatially confine carriers within emissive 3D domains, but it is generally much less conductive than the 3D perovskite framework. If the 0D phase becomes excessive or forms a continuous insulating matrix, it can interrupt charge-transport pathways, increase injection barriers, and limit carrier supply to the emissive 3D regions.[378] In this sense, 0D inorganic phases can play a role similar to that of insulating ligands. They enhance confinement but may impede charge transport when not carefully controlled.

Moreover, the 0D/3D heterostructure alone does not necessarily provide sufficient control over crystallization kinetics or defect formation. Although the wider-band gap 0D phase can localize carriers, nonuniform nucleation, stoichiometric deviation, undercoordinated sites, and defective grain boundaries can remain after vapor-phase growth. Therefore, molecular ligand or additive engineering is often required as a complementary strategy because it can simultaneously regulate crystallization, reduce grain size, passivate defects, and maintain confined emissive domains. The key requirement is to introduce these additives with an optimized ratio so that defect passivation and confinement are improved without creating additional barriers to the vertical charge injection and transport.

Ligand or additive engineering can also be used in thermally evaporated perovskites, but their roles differ from those in solution-processed colloidal nanocrystal films. In solution processing, ligands often serve multiple functions including colloidal stabilization, surface passivation, crystallization control, and film formation. In vacuum deposition, the major role of molecular additives is more focused on moderating the crystallization kinetics and passivating undercoordinated sites. Properly designed ligands or small-molecule additives such as TPPO, bis[2-[(oxo)diphenylphosphino]phenyl] ether (DPEPO), 5-AVA, and phenformin hydrochloride (PFCl) can slow down perovskite crystallization, increase nucleation density, reduce grain size, and promote the formation of quasi-2D phases or nanocrystalline perovskite domains, thereby enhancing spatial exciton confinement (Figure 17d).[378−381] This approach can improve the exciton confinement and photoluminescence efficiency. Nevertheless, similar to an insulating 0D phase, excessive organic additives may disrupt the perovskite network and impede the charge transport. Thus, defect-passivation strategies based on ligands, additives, or 0D secondary phases are intrinsically limited by the amount and electronic properties of the passivating component because too little passivator leaves traps without passivation, whereas too much passivator creates insulating barriers. Therefore, the central design principle is to use molecular additives to control crystallization and passivate defects without forming thick insulating barriers between emissive domains. In this regard, short, conjugated, or charge-transporting ligands or additives are particularly attractive because they can passivate defects while preserving electronic coupling between neighboring perovskite domains.

Alongside stoichiometric control, heterostructure design, and ligand/additive engineering, nucleation-seeding interlayers provide a complementary route to regulate vapor-phase perovskite crystallization beyond conventional flux or rate modulation. In this strategy, a functional seed layer formed at the substrate interface can control precursor adsorption, local supersaturation, and the initial nucleation pathway during vapor phase growth.[381−383] For example, inorganic salts, ultrathin interfacial layers, or organic spacers with specific binding sites can serve as heterogeneous nucleation templates that guide the formation of low-dimensional or compositionally selected perovskite phases.[384−386] By stabilizing preferred nuclei at the early growth stage, such seed layers can suppress random nucleation, mixed-dimensional crystallization, and spatial phase heterogeneity, leading to improved phase purity, dimensional homogeneity, and structural continuity. Therefore, seed-layer-assisted vapor growth offers a kinetically or thermodynamically guided crystallization route to produce confined perovskite emitters with controlled exciton confinement and reduced defect-mediated losses.[381]

8.2. Device Architecture for Efficient Charge Transport and Stable PeLEDs

Beyond crystallization control within the emissive layer, thermally evaporated PeLEDs can provide process flexibility for device architectures that are favorable for both the charge transport and operational stability. Because each functional layer can be deposited sequentially without solvent exposure, vacuum processing avoids dissolution, swelling, or chemical damage to the underlying layers. This solvent-free stacking process enables cleaner and more reproducible interfaces between the perovskite emissive layer and adjacent charge transport layers, which are essential for efficient charge injection, balanced electron−hole transport, and suppression of interfacial nonradiative recombination.

Ultrathin passivation layers, buffer layers, or interfacial dipole layers can be inserted with controlled thicknesses and

Downloaded from pubs.acs.org/chreav/article-pdf/doi/10.1021/acs.chemrev.6c00202/68805793/acs.chemrev.6c00202.pdf by guest on 10 October 2026

https://doi.org/10.1021/acs.chemrev.6c00202
Chem. Rev. XXXX, XXX, XXX−XXX

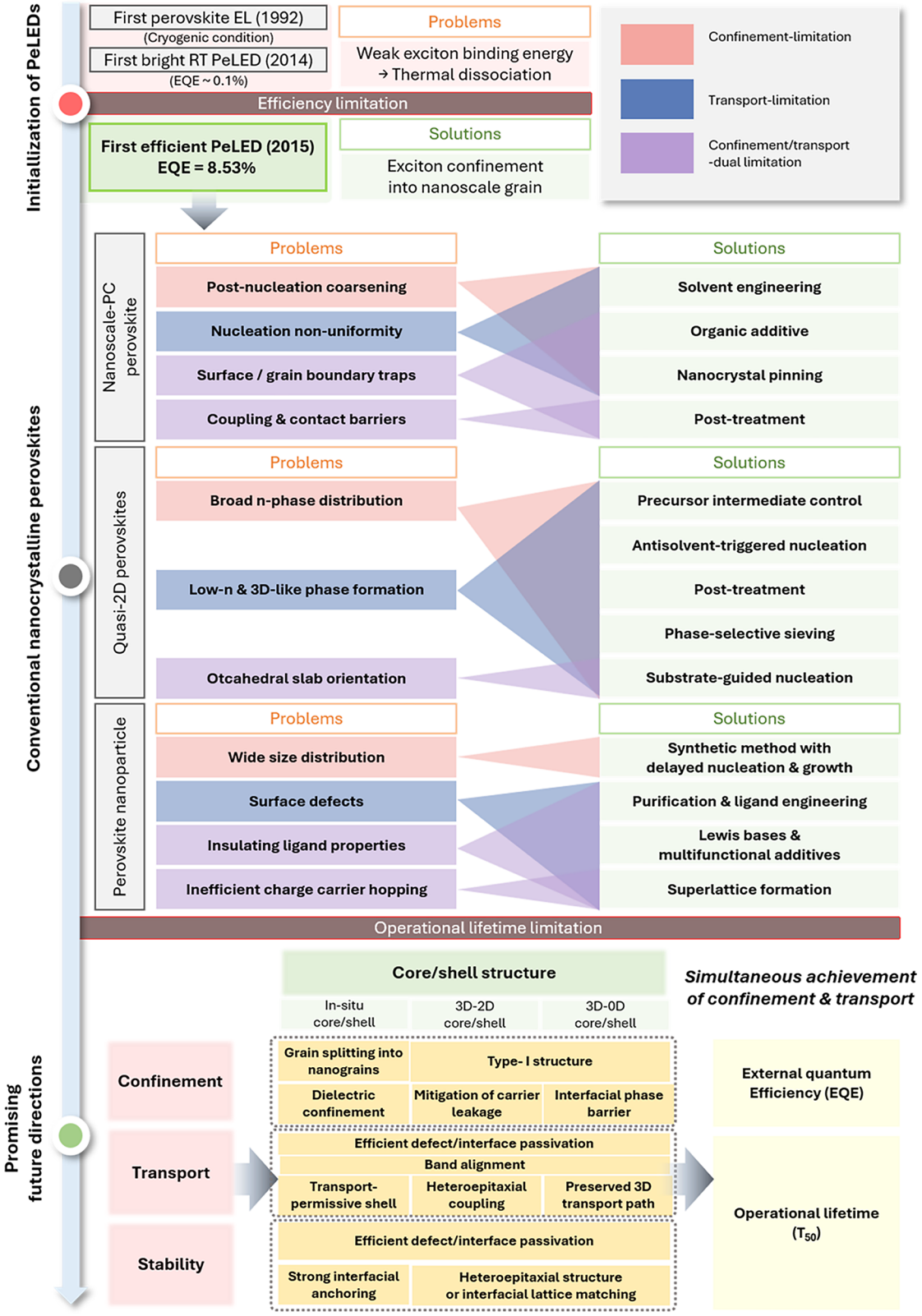


Figure 18. Schematic overview of key confinement- and transport-related bottlenecks limiting PeLED efficiency and operational lifetime, highlighting representative solution strategies and promising directions for nanocrystalline PeLEDs.

compositions to reduce injection barriers, suppress interfacial traps, and improve energy level alignment.[10,383] This is particularly important for confined perovskite emitters, where radiative recombination is enhanced by small grains, low-dimensional phases, or passivated nanodomains but charge injection and vertical transport can be more easily limited. By engineering the interfaces on both sides of the emissive layer, carriers can be supplied more efficiently, while the recombina-

Downloaded from pubs.acs.org/chreav/article-pdf/doi/10.1021/acs.chemrev.6c00202/68805793/acs.chemrev.6c00202.pdf by guest on 10 October 2026

https://doi.org/10.1021/acs.chemrev.6c00202
Chem. Rev. XXXX, XXX, XXX−XXX

tion zone is maintained inside the emissive layer rather than at defective or quenching interfaces. This provides a device-level route to mitigate the transport trade-off introduced by confinement strategies, which are more difficult to implement in solution-processed multilayers because of solvent-orthogonality constraints and interlayer damage.

Vacuum processing also expands the range of candidate charge-transport layers. Since multilayer stacks can be fabricated without solvent orthogonality constraints, regular, inverted, and more complex PeLED architectures can be explored by selecting transport layers with suitable energy levels, carrier mobility, and chemical compatibility.[377,387,388] This flexibility allows the electrical structure of the device to be matched to the transport characteristics of the confined perovskite emitter. In particular, once the perovskite surface is protected by an evaporated buffer or passivation layer, integration with inorganic charge-transport layers (CTLs) becomes more feasible. Compared with many organic transport layers, inorganic CTLs can offer higher carrier mobility, improved electrical conductivity, and better chemical robustness, thereby facilitating charge injection, vertical charge transport, and electron−hole balance in confined PeLED architectures. Thus, vapor-deposited device stacks can provide a more direct and efficient carrier supply pathway to the emissive perovskite domains than many solution-processed architectures.

The ability to integrate inorganic or hybrid transport layers is also relevant to the device lifetime.[389] Inorganic CTLs can provide improved resistance to thermal stress, chemical reactions, and moisture or oxygen ingress compared with many organic counterparts. When combined with evaporated buffer layers or dense interfacial passivation layers, they can suppress interfacial degradation, ion migration-induced reactions, and electrode-induced instability. Moreover, because vapor deposition minimizes exposure of the perovskite layer to moisture and oxygen during fabrication, the initial density of ambient-induced defects or degradation-prone sites can be reduced. This processing environment is beneficial for constructing more robust multilayer stacks that are compatible with encapsulation and long-term operations.

All-vapor-deposited architectures are also advantageous for optical- and display-oriented device design. Precise thickness control enables tuning of optical microcavity effects, emission directionality, and outcoupling efficiency, which are particularly important for top-emitting and high-resolution display structures. At the same time, compatibility with OLED-type evaporation tools and shadow mask patterning provides a practical pathway toward pixelated PeLED fabrication. Therefore, the benefit of vacuum processing is not limited to film formation but extends to the integrated design of charge transport, optical management, and scalable device layout.

Nevertheless, an improved architecture alone does not eliminate all stability issues. Ion migration, interfacial reactions, metal diffusion, Joule-heating-induced structural changes, and defect-assisted degradation can still limit the operational lifetime. Future progress in thermally evaporated PeLEDs will therefore require device designs that simultaneously optimize charge injection, vertical transport, interfacial robustness, and encapsulation-compatible multilayer structures. In this regard, vapor deposition offers a particularly powerful platform because it allows the emissive layer, transport layers, buffer layers, and protective layers to be engineered within a single solvent-free process flow.

9. CONCLUSION AND OUTLOOK

This Review examines material design strategies for overcoming the confinement-transport trade-off in PeLEDs, with an emphasis on the fundamental challenge of maintaining charge confinement and effective defect passivation while preserving charge transport in the perovskite EML (Figure 18). To date, rapid improvements in the EQE have been achieved through nanoscale confinement and surface defect control, while operational lifetimes remain far below commercial targets. In the following, we summarize how each material system addresses the confinement-transport trade-off through material design and how core/shell architectures provide a unified route toward both high efficiency and improved operational lifetime.

For nano-PC perovskites, crystallization kinetics is the primary determinant of film structure. Solvent coordination strength, additive chemistry, and nanocrystal pinning methods can regulate nucleation and growth, suppress grain coarsening, and maintain nanocrystalline films with an enhanced confinement. Because grain size reduction increases the density of surface and grain boundary defects, post-treatment and interfacial reconstruction are required to restore charge transport and reduce trap-assisted nonradiative recombination. Effective strategies must therefore combine the kinetic control of nanocrystal formation with chemically stable passivation and well-defined interfaces.

In quasi-2D perovskites, the central issue is the formation of a narrowed phase distribution that emits efficiently under an electrical bias. Broad *n*-phase distributions arise from precursor aggregation, heterogeneous coordination species, and nonuniform nucleation during spin-coating. Effective quasi-2D processing requires control at several stages, including precursor homogenization to suppress spacer aggregation, nucleation timing control via inhibitor chemistry or antisolvent quenching, and postdeposition processing to prevent redistribution into parasitic low-*n* or high-*n* phases. A major direction for quasi-2D systems involves phase distribution control under practical device processing conditions while simultaneously improving vertical charge transport and suppressing interfacial quenching.

For colloidal PNCs, early progress was based on ligand exchange and surface passivation to improve the PLQY and reduce trap density. However, electrically insulating ligand shells and disordered packing continue to limit the charge transport. Additionally, halide-rich surface conditions often result in unstable operational lifetimes due to ion migration. Consequently, ligand engineering has shifted toward strongly binding acidic ligands and compact multifunctional additives without sacrificing charge mobility. Beyond single-particle passivation, ordered PNC assemblies and superlattice-like structures may reduce the trade-off between confinement and transport by narrowing interparticle spacing distributions and improving the charge redistribution. Two issues remain unresolved for practical PNC superlattice LEDs. The first is the reliable fabrication of laterally extended and long-range-ordered thin films. The second is the development of ligand chemistries that maintain intermediate interparticle coupling under bias without particle fusion, ion migration, or transport blocking.

A promising strategy for mitigating the confinement-transport trade-off is the development of transport-preserving core−shell perovskite structures. Hierarchical and heterophase core/shell designs, including *in situ* core/shell structure, 3D/2D heterostructures, and 3D/0D composite structures such as $CsPbBr_3$/

Downloaded from pubs.acs.org/chreav/article-pdf/doi/10.1021/acs.chemrev.6c00202/6880579/acs.chemrev.6c00202.pdf by guest on 10 October 2026

https://doi.org/10.1021/acs.chemrev.6c00202
Chem. Rev. XXXX, XXX, XXX−XXX

Cs_4PbBr_6, share a fundamental design principle. These architectures rely on the introduction of a chemically and structurally stabilizing shell layer characterized by a controlled thickness, suitable energy-band alignment, and low charge-transport resistance. This structural configuration provides a practical route to preserve efficient charge transport without sacrificing the radiative recombination efficiency. Consequently, transport-preserving core−shell structures enable the simultaneous realization of strong confinement and effective charge transport, which are prerequisites for high-performance PeLEDs. These materials, therefore, serve as highly viable candidates for future development of commercial PeLEDs.

In addition to material design, practical commercialization requires addressing operational stability and durability challenges. Specifically, augmented reality and microdisplay applications demand high-brightness PeLED operation with a minimal efficiency roll-off. These devices also require stable emission under high current densities and robust resistance to both thermal and electrically induced degradation. Achieving these technological targets requires materials and device architectures with broad tolerance to electrical, thermal, and interfacial stress. Ultimately, the successful commercialization of PeLEDs relies on integrated material and device strategies that simultaneously optimize charge confinement, charge transport, and operational stability under high-brightness, high-current-density conditions.

AUTHOR INFORMATION

Corresponding Author

Tae-Woo Lee − *Department of Materials Science and Engineering, Seoul National University, Seoul 08826, Republic of Korea; Research Institute of Advanced Materials (RIAM) and Institute of Engineering Research, Soft Foundry, Interdisciplinary Program in Bioengineering, Seoul National University, Seoul 08826, Republic of Korea; SN Display Co., Ltd., Seoul 08826, Republic of Korea;* orcid.org/0000-0002-6449-6725; Email: twlees@snu.ac.kr

Authors

Kyung Yeon Jang − *Department of Materials Science and Engineering, Seoul National University, Seoul 08826, Republic of Korea*

Bo-Hyun Choi − *Department of Materials Science and Engineering, Seoul National University, Seoul 08826, Republic of Korea*

Kyoo-Hyung Lee − *Department of Materials Science and Engineering, Seoul National University, Seoul 08826, Republic of Korea*

Chan-Yul Park − *Department of Materials Science and Engineering, Seoul National University, Seoul 08826, Republic of Korea*

Qingsen Zeng − *Department of Materials Science and Engineering, Seoul National University, Seoul 08826, Republic of Korea; Research Institute of Advanced Materials (RIAM), Seoul National University, Seoul 08826, Republic of Korea;* orcid.org/0000-0002-0877-0814

Complete contact information is available at: https://pubs.acs.org/10.1021/acs.chemrev.6c00202

Author Contributions

K. Y. J., B.-H. C., K.-H. L., C.-Y. P., and Q. Z. contributed equally; Kyung Yeon Jang, Bo-Hyun Choi, Kyoo-Hyung Lee, Chan-Yul Park, and Qingsen Zeng conceptualization, writing-original draft, writing-review and editing, visualization; Tae-Woo Lee conceptualization, writing-original draft, writing-review and editing, visualization, funding acquisition, supervision.

Notes

The authors declare no competing financial interest.

Biographies

Kyung Yeon Jang received his B.S. (2019) in the Department of Materials Science and Engineering from Seoul National University, Korea. He is a Ph.D. candidate in the Department of Materials Science and Engineering at Seoul National University. His research interests focus on the synthesis of perovskite nanoparticles, perovskite light-emitting diodes (PeLEDs), and photophysical analysis.

Bo-Hyun Choi received his B.S. in the Department of Materials Science & Engineering from Korea University in 2024. He is a Ph.D. candidate in the Department of Materials Science and Engineering of Seoul National University. His research interests focus on the perovskite polycrystalline light-emitting diode and enhancing its lifetime and efficiency.

Kyoo-Hyung Lee received his B.S. in the Department of Materials Science & Engineering from Korea University in 2025. He then entered the integrated master's and doctoral program at Seoul National University, where he is currently conducting research under the supervision of Professor Tae-Woo Lee. His research focuses on nanoscale-polycrystalline perovskites for LED applications.

Chan-Yul Park received his B.S. (2020) in the Department of Materials Science and Engineering from Korea University, Korea. He is a Ph.D. candidate in the Department of Materials Science and Engineering at Seoul National University. His research interests include perovskite thermal evaporation, bulk perovskite LEDs, and large-area PeLEDs.

Qingsen Zeng received his B.S. in Chemistry from Jilin University in 2014 and his Ph.D. in Polymer Chemistry and Physics from Jilin University in 2019 under the supervision of Prof. Bai Yang. He subsequently conducted postdoctoral research at Jilin University and at Seoul National University with Prof. Tae-Woo Lee. Since 2024, he has been an Assistant Research Professor in the Department of Materials Science and Engineering at Seoul National University. His research focuses on stabilizing perovskite nanocrystals and designing structurally ordered superlattice LEDs for next-generation display and lighting technologies.

Tae-Woo Lee is a professor in the Department of Materials Science and Engineering at Seoul National University, Korea. He received his Ph.D. in Chemical Engineering from KAIST, Korea, in 2002. He joined Bell Laboratories, USA, as a postdoctoral researcher and worked in Samsung Advanced Institute of Technology as a member of the research staff (2003−2008). He was appointed an MRS fellow in 2020 and an SPIE fellow in 2024. He was an associate professor in Materials Science and Engineering at Pohang University of Science and Technology (POSTECH), Korea until August 2016. His research focuses on printed flexible electronics based on organic and organic−inorganic hybrid materials for flexible displays, nerve-inspired artificial electronic devices, solid-state lighting, and solar energy conversion devices.

ACKNOWLEDGMENTS

This work was supported by the National Research Foundation of Korea (NRF) grant funded by the Korean government (Ministry of Science, ICT & Future Planning) (RS202500560490, 2022M3H4A1A04096380). This work

Downloaded from pubs.acs.org/chreav/article-pdf/doi/10.1021/acs.chemrev.6c00202/6880579/acs.chemrev.6c00202.pdf by guest on 10 October 2026

was also supported by the Technology Innovation Program (00235080, Development of layered color filters for enhancing low light sensitivity) funded By the Ministry of Trade, Industry & Energy (MOTIE, Korea).

REFERENCES

(1) Han, T.-H.; Jang, K. Y.; Dong, Y.; Friend, R. H.; Sargent, E. H.; Lee, T.-W. A Roadmap for the Commercialization of Perovskite Light Emitters. *Nat. Rev. Mater.* **2022**, *7* (10), 757−777.

(2) Fakharuddin, A.; Gangishetty, M. K.; Abdi-Jalebi, M.; Chin, S.-H.; bin Mohd Yusoff, Abd. R.; Congreve, D. N.; Tress, W.; Deschler, F.; Vasilopoulou, M.; Bolink, H. J. Perovskite Light-Emitting Diodes. *Nat. Electron.* **2022**, *5* (4), 203−216.

(3) Cho, H.; Jeong, S.-H.; Park, M.-H.; Kim, Y.-H.; Wolf, C.; Lee, C.-L.; Heo, J. H.; Sadhanala, A.; Myoung, N.; Yoo, S.; Im, S. H.; Friend, R. H.; Lee, T.-W. Overcoming the Electroluminescence Efficiency Limitations of Perovskite Light-Emitting Diodes. *Science* **2015**, *350* (6265), 1222−1225.

(4) Ban, M.; Zou, Y.; Rivett, J. P. H.; Yang, Y.; Thomas, T. H.; Tan, Y.; Song, T.; Gao, X.; Credgington, D.; Deschler, F.; Sirringhaus, H.; Sun, B. Solution-Processed Perovskite Light Emitting Diodes with Efficiency Exceeding 15% through Additive-Controlled Nanostructure Tailoring. *Nat. Commun.* **2018**, *9* (1), 3892.

(5) Wang, N.; Cheng, L.; Ge, R.; Zhang, S.; Miao, Y.; Zou, W.; Yi, C.; Sun, Y.; Cao, Y.; Yang, R.; Wei, Y.; Guo, Q.; Ke, Y.; Yu, M.; Jin, Y.; Liu, Y.; Ding, Q.; Di, D.; Yang, L.; Xing, G.; Tian, H.; Jin, C.; Gao, F.; Friend, R. H.; Wang, J.; Huang, W. Perovskite Light-Emitting Diodes Based on Solution-Processed Self-Organized Multiple Quantum Wells. *Nat. Photonics* **2016**, *10* (11), 699−704.

(6) Weerasinghe, H. C.; Macadam, N.; Kim, J.-E.; Sutherland, L. J.; Angmo, D.; Ng, L. W. T.; Scully, A. D.; Glenn, F.; Chantler, R.; Chang, N. L.; Dehghanimadvar, M.; Shi, L.; Ho-Baillie, A. W. Y.; Egan, R.; Chesman, A. S. R.; Gao, M.; Jasieniak, J. J.; Hasan, T.; Vak, D. The First Demonstration of Entirely Roll-to-Roll Fabricated Perovskite Solar Cell Modules under Ambient Room Conditions. *Nat. Commun.* **2024**, *15* (1), 1656.

(7) Kim, Y. Y.; Yang, T.-Y.; Suhonen, R.; Kemppainen, A.; Hwang, K.; Jeon, N. J.; Seo, J. Roll-to-Roll Gravure-Printed Flexible Perovskite Solar Cells Using Eco-Friendly Anti-solvent Bathing with Wide Processing Window. *Nat. Commun.* **2020**, *11* (1), 5146.

(8) Du, P.; Li, J.; Wang, L.; Sun, L.; Wang, X.; Xu, X.; Yang, L.; Pang, J.; Liang, W.; Luo, J.; Ma, Y.; Tang, J. Efficient and Large-Area All Vacuum-Deposited Perovskite Light-Emitting Diodes via Spatial Confinement. *Nat. Commun.* **2021**, *12* (1), 4751.

(9) Li, J.; Du, P.; Guo, Q.; Sun, L.; Shen, Z.; Zhu, J.; Dong, C.; Wang, L.; Zhang, X.; Li, L.; Yang, C.; Pan, J.; Liu, Z.; Xia, B.; Xiao, Z.; Du, J.; Song, B.; Luo, J.; Tang, J. Efficient All-Thermally Evaporated Perovskite Light-Emitting Diodes for Active-Matrix Displays. *Nat. Photonics* **2023**, *17* (5), 435−441.

(10) Hsieh, C.-A.; Tan, G.-H.; Chuang, Y.-T.; Lin, H.-C.; Lai, P.-T.; Jan, P.-E.; Chen, B.-H.; Lu, C.-H.; Yang, S.-D.; Hsiao, K.-Y.; Lu, M.-Y.; Chen, L.-Y.; Lin, H.-W. Vacuum-Deposited Inorganic Perovskite Light-Emitting Diodes with External Quantum Efficiency Exceeding 10% via Composition and Crystallinity Manipulation of Emission Layer under High Vacuum. *Adv. Sci.* **2023**, *10* (10), 2206076.

(11) Wei, Z.; Xing, J. The Rise of Perovskite Light-Emitting Diodes. *J. Phys. Chem. Lett.* **2019**, *10* (11), 3035−3042.

(12) Era, M.; Morimoto, S.; Tsutsui, T.; Saito, S. Organic-inorganic Heterostructure Electroluminescent Device Using a Layered Perovskite Semiconductor (C6H5C2H4NH3)2PbI4. *Appl. Phys. Lett.* **1994**, *65* (6), 676−678.

(13) Hong, X.; Ishihara, T.; Nurmikko, A. V. Photoconductivity and Electroluminescence in Lead Iodide Based Natural Quantum Well Structures. *Solid State Commun.* **1992**, *84* (6), 657−661.

(14) Hattori, T.; Taira, T.; Era, M.; Tsutsui, T.; Saito, S. Highly Efficient Electroluminescence from a Heterostructure Device Combined with Emissive Layered-Perovskite and an Electron-Transporting Organic Compound. *Chem. Phys. Lett.* **1996**, *254* (1), 103−108.

(15) Hong, X.; Ishihara, T.; Nurmikko, A. V. Dielectric Confinement Effect on Excitons in PbI4-Based Layered Semiconductors. *Phys. Rev. B* **1992**, *45* (12), 6961−6964.

(16) Ishihara, T.; Hong, X.; Ding, J.; Nurmikko, A. V. Dielectric Confinement Effect for Exciton and Biexciton States in PbI4-Based Two-Dimensional Semiconductor Structures. *Surf. Sci.* **1992**, *267* (1), 323−326.

(17) Tan, Z.-K.; Moghaddam, R. S.; Lai, M. L.; Docampo, P.; Higler, R.; Deschler, F.; Price, M.; Sadhanala, A.; Pazos, L. M.; Credgington, D.; Hanusch, F.; Bein, T.; Snaith, H. J.; Friend, R. H. Bright Light-Emitting Diodes Based on Organometal Halide Perovskite. *Nat. Nanotechnol.* **2014**, *9* (9), 687−692.

(18) Kim, Y.-H.; Cho, H.; Heo, J. H.; Kim, T.-S.; Myoung, N.; Lee, C.-L.; Im, S. H.; Lee, T.-W. Multicolored Organic/Inorganic Hybrid Perovskite Light-Emitting Diodes. *Adv. Mater.* **2015**, *27* (7), 1248−1254.

(19) Miyata, A.; Mitioglu, A.; Plochocka, P.; Portugall, O.; Wang, J. T.-W.; Stranks, S. D.; Snaith, H. J.; Nicholas, R. J. Direct Measurement of the Exciton Binding Energy and Effective Masses for Charge Carriers in Organic-Inorganic Tri-Halide Perovskites. *Nat. Phys.* **2015**, *11* (7), 582−587.

(20) Lee, T.-W.; Kim, Y.-H.; Cho, H. Wavelength Converting Particle, Method for Manufacturing Wavelength Converting Particle, and Light-Emitting Diode Containing Wavelength Converting Particle. WO2016072803A1, November 6, 2014.

(21) Lee, T.-W.; Im, S.; Kim, Y.-H.; Cho, H. Perovskite Nanocrystalline Particles and Optoelectronic Device Using Same. WO2016072805A1, November 6, 2014.

(22) Kim, J. S.; Heo, J.-M.; Park, G.-S.; Woo, S.-J.; Cho, C.; Yun, H. J.; Kim, D.-H.; Park, J.; Lee, S.-C.; Park, S.-H.; Yoon, E.; Greenham, N. C.; Lee, T.-W. Ultra-Bright, Efficient and Stable Perovskite Light-Emitting Diodes. *Nature* **2022**, *611* (7937), 688−694.

(23) Kim, Y.-H.; Kim, S.; Kakekhani, A.; Park, J.; Park, J.; Lee, Y.-H.; Xu, H.; Nagane, S.; Wexler, R. B.; Kim, D.-H.; Jo, S. H.; Martínez-Sarti, L.; Tan, P.; Sadhanala, A.; Park, G.-S.; Kim, Y.-W.; Hu, B.; Bolink, H. J.; Yoo, S.; Friend, R. H.; Rappe, A. M.; Lee, T.-W. Comprehensive Defect Suppression in Perovskite Nanocrystals for High-Efficiency Light-Emitting Diodes. *Nat. Photonics* **2021**, *15* (2), 148−155.

(24) Byun, J.; Cho, H.; Wolf, C.; Jang, M.; Sadhanala, A.; Friend, R. H.; Yang, H.; Lee, T.-W. Efficient Visible Quasi-2D Perovskite Light-Emitting Diodes. *Adv. Mater.* **2016**, *28* (34), 7515−7520.

(25) Jang, K. Y.; Chang, S. E.; Kim, D.-H.; Yoon, E.; Lee, T.-W. Nanocrystalline Perovskites for Bright and Efficient Light-Emitting Diodes. *Adv. Mater.* **2025**, *37* (25), 2415648.

(26) Song, Y.-H.; Li, B.; Wang, Z.-J.; Tai, X.-L.; Ding, G.-J.; Li, Z.-D.; Xu, H.; Hao, J.-M.; Song, K.-H.; Feng, L.-Z.; Hu, Y.-L.; Yin, Y.-C.; Zhu, B.-S.; Zhang, G.; Ju, H.; Zheng, G.; Hu, W.; Lin, Y.; Fan, F.; Yao, H.-B. Intragrain 3D Perovskite Heterostructure for High-Performance Pure-Red Perovskite LEDs. *Nature* **2025**, *641* (8062), 352−357.

(27) Chen, Y.; Wang, R.; Kusch, G.; Xu, B.; Hao, C.; Xue, C.; Cheng, L.; Zhu, L.; Wang, J.; Li, H.; Oliver, R. A.; Wang, N.; Huang, W.; Wang, J. All-Site Alloyed Perovskite for Efficient and Bright Blue Light-Emitting Diodes. *Nat. Commun.* **2025**, *16* (1), 3254.

(28) Gao, Y.; Cai, Q.; He, Y.; Zhang, D.; Cao, Q.; Zhu, M.; Ma, Z.; Zhao, B.; He, H.; Di, D.; Ye, Z.; Dai, X. Highly Efficient Blue Light-Emitting Diodes Based on Mixed-Halide Perovskites with Reduced Chlorine Defects. *Sci. Adv.* **2024**, *10* (29), No. eado5645.

(29) Kong, L.; Sun, Y.; Zhao, B.; Ji, K.; Feng, J.; Dong, J.; Wang, Y.; Liu, Z.; Maqbool, S.; Li, Y.; Yang, Y.; Dai, L.; Lee, W.; Cho, C.; Stranks, S. D.; Friend, R. H.; Wang, N.; Greenham, N. C.; Yang, X. Fabrication of Red-Emitting Perovskite LEDs by Stabilizing Their Octahedral Structure. *Nature* **2024**, *631* (8019), 73−79.

(30) Kim, J. S.; Lee, H.-D.; Jung, J. H.; Kim, T.; Woo, S.-J.; Yoon, H. J.; Moon, J.; Kang, C.; Chang, S.-E.; Kim, D.-H.; Kim, S.; Yang, H.; Kim, D.; Lee, T.-W. Kinetically-Controlled Intermediate-Direct-Pinning for Homogeneous Energy Landscapes in Quasi-Two-Dimensional Perovskites for Efficient and Narrow Blue Emission. *Nat. Commun.* **2025**, *16* (1), 9590.

Downloaded from pubs.acs.org/chreav/article-pdf/doi/10.1021/acs.chemrev.6c00202/68805793/acs.chemrev.6c00202.pdf by guest on 10 October 2026

(31) Kim, S.; Kim, S.-A.; Park, G.-S.; Kim, E.; Kim, D.-H.; Lee, S.-C.; Woo, S.-J.; Jang, Y.; Kweon, J. J.; Kang, S.; Lee, M.; Yun, H. J.; Park, S.; Shim, H.-J.; Kim, J. S.; Jang, K. Y.; Sung, M.-J.; Park, C.-Y.; Chang, S. E.; Park, J.; Park, J.; Lee, S. K.; Lee, T.-W. Cold-Injection Synthesis of Highly Emissive Perovskite Nanocrystals. *Nature* **2026**, *651*, 83−90.
(32) Li, M.; Yang, Y.; Kuang, Z.; Hao, C.; Wang, S.; Lu, F.; Liu, Z.; Liu, J.; Zeng, L.; Cai, Y.; Mao, Y.; Guo, J.; Tian, H.; Xing, G.; Cao, Y.; Ma, C.; Wang, N.; Peng, Q.; Zhu, L.; Huang, W.; Wang, J. Acceleration of Radiative Recombination for Efficient Perovskite LEDs. *Nature* **2024**, *630* (8017), 631−635.
(33) Baek, S.-D.; Shao, W.; Feng, W.; Tang, Y.; Lee, Y. H.; Loy, J.; Gunnarsson, W. B.; Yang, H.; Zhang, Y.; Faheem, M. B.; Kaswekar, P. I.; Atapattu, H. R.; Qin, J.; Coffey, A. H.; Park, J. Y.; Yang, S. J.; Yang, Y.-T.; Zhu, C.; Wang, K.; Graham, K. R.; Gao, F.; Qiao, Q.; Guo, L. J.; Rand, B. P.; Dou, L. Grain Engineering for Efficient Near-Infrared Perovskite Light-Emitting Diodes. *Nat. Commun.* **2024**, *15* (1), 10760.
(34) Li, Z.; Chen, Z.; Shi, Z.; Zou, G.; Chu, L.; Chen, X.-K.; Zhang, C.; So, S. K.; Yip, H.-L. Charge Injection Engineering at Organic/Inorganic Heterointerfaces for High-Efficiency and Fast-Response Perovskite Light-Emitting Diodes. *Nat. Commun.* **2023**, *14* (1), 6441.
(35) Coropceanu, V.; Cornil, J.; da Silva Filho, D. A.; Olivier, Y.; Silbey, R.; Brédas, J.-L. Charge Transport in Organic Semiconductors. *Chem. Rev.* **2007**, *107* (4), 926−952.
(36) Feng, S.-C.; Shen, Y.; Hu, X.-M.; Su, Z.-H.; Zhang, K.; Wang, B.-F.; Cao, L.-X.; Xie, F.-M.; Li, H.-Z.; Gao, X.; Tang, J.-X.; Li, Y.-Q. Efficient and Stable Red Perovskite Light-Emitting Diodes via Thermodynamic Crystallization Control. *Adv. Mater.* **2024**, *36* (44), 2410255.
(37) Zhao, B.; Guo, B.; Xing, S.; Liu, Z.; Yuan, Y.; Ren, Z.; Tang, W.; Lian, Y.; Zhang, G.; Zou, C.; Di, D. Highly Stable Perovskite Light-Emitting Diodes. *Matter* **2024**, *7* (3), 772−793.
(38) Zheng, S.; Wang, Z.; Jiang, N.; Huang, H.; Wu, X.; Li, D.; Teng, Q.; Li, J.; Li, C.; Li, J.; Pang, T.; Zeng, L.; Zhang, R.; Huang, F.; Lei, L.; Wu, T.; Yuan, F.; Chen, D. Ultralow Voltage-Driven Efficient and Stable Perovskite Light-Emitting Diodes. *Sci. Adv.* **2024**, *10* (36), No. eadp8473.
(39) Li, H.; Zhu, X.; Zhang, D.; Gao, Y.; Feng, Y.; Ma, Z.; Huang, J.; He, H.; Ye, Z.; Dai, X. Thermal Management towards Ultra-Bright and Stable Perovskite Nanocrystal-Based Pure Red Light-Emitting Diodes. *Nat. Commun.* **2024**, *15* (1), 6561.
(40) Xu, B.; Wang, W.; Zhang, X.; Liu, H.; Zhang, Y.; Mei, G.; Chen, S.; Wang, K.; Wang, L.; Sun, X. W. Electric Bias Induced Degradation in Organic-Inorganic Hybrid Perovskite Light-Emitting Diodes. *Sci. Rep.* **2018**, *8* (1), 15799.
(41) Lin, C.-H.; Hu, L.; Guan, X.; Kim, J.; Huang, C.-Y.; Huang, J.-K.; Singh, S.; Wu, T. Electrode Engineering in Halide Perovskite Electronics: Plenty of Room at the Interfaces. *Adv. Mater.* **2022**, *34* (18), 2108616.
(42) Seo, H.-K.; Kim, H.; Lee, J.; Park, M.-H.; Jeong, S.-H.; Kim, Y.-H.; Kwon, S.-J.; Han, T.-H.; Yoo, S.; Lee, T.-W. Efficient Flexible Organic/Inorganic Hybrid Perovskite Light-Emitting Diodes Based on Graphene Anode. *Adv. Mater.* **2017**, *29* (12), 1605587.
(43) Jiang, Y.; Cui, M.; Li, S.; Sun, C.; Huang, Y.; Wei, J.; Zhang, L.; Lv, M.; Qin, C.; Liu, Y.; Yuan, M. Reducing the Impact of Auger Recombination in Quasi-2D Perovskite Light-Emitting Diodes. *Nat. Commun.* **2021**, *12* (1), 336.
(44) Bawendi, M. G.; Steigerwald, M. L.; Brus, L. E. The Quantum Mechanics of Larger Semiconductor Clusters ("Quantum Dots"). *Annu. Rev. Phys. Chem.* **1990**, *41*, 477−496.
(45) Brus, L. Electronic Wave Functions in Semiconductor Clusters: Experiment and Theory. *J. Phys. Chem.* **1986**, *90* (12), 2555−2560.
(46) Ferreira, D. L.; Sousa, J. C. L.; Maronesi, R. N.; Bettini, J.; Schiavon, M. A.; Teixeira, A. V. N. C.; Silva, A. G. Size-Dependent Bandgap and Particle Size Distribution of Colloidal Semiconductor Nanocrystals. *J. Chem. Phys.* **2017**, *147* (15), 154102.
(47) Jang, H. M.; Kim, J.-S.; Heo, J.-M.; Lee, T.-W. Enhancing Photoluminescence Quantum Efficiency of Metal Halide Perovskites by Examining Luminescence-Limiting Factors. *APL Mater.* **2020**, *8* (2), 020904.
(48) Jang, H. M.; Jang, K. Y.; Lee, S. H.; Park, J.; Lee, T.-W. Exciton Bohr Radius of Lead Halide Perovskites for Photovoltaic and Light-Emitting Applications [Preprint]. *arXiv* **2025**, arXiv:2505.15565v1. (accessed June 16, 2026).
(49) Cahen, D.; Rakita, Y.; Egger, D. A.; Kahn, A. Surface Defects Control Bulk Carrier Densities in Polycrystalline Pb-Halide Perovskites. *Adv. Mater.* **2024**, *36* (50), 2407098.
(50) Olyaeefar, B.; Ahmadi-Kandjani, S.; Asgari, A. Classical Modelling of Grain Size and Boundary Effects in Polycrystalline Perovskite Solar Cells. *Sol. Energy Mater. Sol. Cells* **2018**, *180*, 76−82.
(51) Dörflinger, P.; Rieder, P.; Dyakonov, V. Temperature-Dependent Charge-Carrier Dynamics in Lead-Halide Perovskites: Indications for Dynamic Disorder Dominated Scattering Mechanism. *Adv. Energy Mater.* **2025**, *15* (20), 2403332.
(52) Johnston, M. B.; Herz, L. M. Hybrid Perovskites for Photovoltaics: Charge-Carrier Recombination, Diffusion, and Radiative Efficiencies. *Acc. Chem. Res.* **2016**, *49* (1), 146−154.
(53) Herz, L. M. Charge-Carrier Mobilities in Metal Halide Perovskites: Fundamental Mechanisms and Limits. *ACS Energy Lett.* **2017**, *2* (7), 1539−1548.
(54) Manser, J. S.; Christians, J. A.; Kamat, P. V. Intriguing Optoelectronic Properties of Metal Halide Perovskites. *Chem. Rev.* **2016**, *116* (21), 12956−13008.
(55) Kang, Y.; Han, S. Intrinsic Carrier Mobility of Cesium Lead Halide Perovskites. *Phys. Rev. Appl.* **2018**, *10* (4), 044013.
(56) Ulbricht, R.; Hendry, E.; Shan, J.; Heinz, T. F.; Bonn, M. Carrier Dynamics in Semiconductors Studied with Time-Resolved Terahertz Spectroscopy. *Rev. Mod. Phys.* **2011**, *83* (2), 543−586.
(57) Dong, Q.; Fang, Y.; Shao, Y.; Mulligan, P.; Qiu, J.; Cao, L.; Huang, J. Electron-Hole Diffusion Lengths > 175 Mm in Solution-Grown CH3NH3PbI3 Single Crystals. *Science* **2015**, *347* (6225), 967−970.
(58) Senanayak, S. P.; Yang, B.; Thomas, T. H.; Giesbrecht, N.; Huang, W.; Gann, E.; Nair, B.; Goedel, K.; Guha, S.; Moya, X.; McNeill, C. R.; Docampo, P.; Sadhanala, A.; Friend, R. H.; Sirringhaus, H. Understanding Charge Transport in Lead Iodide Perovskite Thin-Film Field-Effect Transistors. *Sci. Adv.* **2017**, *3* (1), No. e1601935.
(59) Reid, O. G.; Yang, M.; Kopidakis, N.; Zhu, K.; Rumbles, G. Grain-Size-Limited Mobility in Methylammonium Lead Iodide Perovskite Thin Films. *ACS Energy Lett.* **2016**, *1* (3), 561−565.
(60) Xia, C. Q.; Peng, J.; Poncé, S.; Patel, J. B.; Wright, A. D.; Crothers, T. W.; Uller Rothmann, M.; Borchert, J.; Milot, R. L.; Kraus, H.; Lin, Q.; Giustino, F.; Herz, L. M.; Johnston, M. B. Limits to Electrical Mobility in Lead-Halide Perovskite Semiconductors. *J. Phys. Chem. Lett.* **2021**, *12* (14), 3607−3617.
(61) Musiienko, A.; Pipek, J.; Praus, P.; Brynza, M.; Belas, E.; Dryzhakov, B.; Du, M.-H.; Ahmadi, M.; Grill, R. Deciphering the Effect of Traps on Electronic Charge Transport Properties of Methylammonium Lead Tribromide Perovskite. *Sci. Adv.* **2020**, *6* (37), No. eabb6393.
(62) Germs, W. C.; van der Holst, J. J. M.; van Mensfoort, S. L. M.; Bobbert, P. A.; Coehoorn, R. Modeling of the Transient Mobility in Disordered Organic Semiconductors with a Gaussian Density of States. *Phys. Rev. B* **2011**, *84* (16), 165210.
(63) Ni, Z.; Bao, C.; Liu, Y.; Jiang, Q.; Wu, W.-Q.; Chen, S.; Dai, X.; Chen, B.; Hartweg, B.; Yu, Z.; Holman, Z.; Huang, J. Resolving Spatial and Energetic Distributions of Trap States in Metal Halide Perovskite Solar Cells. *Science* **2020**, *367* (6484), 1352−1358.
(64) Sherkar, T. S.; Momblona, C.; Gil-Escrig, L.; Ávila, J.; Sessolo, M.; Bolink, H. J.; Koster, L. J. A. Recombination in Perovskite Solar Cells: Significance of Grain Boundaries, Interface Traps, and Defect Ions. *ACS Energy Lett.* **2017**, *2* (5), 1214−1222.
(65) Bi, C.; Yao, Z.; Hu, J.; Wang, X.; Zhang, M.; Tian, S.; Liu, A.; Lu, Y.; de Leeuw, N. H.; Sui, M.; Tian, J. Suppressing Auger Recombination of Perovskite Quantum Dots for Efficient Pure-Blue-Light-Emitting Diodes. *ACS Energy Lett.* **2023**, *8* (1), 731−739.
(66) Berestennikov, A. S.; Li, Y.; Iorsh, I. V.; Zakhidov, A. A.; Rogach, A. L.; Makarov, S. V. Beyond Quantum Confinement: Excitonic

Downloaded from pubs.acs.org/chreav/article-pdf/doi/10.1021/acs.chemrev.6c00202/68805793/acs.chemrev.6c00202.pdf by guest on 10 October 2026

Nonlocality in Halide Perovskite Nanoparticles with Mie Resonances. *Nanoscale* **2019**, *11* (14), 6747−6754.
(67) Chen, Y.; Filip, M. R. Tunable Interlayer Delocalization of Excitons in Layered Organic-Inorganic Halide Perovskites. *J. Phys. Chem. Lett.* **2023**, *14* (47), 10634−10641.
(68) Tilchin, J.; Dirin, D. N.; Maikov, G. I.; Sashchiuk, A.; Kovalenko, M. V.; Lifshitz, E. Hydrogen-like Wannier-Mott Excitons in Single Crystal of Methylammonium Lead Bromide Perovskite. *ACS Nano* **2016**, *10* (6), 6363−6371.
(69) Mauck, C. M.; Tisdale, W. A. Excitons in 2D Organic−Inorganic Halide Perovskites. *Trends Chem.* **2019**, *1* (4), 380−393.
(70) Sun, Y.; Ge, L.; Dai, L.; Cho, C.; Ferrer Orri, J.; Ji, K.; Zelewski, S. J.; Liu, Y.; Mirabelli, A. J.; Zhang, Y.; Huang, J.-Y.; Wang, Y.; Gong, K.; Lai, M. C.; Zhang, L.; Yang, D.; Lin, J.; Tennyson, E. M.; Ducati, C.; Stranks, S. D.; Cui, L.-S.; Greenham, N. C. Bright and Stable Perovskite Light-Emitting Diodes in the near-Infrared Range. *Nature* **2023**, *615* (7954), 830−835.
(71) Chakraborty, R.; Nag, A. Correlation of Dielectric Confinement and Excitonic Binding Energy in 2D Layered Hybrid Perovskites Using Temperature Dependent Photoluminescence. *J. Phys. Chem. C* **2020**, *124* (29), 16177−16185.
(72) Movilla, J. L.; Planelles, J.; Climente, J. I. Excitons in Metal Halide Perovskite Nanoplatelets: An Effective Mass Description of Polaronic, Dielectric and Quantum Confinement Effects. *Nanoscale Adv.* **2023**, *5* (22), 6093−6101.
(73) Holstein, B. R.; Swift, A. R. Barrier Penetration via Path Integrals. *Am. J. Phys.* **1982**, *50* (9), 833−839.
(74) Will, C. M.; Guinn, J. W. Tunneling near the Peaks of Potential Barriers: Consequences of Higher-Order Wentzel-Kramers-Brillouin Corrections. *Phys. Rev. A* **1988**, *37* (10), 3674−3679.
(75) Liu, Y.; Gibbs, M.; Puthussery, J.; Gaik, S.; Ihly, R.; Hillhouse, H. W.; Law, M. Dependence of Carrier Mobility on Nanocrystal Size and Ligand Length in PbSe Nanocrystal Solids. *Nano Lett.* **2010**, *10* (5), 1960−1969.
(76) Li, N.; Jia, Y.; Guo, Y.; Zhao, N. Ion Migration in Perovskite Light-Emitting Diodes: Mechanism, Characterizations, and Material and Device Engineering. *Adv. Mater.* **2022**, *34* (19), 2108102.
(77) Zhou, Y.; Li, M.; Yin, W.; Zeng, Q.; Zhao, Y.; Zhang, X. Beyond Thin Stacks: Physics, Materials, and Architectures of Thick Perovskite Light-Emitting Diodes. *Small* **2026**, *22*, No. e12877.
(78) Yoon, E.; Jang, K. Y.; Park, J.; Lee, T.-W. Understanding the Synergistic Effect of Device Architecture Design toward Efficient Perovskite Light-Emitting Diodes Using Interfacial Layer Engineering. *Adv. Mater. Interfaces* **2021**, *8* (3), 2001712.
(79) Xiong, W.; Tang, W.; Zhang, G.; Yang, Y.; Fan, Y.; Zhou, K.; Zou, C.; Zhao, B.; Di, D. Controllable P- and n-Type Behaviours in Emissive Perovskite Semiconductors. *Nature* **2024**, *633* (8029), 344−350.
(80) Cho, C.; Zhao, B.; Tainter, G. D.; Lee, J.-Y.; Friend, R. H.; Di, D.; Deschler, F.; Greenham, N. C. The Role of Photon Recycling in Perovskite Light-Emitting Diodes. *Nat. Commun.* **2020**, *11* (1), 611.
(81) Park, M.-H.; Park, J.; Lee, J.; So, H. S.; Kim, H.; Jeong, S.-H.; Han, T.-H.; Wolf, C.; Lee, H.; Yoo, S.; Lee, T.-W. Efficient Perovskite Light-Emitting Diodes Using Polycrystalline Core-Shell-Mimicked Nanograins. *Adv. Funct. Mater.* **2019**, *29* (22), 1902017.
(82) Chu, S.; Zhang, Y.; Xiao, P.; Chen, W.; Tang, R.; Shao, Y.; Chen, T.; Zhang, X.; Liu, F.; Xiao, Z. Large-Area and Efficient Sky-Blue Perovskite Light-Emitting Diodes via Blade-Coating. *Adv. Mater.* **2022**, *34* (16), 2108939.
(83) Han, J.; Ha, J. M.; Kweon, S. H.; Noh, Y. W.; Lee, D.; Lee, M. H.; Kim, N.; Shin, J. K.; Park, S.; Min, J. W.; Im, W. B.; Kwak, S. K.; Song, M. H.; Woo, H. Y. Fine-Modulation of Perovskite Ion-Additive Binding Interaction Using Multidentate Ligation for High Performance Perovskite Light-Emitting Diodes. *ACS Nano* **2025**, *19* (1), 1044−1055.
(84) Liu, C.; Cheng, Y.-B.; Ge, Z. Understanding of Perovskite Crystal Growth and Film Formation in Scalable Deposition Processes. *Chem. Soc. Rev.* **2020**, *49* (6), 1653−1687.
(85) Gao, Q.; Qi, J.; Chen, K.; Xia, M.; Hu, Y.; Mei, A.; Han, H. Halide Perovskite Crystallization Processes and Methods in Nanocrystals, Single Crystals, and Thin Films. *Adv. Mater.* **2022**, *34* (52), 2200720.
(86) Zhang, Y.; Liu, Y.; Xu, Z.; Ye, H.; Yang, Z.; You, J.; Liu, M.; He, Y.; Kanatzidis, M. G.; Liu, S. Nucleation-Controlled Growth of Superior Lead-Free Perovskite Cs3Bi2I9 Single-Crystals for High-Performance X-Ray Detection. *Nat. Commun.* **2020**, *11* (1), 2304.
(87) Sánchez, S.; Pfeifer, L.; Vlachopoulos, N.; Hagfeldt, A. Rapid Hybrid Perovskite Film Crystallization from Solution. *Chem. Soc. Rev.* **2021**, *50* (12), 7108−7131.
(88) Adhyaksa, G. W. P.; Brittman, S.; Aboliņš, H.; Lof, A.; Li, X.; Keelor, J. D.; Luo, Y.; Duevski, T.; Heeren, R. M. A.; Ellis, S. R.; Fenning, D. P.; Garnett, E. C. Understanding Detrimental and Beneficial Grain Boundary Effects in Halide Perovskites. *Adv. Mater.* **2018**, *30* (52), 1804792.
(89) An, Q.; Paulus, F.; Becker-Koch, D.; Cho, C.; Sun, Q.; Weu, A.; Bitton, S.; Tessler, N.; Vaynzof, Y. Small Grains as Recombination Hot Spots in Perovskite Solar Cells. *Matter* **2021**, *4* (5), 1683−1701.
(90) Jang, J. W.; Woo, J. Y.; Lee, C. B.; Kim, W. D.; Park, J.; Kim, D.; Zhao, Y.; Yeo, J.-S.; Kim, M. G.; Nam, S. H.; Lee, S. H.; Kim, Y.-H.; Lee, D. R.; Yang, Y.; Kim, K.; Han, T.-H. Chemically Designed Crystal Growth Termination for High-Luminance and Stable Polycrystalline Perovskite LEDs. *ACS Energy Lett.* **2024**, *9* (12), 6029−6038.
(91) Hamill, J. C., Jr.; Schwartz, J.; Loo, Y.-L. Influence of Solvent Coordination on Hybrid Organic-Inorganic Perovskite Formation. *ACS Energy Lett.* **2018**, *3* (1), 92−97.
(92) Zuo, W.; Byranvand, M. M.; Kodalle, T.; Zohdi, M.; Lim, J.; Carlsen, B.; Magorian Friedlmeier, T.; Kot, M.; Das, C.; Flege, J. I.; Zong, W.; Abate, A.; Sutter-Fella, C. M.; Li, M.; Saliba, M. Coordination Chemistry as a Universal Strategy for a Controlled Perovskite Crystallization. *Adv. Mater.* **2023**, *35* (39), 2302889.
(93) Rong, Y.; Tang, Z.; Zhao, Y.; Zhong, X.; Venkatesan, S.; Graham, H.; Patton, M.; Jing, Y.; Guloy, A. M.; Yao, Y. Solvent Engineering towards Controlled Grain Growth in Perovskite Planar Heterojunction Solar Cells. *Nanoscale* **2015**, *7* (24), 10595−10599.
(94) Jiang, Y.; Sun, C.; Xu, J.; Li, S.; Cui, M.; Fu, X.; Liu, Y.; Liu, Y.; Wan, H.; Wei, K.; Zhou, T.; Zhang, W.; Yang, Y.; Yang, J.; Qin, C.; Gao, S.; Pan, J.; Liu, Y.; Hoogland, S.; Sargent, E. H.; Chen, J.; Yuan, M. Synthesis-on-Substrate of Quantum Dot Solids. *Nature* **2022**, *612* (7941), 679−684.
(95) Jiang, Y.; Wei, K.; Sun, C.; Feng, Y.; Zhang, L.; Cui, M.; Li, S.; Li, W.-D.; Kim, J. T.; Qin, C.; Yuan, M. Unraveling Size-Dependent Ion-Migration for Stable Mixed-Halide Perovskite Light-Emitting Diodes. *Adv. Mater.* **2023**, *35* (39), 2304094.
(96) Yu, Y.; Wang, B.-F.; Shen, Y.; Su, Z.-H.; Zhang, K.; Ren, H.; Zhang, Y.-F.; Gao, X.; Tang, J.-X.; Li, Y.-Q. Regulating Perovskite Crystallization through Interfacial Engineering Using a Zwitterionic Additive Potassium Sulfamate for Efficient Pure-Blue Light-Emitting Diodes. *Angew. Chem., Int. Ed.* **2024**, *63* (7), No. e202319730.
(97) Liang, A.; Gao, Y.; Asadpour, R.; Wei, Z.; Finkenauer, B. P.; Jin, L.; Yang, J.; Wang, K.; Chen, K.; Liao, P.; Zhu, C.; Huang, L.; Boudouris, B. W.; Alam, M. A.; Dou, L. Ligand-Driven Grain Engineering of High Mobility Two-Dimensional Perovskite Thin-Film Transistors. *J. Am. Chem. Soc.* **2021**, *143* (37), 15215−15223.
(98) Sun, C.; Jiang, Y.; Zhang, L.; Wei, K.; Yuan, M. Toward the Controlled Synthesis of Lead Halide Perovskite Nanocrystals. *ACS Nano* **2023**, *17* (18), 17600.
(99) Park, M.-H.; Jeong, S.-H.; Seo, H.-K.; Wolf, C.; Kim, Y.-H.; Kim, H.; Byun, J.; Kim, J. S.; Cho, H.; Lee, T.-W. Unravelling Additive-Based Nanocrystal Pinning for High Efficiency Organic-Inorganic Halide Perovskite Light-Emitting Diodes. *Nano Energy* **2017**, *42*, 157−165.
(100) Paek, S.; Schouwink, P.; Athanasopoulou, E. N.; Cho, K. T.; Grancini, G.; Lee, Y.; Zhang, Y.; Stellacci, F.; Nazeeruddin, M. K.; Gao, P. From Nano- to Micrometer Scale: The Role of Anti-solvent Treatment on High Performance Perovskite Solar Cells. *Chem. Mater.* **2017**, *29* (8), 3490−3498.
(101) Zhou, Y.; Yang, M.; Game, O. S.; Wu, W.; Kwun, J.; Strauss, M. A.; Yan, Y.; Huang, J.; Zhu, K.; Padture, N. P. Manipulating Crystallization of Organolead Mixed-Halide Thin Films in Anti-solvent

Downloaded from pubs.acs.org/chreav/article-pdf/doi/10.1021/acs.chemrev.6c00202/68805793/acs.chemrev.6c00202.pdf by guest on 10 October 2026

Baths for Wide-Bandgap Perovskite Solar Cells. *ACS Appl. Mater. Interfaces* **2016**, *8* (3), 2232−2237.
(102) Meggiolaro, D.; Mosconi, E.; De Angelis, F. Formation of Surface Defects Dominates Ion Migration in Lead-Halide Perovskites. *ACS Energy Lett.* **2019**, *4* (3), 779−785.
(103) Xue, J.; Wang, R.; Yang, Y. The Surface of Halide Perovskites from Nano to Bulk. *Nat. Rev. Mater.* **2020**, *5* (11), 809−827.
(104) Shargaieva, O.; Lang, F.; Rappich, J.; Dittrich, T.; Klaus, M.; Meixner, M.; Genzel, C.; Nickel, N. H. Influence of the Grain Size on the Properties of CH3NH3PbI3 Thin Films. *ACS Appl. Mater. Interfaces* **2017**, *9* (44), 38428−38435.
(105) Li, Z.; Ren, Z.; Liang, Q.; Fong, P. W. K.; Liu, H.; Lu, X.; Kymissis, I.; Li, G. Grain Orientation Management and Recombination Suppression for Ultra-Stable PeLEDs with Record Brightness. *Joule* **2024**, *8* (4), 1176−1190.
(106) Wetzelaer, G.-J. A. H.; Scheepers, M.; Sempere, A. M.; Momblona, C.; Ávila, J.; Bolink, H. J. Trap-Assisted Non-Radiative Recombination in Organic-Inorganic Perovskite Solar Cells. *Adv. Mater.* **2015**, *27* (11), 1837−1841.
(107) Srimath Kandada, A. R.; Neutzner, S.; D'Innocenzo, V.; Tassone, F.; Gandini, M.; Akkerman, Q. A.; Prato, M.; Manna, L.; Petrozza, A.; Lanzani, G. Nonlinear Carrier Interactions in Lead Halide Perovskites and the Role of Defects. *J. Am. Chem. Soc.* **2016**, *138* (41), 13604−13611.
(108) Meng, Y.; Guan, X.; Weng, Y.; Lu, J.; Li, Y.; Zhao, Y.; Li, M.; Feng, W.; Sun, C.; Lin, J.; Wei, Z. Bi-Functional Phosphine Oxide Passivator for Efficient Near-Infrared Sn-Based Perovskite Light-Emitting Diodes with Ultra-Low Efficiency Roll-Off. *Adv. Funct. Mater.* **2024**, *34* (13), 2310530.
(109) Deng, Y.; Zhang, Z.; Ren, G.; Liu, W.; Li, Z.; Liu, C.; Li, Z.; Guo, W. Managing Surface Reconstruction Enables Bright, Stable, and Cost-Performance Perovskite Light-Emitting Diodes. *Laser Photon. Rev.* **2025**, *19* (9), 2401817.
(110) Hu, M.; Zhu, Y.; Zhou, Z.; Hao, M.; Harnmanasvate, C.; Waiyawat, J.; Wang, Y.; Lu, J.; An, Q.; Li, X.; Zhang, T.; Zhou, Y.; Cheacharoen, R.; Rong, Y. Post-Treatment of Metal Halide Perovskites: From Morphology Control, Defect Passivation to Band Alignment and Construction of Heterostructures. *Adv. Energy Mater.* **2023**, *13* (41), 2301888.
(111) Park, K.; Lee, J.-H.; Lee, J.-W. Surface Defect Engineering of Metal Halide Perovskites for Photovoltaic Applications. *ACS Energy Lett.* **2022**, *7* (3), 1230−1239.
(112) Gao, Y.; Wu, Y.; Liu, Y.; Chen, C.; Bai, X.; Yang, L.; Shi, Z.; Yu, W. W.; Dai, Q.; Zhang, Y. Dual Functions of Crystallization Control and Defect Passivation Enabled by an Ionic Compensation Strategy for Stable and High-Efficient Perovskite Solar Cells. *ACS Appl. Mater. Interfaces* **2020**, *12* (3), 3631−3641.
(113) Chen, B.; Rudd, P. N.; Yang, S.; Yuan, Y.; Huang, J. Imperfections and Their Passivation in Halide Perovskite Solar Cells. *Chem. Soc. Rev.* **2019**, *48* (14), 3842−3867.
(114) Stewart, R. J.; Grieco, C.; Larsen, A. V.; Maier, J. J.; Asbury, J. B. Approaching Bulk Carrier Dynamics in Organo-Halide Perovskite Nanocrystalline Films by Surface Passivation. *J. Phys. Chem. Lett.* **2016**, *7* (7), 1148−1153.
(115) Xie, Y.-M.; Xue, Q.; Yip, H.-L. Metal-Halide Perovskite Crystallization Kinetics: A Review of Experimental and Theoretical Studies. *Adv. Energy Mater.* **2021**, *11* (24), 2100784.
(116) Lee, J.-W.; Kim, H.-S.; Park, N.-G. Lewis Acid-Base Adduct Approach for High Efficiency Perovskite Solar Cells. *Acc. Chem. Res.* **2016**, *49* (2), 311−319.
(117) Yan, K.; Long, M.; Zhang, T.; Wei, Z.; Chen, H.; Yang, S.; Xu, J. Hybrid Halide Perovskite Solar Cell Precursors: Colloidal Chemistry and Coordination Engineering behind Device Processing for High Efficiency. *J. Am. Chem. Soc.* **2015**, *137* (13), 4460−4468.
(118) Guo, Y.; Tang, Z.; Li, Z.; Wu, J.; Fu, Y.; Liu, J.; Xie, Z. Weakly Coordinated Co-Solvent Strategy Enables Anti-Solvent-Free Fabrication of High-Efficiency Perovskite Light-Emitting Diodes. *Adv. Funct. Mater.* **2026**, *36* (11), No. e17075.
(119) Radicchi, E.; Mosconi, E.; Elisei, F.; Nunzi, F.; De Angelis, F. Understanding the Solution Chemistry of Lead Halide Perovskites Precursors. *ACS Appl. Energy Mater.* **2019**, *2* (5), 3400−3409.
(120) Jung, M.; Ji, S.-G.; Kim, G.; Seok, S. Il. Perovskite Precursor Solution Chemistry: From Fundamentals to Photovoltaic Applications. *Chem. Soc. Rev.* **2019**, *48* (7), 2011−2038.
(121) Zhang, S.; Ma, F.; Jiang, J.; Wang, Z.; Kwok, R. T. K.; Qiu, Z.; Zhao, Z.; Lam, J. W. Y.; Tang, B. Z. Aggregative Luminescence from CsPbBr3 Perovskite Precursors. *Angew. Chem., Int. Ed.* **2024**, *63* (35), No. e202408586.
(122) Zhang, S.; Wang, J.; Jiang, J.; Ma, F.; Wang, Y.; Chen, X.; Kwok, R. T. K.; Zhao, Z.; Lam, J. W. Y.; Tang, B. Z. Illuminating Lead Coordination in Perovskite Precursors via Fluorescence Spectroscopy. *Angew. Chem., Int. Ed.* **2025**, *64* (22), No. e202500294.
(123) Liu, M.; Zhao, J.; Luo, Z.; Sun, Z.; Pan, N.; Ding, H.; Wang, X. Unveiling Solvent-Related Effect on Phase Transformations in CsBr-PbBr2 System: Coordination and Ratio of Precursors. *Chem. Mater.* **2018**, *30* (17), 5846−5852.
(124) Zhang, Z.; Liang, J.; Wang, J.; Zheng, Y.; Wu, X.; Tian, C.; Sun, A.; Huang, Y.; Zhou, Z.; Yang, Y.; Liu, Y.; Tang, C.; Chen, C.-C. DMSO-Free Solvent Strategy for Stable and Efficient Methylammonium-Free Sn-Pb Alloyed Perovskite Solar Cells. *Adv. Energy Mater.* **2023**, *13* (17), 2300181.
(125) Wang, Y.; Li, L.; Wu, Z.; Zhang, R.; Hong, J.; Zhang, J.; Rao, H.; Pan, Z.; Zhong, X. Self-Driven Prenucleation-Induced Perovskite Crystallization Enables Efficient Perovskite Solar Cells. *Angew. Chem., Int. Ed.* **2023**, *62* (22), No. e202302342.
(126) Rahimnejad, S.; Kovalenko, A.; Forés, S. M.; Aranda, C.; Guerrero, A. Coordination Chemistry Dictates the Structural Defects in Lead Halide Perovskites. *ChemPhysChem* **2016**, *17* (18), 2795−2798.
(127) Nasti, G.; Aldamasy, M. H.; Flatken, M. A.; Musto, P.; Matczak, P.; Dallmann, A.; Hoell, A.; Musiienko, A.; Hempel, H.; Aktas, E.; Di Girolamo, D.; Pascual, J.; Li, G.; Li, M.; Mercaldo, L. V.; Veneri, P. D.; Abate, A. Pyridine Controlled Tin Perovskite Crystallization. *ACS Energy Lett.* **2022**, *7* (10), 3197−3203.
(128) Zhou, Y.; Najar, A.; Zhang, J.; Feng, J.; Cao, Y.; Li, Z.; Zhu, X.; Yang, D.; Liu, S. F. Effect of Solvent Residue in the Thin-Film Fabrication on Perovskite Solar Cell Performance. *ACS Appl. Mater. Interfaces* **2022**, *14* (25), 28729−28737.
(129) Wu, G.; Li, H.; Cui, J.; Zhang, Y.; Olthof, S.; Chen, S.; Liu, Z.; Wang, D.; Liu, S. Solvent Engineering Using a Volatile Solid for Highly Efficient and Stable Perovskite Solar Cells. *Adv. Sci.* **2020**, *7* (10), 1903250.
(130) Zhang, H.; Darabi, K.; Nia, N. Y.; Krishna, A.; Ahlawat, P.; Guo, B.; Almalki, M. H. S.; Su, T.-S.; Ren, D.; Bolnykh, V.; Castriotta, L. A.; Zendehdel, M.; Pan, L.; Alonso, S. S.; Li, R.; Zakeeruddin, S. M.; Hagfeldt, A.; Rothlisberger, U.; Di Carlo, A.; Amassian, A.; Grätzel, M. A Universal Co-Solvent Dilution Strategy Enables Facile and Cost-Effective Fabrication of Perovskite Photovoltaics. *Nat. Commun.* **2022**, *13* (1), 89.
(131) Li, B.; Binks, D.; Cao, G.; Tian, J. Engineering Halide Perovskite Crystals through Precursor Chemistry. *Small* **2019**, *15* (47), 1903613.
(132) Li, J.; Dagar, J.; Shargaieva, O.; Flatken, M. A.; Köbler, H.; Fenske, M.; Schultz, C.; Stegemann, B.; Just, J.; Többens, D. M.; Abate, A.; Munir, R.; Unger, E. 20.8% Slot-Die Coated MAPbI3 Perovskite Solar Cells by Optimal DMSO-Content and Age of 2-ME Based Precursor Inks. *Adv. Energy Mater.* **2021**, *11* (10), 2003460.
(133) Liang, Q.; Liu, K.; Sun, M.; Ren, Z.; Fong, P. W. K.; Huang, J.; Qin, M.; Wu, Z.; Shen, D.; Lee, C.-S.; Hao, J.; Lu, X.; Huang, B.; Li, G. Manipulating Crystallization Kinetics in High-Performance Blade-Coated Perovskite Solar Cells via Cosolvent-Assisted Phase Transition. *Adv. Mater.* **2022**, *34* (16), 2200276.
(134) Cao, X.; Zhi, L.; Jia, Y.; Li, Y.; Zhao, K.; Cui, X.; Ci, L.; Zhuang, D.; Wei, J. A Review of the Role of Solvents in Formation of High-Quality Solution-Processed Perovskite Films. *ACS Appl. Mater. Interfaces* **2019**, *11* (8), 7639−7654.
(135) Zhu, L.; Cao, H.; Xue, C.; Zhang, H.; Qin, M.; Wang, J.; Wen, K.; Fu, Z.; Jiang, T.; Xu, L.; Zhang, Y.; Cao, Y.; Tu, C.; Zhang, J.; Liu, D.; Zhang, G.; Kong, D.; Fan, N.; Li, G.; Yi, C.; Peng, Q.; Chang, J.; Lu, X.;

Downloaded from pubs.acs.org/chreav/article-pdf/doi/10.1021/acs.chemrev.6c00202/6880579/acs.chemrev.6c00202.pdf by guest on 10 October 2026

Wang, N.; Huang, W.; Wang, J. Unveiling the Additive-Assisted Oriented Growth of Perovskite Crystallite for High Performance Light-Emitting Diodes. *Nat. Commun.* **2021**, *12* (1), 5081.
(136) Xu, C.; Zhang, Z.; Zhang, S.; Si, H.; Ma, S.; Fan, W.; Xiong, Z.; Liao, Q.; Sattar, A.; Kang, Z.; Zhang, Y. Manipulation of Perovskite Crystallization Kinetics via Lewis Base Additives. *Adv. Funct. Mater.* **2021**, *31* (13), 2009425.
(137) Miao, Y.; Chen, Y.; Chen, H.; Wang, X.; Zhao, Y. Using Steric Hindrance to Manipulate and Stabilize Metal Halide Perovskites for Optoelectronics. *Chem. Sci.* **2021**, *12* (21), 7231−7247.
(138) Zhao, L.; Yeh, Y.-W.; Tran, N. L.; Wu, F.; Xiao, Z.; Kerner, R. A.; Lin, Y. L.; Scholes, G. D.; Yao, N.; Rand, B. P. In Situ Preparation of Metal Halide Perovskite Nanocrystal Thin Films for Improved Light-Emitting Devices. *ACS Nano* **2017**, *11* (4), 3957−3964.
(139) Lee, S.; Park, J. H.; Nam, Y. S.; Lee, B. R.; Zhao, B.; Di Nuzzo, D.; Jung, E. D.; Jeon, H.; Kim, J.-Y.; Jeong, H. Y.; Friend, R. H.; Song, M. H. Growth of Nanosized Single Crystals for Efficient Perovskite Light-Emitting Diodes. *ACS Nano* **2018**, *12* (4), 3417−3423.
(140) Guo, Y.; Apergi, S.; Li, N.; Chen, M.; Yin, C.; Yuan, Z.; Gao, F.; Xie, F.; Brocks, G.; Tao, S.; Zhao, N. Phenylalkylammonium Passivation Enables Perovskite Light Emitting Diodes with Record High-Radiance Operational Lifetime: The Chain Length Matters. *Nat. Commun.* **2021**, *12* (1), 644.
(141) Sun, W.; Yun, R.; Liu, Y.; Zhang, X.; Yuan, M.; Zhang, L.; Li, X. Ligands in Lead Halide Perovskite Nanocrystals: From Synthesis to Optoelectronic Applications. *Small* **2023**, *19* (11), 2205950.
(142) Liu, Z.; Wang, G.; Kong, L.; Wang, J.; Wang, Y.; Du, P.; Wang, L.; Wang, S.; Rogach, A. L.; Yang, X. Simultaneous Regulation of Crystallization and Suppression of Oxidation in CsSnI3 Perovskite Enables Efficient and Stable Near-Infrared Light-Emitting Diodes. *Nano Lett.* **2025**, *25* (17), 7061−7068.
(143) Warby, J. H.; Wenger, B.; Ramadan, A. J.; Oliver, R. D. J.; Sansom, H. C.; Marshall, A. R.; Snaith, H. J. Revealing Factors Influencing the Operational Stability of Perovskite Light-Emitting Diodes. *ACS Nano* **2020**, *14* (7), 8855−8865.
(144) Shen, Y.; Wu, H.-Y.; Li, Y.-Q.; Shen, K.-C.; Gao, X.; Song, F.; Tang, J.-X. Interfacial Nucleation Seeding for Electroluminescent Manipulation in Blue Perovskite Light-Emitting Diodes. *Adv. Funct. Mater.* **2021**, *31* (45), 2103870.
(145) Ma, D.; Lin, K.; Dong, Y.; Choubisa, H.; Proppe, A. H.; Wu, D.; Wang, Y.-K.; Chen, B.; Li, P.; Fan, J. Z.; Yuan, F.; Johnston, A.; Liu, Y.; Kang, Y.; Lu, Z.-H.; Wei, Z.; Sargent, E. H. Distribution Control Enables Efficient Reduced-Dimensional Perovskite LEDs. *Nature* **2021**, *599* (7886), 594−598.
(146) Liu, Z.; Qiu, W.; Peng, X.; Sun, G.; Liu, X.; Liu, D.; Li, Z.; He, F.; Shen, C.; Gu, Q.; Ma, F.; Yip, H.-L.; Hou, L.; Qi, Z.; Su, S.-J. Perovskite Light-Emitting Diodes with EQE Exceeding 28% through a Synergetic Dual-Additive Strategy for Defect Passivation and Nanostructure Regulation. *Adv. Mater.* **2021**, *33* (43), 2103268.
(147) Wang, H.; Zhang, X.; Wu, Q.; Cao, F.; Yang, D.; Shang, Y.; Ning, Z.; Zhang, W.; Zheng, W.; Yan, Y.; Kershaw, S. V.; Zhang, L.; Rogach, A. L.; Yang, X. Trifluoroacetate Induced Small-Grained CsPbBr3 Perovskite Films Result in Efficient and Stable Light-Emitting Devices. *Nat. Commun.* **2019**, *10* (1), 665.
(148) Lee, S.; Kim, J.; Kim, H.; Kim, C.; Kim, S.; Kim, C.; Lee, H.; Choi, B.; Muthu, C.; Kim, T.; Lee, J.; Lee, S.; Ihee, H.; Lee, J.-Y. Brightening Deep-Blue Perovskite Light-Emitting Diodes: A Path to Rec. 2020. *Sci. Adv.* **2024**, *10* (20), No. eadn8465.
(149) Zhang, J.; Xing, X.; Qian, D.; Wang, A.; Gu, L.; Kuang, Z.; Wang, J.; Zhang, H.; Wen, K.; Xu, W.; Niu, M.; Du, X.; Yuan, L.; Cao, C.; Cao, Y.; Zhu, L.; Wang, N.; Yi, C.; Huang, W.; Wang, J. Sulfonic Zwitterion for Passivating Deep and Shallow Level Defects in Perovskite Light-Emitting Diodes. *Adv. Funct. Mater.* **2022**, *32* (22), 2111578.
(150) Wang, N.; Cheng, L.; Si, J.; Liang, X.; Jin, Y.; Wang, J.; Huang, W. Morphology Control of Perovskite Light-Emitting Diodes by Using Amino Acid Self-Assembled Monolayers. *Appl. Phys. Lett.* **2016**, *108* (14), 141102.
(151) Park, J. H.; Lee, A.; Yu, J. C.; Nam, Y. S.; Choi, Y.; Park, J.; Song, M. H. Surface Ligand Engineering for Efficient Perovskite Nanocrystal-Based Light-Emitting Diodes. *ACS Appl. Mater. Interfaces* **2019**, *11* (8), 8428−8435.
(152) Zhang, B.-B.; Yuan, S.; Ma, J.-P.; Zhou, Y.; Hou, J.; Chen, X.; Zheng, W.; Shen, H.; Wang, X.-C.; Sun, B.; Bakr, O. M.; Liao, L.-S.; Sun, H.-T. General Mild Reaction Creates Highly Luminescent Organic-Ligand-Lacking Halide Perovskite Nanocrystals for Efficient Light-Emitting Diodes. *J. Am. Chem. Soc.* **2019**, *141* (38), 15423−15432.
(153) Xiao, Z.; Kerner, R. A.; Tran, N.; Zhao, L.; Scholes, G. D.; Rand, B. P. Engineering Perovskite Nanocrystal Surface Termination for Light-Emitting Diodes with External Quantum Efficiency Exceeding 15%. *Adv. Funct. Mater.* **2019**, *29* (11), 1807284.
(154) Hassan, Y.; Park, J. H.; Crawford, M. L.; Sadhanala, A.; Lee, J.; Sadighian, J. C.; Mosconi, E.; Shivanna, R.; Radicchi, E.; Jeong, M.; Yang, C.; Choi, H.; Park, S. H.; Song, M. H.; De Angelis, F.; Wong, C. Y.; Friend, R. H.; Lee, B. R.; Snaith, H. J. Ligand-Engineered Bandgap Stability in Mixed-Halide Perovskite LEDs. *Nature* **2021**, *591* (7848), 72−77.
(155) Zou, Y.; Teng, P.; Xu, W.; Zheng, G.; Lin, W.; Yin, J.; Kobera, L.; Abbrent, S.; Li, X.; Steele, J. A.; Solano, E.; Roeffaers, M. B. J.; Li, J.; Cai, L.; Kuang, C.; Scheblykin, I. G.; Brus, J.; Zheng, K.; Yang, Y.; Mohammed, O. F.; Bakr, O. M.; Pullerits, T.; Bai, S.; Sun, B.; Gao, F. Manipulating Crystallization Dynamics through Chelating Molecules for Bright Perovskite Emitters. *Nat. Commun.* **2021**, *12* (1), 4831.
(156) Zhao, C.; Wu, W.; Zhan, H.; Yuan, W.; Li, H.; Zhang, D.; Wang, D.; Cheng, Y.; Shao, S.; Qin, C.; Wang, L. Phosphonate/Phosphine Oxide Dyad Additive for Efficient Perovskite Light-Emitting Diodes. *Angew. Chem., Int. Ed.* **2022**, *61* (13), No. e202117374.
(157) Deng, Y.; Zhang, Z.; Ren, G.; Li, Z.; Liu, C.; Guo, W. An Easily Developed Difunctional Molecule Enabling Highly Efficient and Stable Light-Emitting Diodes. *Adv. Funct. Mater.* **2023**, *33* (48), 2305423.
(158) Zhan, W.; Wang, H.; Guo, J.; Liang, Y.; Wang, Y.; Wu, J.; Dang, Z.; Zhang, N.; Cao, J.; Fan, Y.; Zou, Y.; Li, B.; Wang, Y.; Chen, Y.; Miao, Y.; Zhao, Y. Bulk Fabrication of Space-Confined CsPbI3 Nanocrystal Films Toward Efficient and Bright Deep-Red LEDs. *Adv. Mater.* **2026**, *38* (9), No. e18255.
(159) Sun, X.; Meng, W.; Ngai, K. H.; Nie, Z.; Luan, C.; Zhang, W.; Li, S.; Lu, X.; Wu, B.; Zhou, G.; Long, M.; Xu, J. Regulating Surface-Passivator Binding Priority for Efficient Perovskite Light-Emitting Diodes. *Adv. Mater.* **2024**, *36* (25), 2400347.
(160) Shang, Y.; Liao, Y.; Wei, Q.; Wang, Z.; Xiang, B.; Ke, Y.; Liu, W.; Ning, Z. Highly Stable Hybrid Perovskite Light-Emitting Diodes Based on Dion-Jacobson Structure. *Sci. Adv.* **2019**, *5* (8), No. eaaw8072.
(161) Liu, Y.; Wang, S.; Yu, Z.; Chen, G.; Wang, C.; Wang, T.; Ke, W.; Fang, G. A Multifunctional Additive Strategy Enables Efficient Pure-Blue Perovskite Light-Emitting Diodes. *Adv. Mater.* **2023**, *35* (35), 2302161.
(162) Liu, S.; Guo, Z.; Wu, X.; Liu, X.; Huang, Z.; Li, L.; Zhang, J.; Zhou, H.; Sun, L.-D.; Yan, C.-H. Zwitterions Narrow Distribution of Perovskite Quantum Wells for Blue Light-Emitting Diodes with Efficiency Exceeding 15%. *Adv. Mater.* **2023**, *35* (3), 2208078.
(163) LaMer, V. K.; Dinegar, R. H. Theory, Production and Mechanism of Formation of Monodispersed Hydrosols. *J. Am. Chem. Soc.* **1950**, *72* (11), 4847−4854.
(164) Zheng, D.; Raffin, F.; Volovitch, P.; Pauporté, T. Control of Perovskite Film Crystallization and Growth Direction to Target Homogeneous Monolithic Structures. *Nat. Commun.* **2022**, *13* (1), 6655.
(165) Yang, Y.; Wu, J.; Wang, X.; Guo, Q.; Liu, X.; Sun, W.; Wei, Y.; Huang, Y.; Lan, Z.; Huang, M.; Lin, J.; Chen, H.; Wei, Z. Suppressing Vacancy Defects and Grain Boundaries via Ostwald Ripening for High-Performance and Stable Perovskite Solar Cells. *Adv. Mater.* **2020**, *32* (7), 1904347.
(166) Huang, X.; Wu, B.; Zheng, N. Optimizing Solvent Chemistry for High-Quality Halide Perovskite Films. *Acc. Mater. Res.* **2025**, *6* (1), 40−51.
(167) Han, D.; Imran, M.; Zhang, M.; Chang, S.; Wu, X.; Zhang, X.; Tang, J.; Wang, M.; Ali, S.; Li, X.; Yu, G.; Han, J.; Wang, L.; Zou, B.;

Downloaded from pubs.acs.org/chreav/article-pdf/doi/10.1021/acs.chemrev.6c00202/6880579/acs.chemrev.6c00202.pdf by guest on 10 October 2026

Zhong, H. Efficient Light-Emitting Diodes Based on in Situ Fabricated FAPbBr3 Nanocrystals: The Enhancing Role of the Ligand-Assisted Reprecipitation Process. *ACS Nano* **2018**, *12* (8), 8808−8816.
(168) Wu, C.; Zou, Y.; Wu, T.; Ban, M.; Pecunia, V.; Han, Y.; Liu, Q.; Song, T.; Duhm, S.; Sun, B. Improved Performance and Stability of All-Inorganic Perovskite Light-Emitting Diodes by Anti-solvent Vapor Treatment. *Adv. Funct. Mater.* **2017**, *27* (28), 1700338.
(169) Ngo, T. T.; Suarez, I.; Antonicelli, G.; Cortizo-Lacalle, D.; Martinez-Pastor, J. P.; Mateo-Alonso, A.; Mora-Sero, I. Enhancement of the Performance of Perovskite Solar Cells, LEDs, and Optical Amplifiers by Anti-Solvent Additive Deposition. *Adv. Mater.* **2017**, *29* (7), 1604056.
(170) Ghosh, S.; Mishra, S.; Singh, T. Anti-solvents in Perovskite Solar Cells: Importance, Issues, and Alternatives. *Adv. Mater. Interfaces* **2020**, *7* (18), 2000950.
(171) Cao, X.; Zhi, L.; Li, Y.; Fang, F.; Cui, X.; Ci, L.; Ding, K.; Wei, J. Fabrication of Perovskite Films with Large Columnar Grains via Solvent-Mediated Ostwald Ripening for Efficient Inverted Perovskite Solar Cells. *ACS Appl. Energy Mater.* **2018**, *1* (2), 868−875.
(172) Xue, J.; Wang, R.; Wang, K.-L.; Wang, Z.-K.; Yavuz, I.; Wang, Y.; Yang, Y.; Gao, X.; Huang, T.; Nuryyeva, S.; Lee, J.-W.; Duan, Y.; Liao, L.-S.; Kaner, R.; Yang, Y. Crystalline Liquid-like Behavior: Surface-Induced Secondary Grain Growth of Photovoltaic Perovskite Thin Film. *J. Am. Chem. Soc.* **2019**, *141* (35), 13948−13953.
(173) Sun, J.; Li, F.; Yuan, J.; Ma, W. Advances in Metal Halide Perovskite Film Preparation: The Role of Anti-Solvent Treatment. *Small Methods* **2021**, *5* (5), 2100046.
(174) Cho, H.; Kim, J. S.; Wolf, C.; Kim, Y.-H.; Yun, H. J.; Jeong, S.-H.; Sadhanala, A.; Venugopalan, V.; Choi, J. W.; Lee, C.-L.; Friend, R. H.; Lee, T.-W. High-Efficiency Polycrystalline Perovskite Light-Emitting Diodes Based on Mixed Cations. *ACS Nano* **2018**, *12* (3), 2883−2892.
(175) Yantara, N.; Bhaumik, S.; Yan, F.; Sabba, D.; Dewi, H. A.; Mathews, N.; Boix, P. P.; Demir, H. V.; Mhaisalkar, S. Inorganic Halide Perovskites for Efficient Light-Emitting Diodes. *J. Phys. Chem. Lett.* **2015**, *6* (21), 4360−4364.
(176) Kim, B. W.; Im, S. H. Supersaturated Anti-solvent-Assisted Crystallization for Highly Efficient Inorganic Perovskite Light-Emitting Diodes. *ACS Nano* **2024**, *18* (42), 28691−28699.
(177) Taylor, A. D.; Sun, Q.; Goetz, K. P.; An, Q.; Schramm, T.; Hofstetter, Y.; Litterst, M.; Paulus, F.; Vaynzof, Y. A General Approach to High-Efficiency Perovskite Solar Cells by Any Anti-solvent. *Nat. Commun.* **2021**, *12* (1), 1878.
(178) Chu, Z.; Ye, Q.; Zhao, Y.; Ma, F.; Yin, Z.; Zhang, X.; You, J. Perovskite Light-Emitting Diodes with External Quantum Efficiency Exceeding 22% via Small-Molecule Passivation. *Adv. Mater.* **2021**, *33* (18), 2007169.
(179) Yu, J. C.; Kim, D. B.; Jung, E. D.; Lee, B. R.; Song, M. H. High-Performance Perovskite Light-Emitting Diodes via Morphological Control of Perovskite Films. *Nanoscale* **2016**, *8* (13), 7036−7042.
(180) Chen, C.; Han, T.-H.; Tan, S.; Xue, J.; Zhao, Y.; Liu, Y.; Wang, H.; Hu, W.; Bao, C.; Mazzeo, M.; Wang, R.; Duan, Y.; Yang, Y. Efficient Flexible Inorganic Perovskite Light-Emitting Diodes Fabricated with CsPbBr3 Emitters Prepared via Low-Temperature in Situ Dynamic Thermal Crystallization. *Nano Lett.* **2020**, *20* (6), 4673−4680.
(181) Kumawat, N. K.; Jain, N.; Dey, A.; Narasimhan, K. L.; Kabra, D. Quantitative Correlation of Perovskite Film Morphology to Light Emitting Diodes Efficiency Parameters. *Adv. Funct. Mater.* **2017**, *27* (3), 1603219.
(182) Xia, Y.; Li, J.-C.; Zhang, Z.; Li, N.; Wang, Y.; Li, Y.-H.; Wang, K.-L.; Chen, C.-H.; Chen, J.; Huang, L.; Yang, Y.-T.; Xing, G.; Sun, B.; Wang, Z.-K. Spatial Crystallization Homogenization Boosts Scalable Perovskite Light-Emitting Diodes. *Adv. Mater.* **2025**, *37* (42), No. e06413.
(183) Bush, K. A.; Rolston, N.; Gold-Parker, A.; Manzoor, S.; Hausele, J.; Yu, Z. J.; Raiford, J. A.; Cheacharoen, R.; Holman, Z. C.; Toney, M. F.; Dauskardt, R. H.; McGehee, M. D. Controlling Thin-Film Stress and Wrinkling during Perovskite Film Formation. *ACS Energy Lett.* **2018**, *3* (6), 1225−1232.
(184) Yu, J. C.; Kim, D. W.; Kim, D. B.; Jung, E. D.; Lee, K.-S.; Lee, S.; Nuzzo, D. Di; Kim, J.-S.; Song, M. H. Effect of the Solvent Used for Fabrication of Perovskite Films by Solvent Dropping on Performance of Perovskite Light-Emitting Diodes. *Nanoscale* **2017**, *9* (5), 2088−2094.
(185) Bischak, C. G.; Sanehira, E. M.; Precht, J. T.; Luther, J. M.; Ginsberg, N. S. Heterogeneous Charge Carrier Dynamics in Organic-Inorganic Hybrid Materials: Nanoscale Lateral and Depth-Dependent Variation of Recombination Rates in Methylammonium Lead Halide Perovskite Thin Films. *Nano Lett.* **2015**, *15* (7), 4799−4807.
(186) Liang, A.; Wang, K.; Gao, Y.; Finkenauer, B. P.; Zhu, C.; Jin, L.; Huang, L.; Dou, L. Highly Efficient Halide Perovskite Light-Emitting Diodes via Molecular Passivation. *Angew. Chem., Int. Ed.* **2021**, *60* (15), 8337−8343.
(187) Uličná, S.; Dou, B.; Kim, D. H.; Zhu, K.; Walls, J. M.; Bowers, J. W.; van Hest, M. F. A. M. Scalable Deposition of High-Efficiency Perovskite Solar Cells by Spray-Coating. *ACS Appl. Energy Mater.* **2018**, *1* (5), 1853−1857.
(188) Shi, Y.; Wu, W.; Dong, H.; Li, G.; Xi, K.; Divitini, G.; Ran, C.; Yuan, F.; Zhang, M.; Jiao, B.; Hou, X.; Wu, Z. A Strategy for Architecture Design of Crystalline Perovskite Light-Emitting Diodes with High Performance. *Adv. Mater.* **2018**, *30* (25), 1800251.
(189) Chen, Y.; He, M.; Peng, J.; Sun, Y.; Liang, Z. Structure and Growth Control of Organic-Inorganic Halide Perovskites for Optoelectronics: From Polycrystalline Films to Single Crystals. *Adv. Sci.* **2016**, *3* (4), 1500392.
(190) Lee, J.-W.; Choi, Y. J.; Yang, J.-M.; Ham, S.; Jeon, S. K.; Lee, J. Y.; Song, Y.-H.; Ji, E. K.; Yoon, D.-H.; Seo, S.; Shin, H.; Han, G. S.; Jung, H. S.; Kim, D.; Park, N.-G. In-Situ Formed Type I Nanocrystalline Perovskite Film for Highly Efficient Light-Emitting Diode. *ACS Nano* **2017**, *11* (3), 3311−3319.
(191) Lohmann, K. B.; Patel, J. B.; Rothmann, M. U.; Xia, C. Q.; Oliver, R. D. J.; Herz, L. M.; Snaith, H. J.; Johnston, M. B. Control over Crystal Size in Vapor Deposited Metal-Halide Perovskite Films. *ACS Energy Lett.* **2020**, *5* (3), 710−717.
(192) Ye, J.; Byranvand, M. M.; Martínez, C. O.; Hoye, R. L. Z.; Saliba, M.; Polavarapu, L. Defect Passivation in Lead-Halide Perovskite Nanocrystals and Thin Films: Toward Efficient LEDs and Solar Cells. *Angew. Chem., Int. Ed.* **2021**, *60* (40), 21636−21660.
(193) Jia, Y.-H.; Neutzner, S.; Zhou, Y.; Yang, M.; Tapia, J. M. F.; Li, N.; Yu, H.; Cao, J.; Wang, J.-P.; Petrozza, A.; Wong, C.-P.; Zhao, N. Role of Excess FAI in Formation of High-Efficiency FAPbI3-Based Light-Emitting Diodes. *Adv. Funct. Mater.* **2020**, *30* (1), 1906875.
(194) Han, T.-H.; Tan, S.; Xue, J.; Meng, L.; Lee, J.-W.; Yang, Y. Interface and Defect Engineering for Metal Halide Perovskite Optoelectronic Devices. *Adv. Mater.* **2019**, *31* (47), 1803515.
(195) Wei, J.; Li, J.; Duan, C.; Yuan, L.; Zou, S.; Pang, Q.; Yan, K. High Efficiency Near-Infrared Perovskite Light Emitting Diodes With Reduced Rolling-Off by Surface Post-Treatment. *Small* **2023**, *19* (20), 2207769.
(196) Iskandar, J.; Lee, C.-C.; Kurniawan, A.; Cheng, H.-M.; Liu, S.-W.; Biring, S. Improving the Efficiency of Near-IR Perovskite LEDs via Surface Passivation and Ultrathin Interfacial Layers. *Cell Rep. Phys. Sci.* **2022**, *3* (12), 101170.
(197) Liu, A.; Zhang, Z.; Li, J.; Yu, H.; Wang, N.; Wang, J.; Zhao, N. Optimizing Perovskite Surfaces to Enhance Post-Treatment for Efficient Blue Mixed-Halide Perovskite Light-Emitting Diodes. *Adv. Mater.* **2025**, *37* (25), 2414788.
(198) Yuan, M.; Ma, H.; Dong, Q.; Wang, X.; Zhang, L.; Yin, Y.; Ying, Z.; Guo, J.; Shang, W.; Zhang, J.; Shi, Y. Chemical Polishing and Sub-Surface Passivation of Perovskite Film towards High Efficiency Solar Cells. *Nano Energy* **2024**, *121*, 109192.
(199) Chi, S.; Chen, Y.; Li, X.; Wang, J.; Zhao, Z.; Li, Z.; Miao, Y.; Tong, X.; Liu, J.; Bi, Y.; Liu, Z.; Wang, Z.; Yang, W.; Lin, K. Functional Molecule Surface Infiltration Treatment for Efficient All-Inorganic Perovskite Light-Emitting Diodes. *Chem. Eng. J.* **2025**, *514*, 162787.
(200) Lee, S.; Kim, D. B.; Yu, J. C.; Jang, C. H.; Park, J. H.; Lee, B. R.; Song, M. H. Versatile Defect Passivation Methods for Metal Halide Perovskite Materials and Their Application to Light-Emitting Devices. *Adv. Mater.* **2019**, *31* (20), 1805244.

Downloaded from pubs.acs.org/chreav/article-pdf/doi/10.1021/acs.chemrev.6c00202/68805793/acs.chemrev.6c00202.pdf by guest on 10 October 2026

(201) Tan, S.; Huang, T.; Yavuz, I.; Wang, R.; Weber, M. H.; Zhao, Y.; Abdelsamie, M.; Liao, M. E.; Wang, H.-C.; Huynh, K.; Wei, K.-H.; Xue, J.; Babbe, F.; Goorsky, M. S.; Lee, J.-W.; Sutter-Fella, C. M.; Yang, Y. Surface Reconstruction of Halide Perovskites During Post-Treatment. *J. Am. Chem. Soc.* **2021**, *143* (18), 6781−6786.
(202) Li, M.; Zhao, Y.; Qin, X.; Ma, Q.; Lu, J.; Lin, K.; Xu, P.; Li, Y.; Feng, W.; Zhang, W.-H.; Wei, Z. Conductive Phosphine Oxide Passivator Enables Efficient Perovskite Light-Emitting Diodes. *Nano Lett.* **2022**, *22* (6), 2490−2496.
(203) Shen, X.; Kang, K.; Yu, Z.; Jeong, W. H.; Choi, H.; Park, S. H.; Stranks, S. D.; Snaith, H. J.; Friend, R. H.; Lee, B. R. Passivation Strategies for Mitigating Defect Challenges in Halide Perovskite Light-Emitting Diodes. *Joule* **2023**, *7* (2), 272−308.
(204) Kim, Y. C.; An, H. J.; Kim, D. H.; Myoung, J.-M.; Heo, Y. J.; Cho, J. H. High-Performance Perovskite-Based Blue Light-Emitting Diodes with Operational Stability by Using Organic Ammonium Cations as Passivating Agents. *Adv. Funct. Mater.* **2021**, *31* (5), 2005553.
(205) Song, J.; Li, J.; Xu, L.; Li, J.; Zhang, F.; Han, B.; Shan, Q.; Zeng, H. Room-Temperature Triple-Ligand Surface Engineering Synergistically Boosts Ink Stability, Recombination Dynamics, and Charge Injection toward EQE-11.6% Perovskite QLEDs. *Adv. Mater.* **2018**, *30* (30), 1800764.
(206) Li, Z.; Ren, Z.; Liang, Q.; Fong, P. W. K.; Tian, J.; Li, G. Eliminating the Adverse Impact of Composition Modulation in Perovskite Light-Emitting Diodes toward Ultra-High Brightness and Stability. *Adv. Mater.* **2024**, *36* (27), 2313981.
(207) Kong, L.; Zhang, X.; Zhang, C.; Wang, L.; Wang, S.; Cao, F.; Zhao, D.; Rogach, A. L.; Yang, X. Stability of Perovskite Light-Emitting Diodes: Existing Issues and Mitigation Strategies Related to Both Material and Device Aspects. *Adv. Mater.* **2022**, *34* (43), 2205217.
(208) Cheng, H.; Feng, Y.; Fu, Y.; Zheng, Y.; Shao, Y.; Bai, Y. Understanding and Minimizing Non-Radiative Recombination Losses in Perovskite Light-Emitting Diodes. *J. Mater. Chem. C* **2022**, *10* (37), 13590−13610.
(209) Yu, M.; Qin, T.; Gao, G.; Zu, K.; Zhang, D.; Chen, N.; Wang, D.; Hua, Y.; Zhang, H.; Zhao, Y.-B.; Zhu, J. Multiple Defects Renovation and Phase Reconstruction of Reduced-Dimensional Perovskites via in Situ Chlorination for Efficient Deep-Blue (454 nm) Light-Emitting Diodes. *Light Sci. Appl.* **2025**, *14* (1), 102.
(210) Byranvand, M. M.; Saliba, M. Defect Passivation of Perovskite Films for Highly Efficient and Stable Solar Cells. *Solar RRL* **2021**, *5* (8), 2100295.
(211) Kang, D.-H.; Kim, S.-Y.; Lee, J.-W.; Park, N.-G. Efficient Surface Passivation of Perovskite Films by a Post-Treatment Method with a Minimal Dose. *J. Mater. Chem. A* **2021**, *9* (6), 3441−3450.
(212) Fang, Z.; Chen, W.; Shi, Y.; Zhao, J.; Chu, S.; Zhang, J.; Xiao, Z. Dual Passivation of Perovskite Defects for Light-Emitting Diodes with External Quantum Efficiency Exceeding 20%. *Adv. Funct. Mater.* **2020**, *30* (12), 1909754.
(213) Zhang, F.; Min, H.; Zhang, Y.; Kuang, Z.; Wang, J.; Feng, Z.; Wen, K.; Xu, L.; Yang, C.; Shi, H.; Zhuo, C.; Wang, N.; Chang, J.; Huang, W.; Wang, J. Vapor-Assisted In Situ Recrystallization for Efficient Tin-Based Perovskite Light-Emitting Diodes. *Adv. Mater.* **2022**, *34* (37), 2203180.
(214) Xie, M.; Guo, J.; Bi, C.; Zhang, Y.; Li, H.; Zhang, L.; Zhang, L.; Zhang, X.; Zheng, W.; Tian, J. Efficient and Stable Pure-Red Perovskite LED Based on Uniform Arrangement Strongly Confined Quantum-Dot Film. *ACS Energy Lett.* **2024**, *9* (8), 4003−4008.
(215) Jiang, J.; Shi, M.; Xia, Z.; Cheng, Y.; Chu, Z.; Zhang, W.; Li, J.; Yin, Z.; You, J.; Zhang, X. Efficient Pure-Red Perovskite Light-Emitting Diodes with Strong Passivation via Ultrasmall-Sized Molecules. *Sci. Adv.* **2024**, *10* (18), No. eadn5683.
(216) Wang, L.; Liu, B.; Zhao, X.; Demir, H. V.; Gu, H.; Sun, H. Solvent-Assisted Surface Engineering for High-Performance All-Inorganic Perovskite Nanocrystal Light-Emitting Diodes. *ACS Appl. Mater. Interfaces* **2018**, *10* (23), 19828−19835.
(217) Chen, P.; Xiong, Z.; Wu, X.; Shao, M.; Ma, X.; Xiong, Z.; Gao, C. Highly Efficient Perovskite Light-Emitting Diodes Incorporating Full Film Coverage and Bipolar Charge Injection. *J. Phys. Chem. Lett.* **2017**, *8* (8), 1810−1818.
(218) Jiao, H.; Ni, Z.; Shi, Z.; Fei, C.; Liu, Y.; Dai, X.; Huang, J. Perovskite Grain Wrapping by Converting Interfaces and Grain Boundaries into Robust and Water-Insoluble Low-Dimensional Perovskites. *Sci. Adv.* **2022**, *8* (48), No. eabq4524.
(219) Liu, B.; Wang, L.; Gu, H.; Sun, H.; Demir, H. V. Highly Efficient Green Light-Emitting Diodes from All-Inorganic Perovskite Nanocrystals Enabled by a New Electron Transport Layer. *Adv. Opt. Mater.* **2018**, *6* (11), 1800220.
(220) Yuan, S.; Fang, T.; Huang, J.; Li, X.; Wei, C.; Zhou, Y.; Li, Y.; Zheng, X.; Huang, J.; Su, J.; Baryshnikov, G.; Choy, W. C. H.; Zeng, H.; Xu, B. Balancing Charge Injection via a Tailor-Made Electron-Transporting Material for High Performance Blue Perovskite QLEDs. *ACS Energy Lett.* **2023**, *8* (1), 818−826.
(221) Papavassiliou, G. C. Three- and Low-Dimensional Inorganic Semiconductors. *Prog. Solid State Chem.* **1997**, *25* (3), 125−270.
(222) Yuan, M.; Quan, L. N.; Comin, R.; Walters, G.; Sabatini, R.; Voznyy, O.; Hoogland, S.; Zhao, Y.; Beauregard, E. M.; Kanjanaboos, P.; Lu, Z.; Kim, D. H.; Sargent, E. H. Perovskite Energy Funnels for Efficient Light-Emitting Diodes. *Nat. Nanotechnol.* **2016**, *11* (10), 872−877.
(223) Quan, L. N.; Yuan, M.; Comin, R.; Voznyy, O.; Beauregard, E. M.; Hoogland, S.; Buin, A.; Kirmani, A. R.; Zhao, K.; Amassian, A.; Kim, D. H.; Sargent, E. H. Ligand-Stabilized Reduced-Dimensionality Perovskites. *J. Am. Chem. Soc.* **2016**, *138* (8), 2649−2655.
(224) Blancon, J.-C.; Stier, A. V.; Tsai, H.; Nie, W.; Stoumpos, C. C.; Traoré, B.; Pedesseau, L.; Kepenekian, M.; Katsutani, F.; Noe, G. T.; Kono, J.; Tretiak, S.; Crooker, S. A.; Katan, C.; Kanatzidis, M. G.; Crochet, J. J.; Even, J.; Mohite, A. D. Scaling Law for Excitons in 2D Perovskite Quantum Wells. *Nat. Commun.* **2018**, *9* (1), 2254.
(225) Xing, J.; Zhao, Y.; Askerka, M.; Quan, L. N.; Gong, X.; Zhao, W.; Zhao, J.; Tan, H.; Long, G.; Gao, L.; Yang, Z.; Voznyy, O.; Tang, J.; Lu, Z.-H.; Xiong, Q.; Sargent, E. H. Color-Stable Highly Luminescent Sky-Blue Perovskite Light-Emitting Diodes. *Nat. Commun.* **2018**, *9* (1), 3541.
(226) Peng, S.; Liu, J.; Liang, C.; Chen, G.; Shi, Y.; Miao, Z.; Liang, W.; Zhang, T.; Xie, Y.; Zhang, Y.; Song, Y.; Li, P. Achieving Low-n Value Phases and Unobstructed Carrier Transport toward High-Performance Quasi-2D Perovskite Solar Cells and Modules. *Joule* **2025**, *9* (9), 102079.
(227) Yan, L.; Ma, J.; Li, P.; Zang, S.; Han, L.; Zhang, Y.; Song, Y. Charge-Carrier Transport in Quasi-2D Ruddlesden-Popper Perovskite Solar Cells. *Adv. Mater.* **2022**, *34* (7), 2106822.
(228) Zhang, L.; Sun, C.; He, T.; Jiang, Y.; Wei, J.; Huang, Y.; Yuan, M. High-Performance Quasi-2D Perovskite Light-Emitting Diodes: From Materials to Devices. *Light Sci. Appl.* **2021**, *10* (1), 61.
(229) Wang, K.; Lin, Z.-Y.; Zhang, Z.; Jin, L.; Ma, K.; Coffey, A. H.; Atapattu, H. R.; Gao, Y.; Park, J. Y.; Wei, Z.; Finkenauer, B. P.; Zhu, C.; Meng, X.; Chowdhury, S. N.; Chen, Z.; Terlier, T.; Do, T.-H.; Yao, Y.; Graham, K. R.; Boltasseva, A.; Guo, T.-F.; Huang, L.; Gao, H.; Savoie, B. M.; Dou, L. Suppressing Phase Disproportionation in Quasi-2D Perovskite Light-Emitting Diodes. *Nat. Commun.* **2023**, *14* (1), 397.
(230) Zhang, Y.; Sun, M.; Zhou, N.; Huang, B.; Zhou, H. Electronic Tunability and Mobility Anisotropy of Quasi-2D Perovskite Single Crystals with Varied Spacer Cations. *J. Phys. Chem. Lett.* **2020**, *11* (18), 7610−7616.
(231) Tsai, H.; Asadpour, R.; Blancon, J.-C.; Stoumpos, C. C.; Even, J.; Ajayan, P. M.; Kanatzidis, M. G.; Alam, M. A.; Mohite, A. D.; Nie, W. Design Principles for Electronic Charge Transport in Solution-Processed Vertically Stacked 2D Perovskite Quantum Wells. *Nat. Commun.* **2018**, *9* (1), 2130.
(232) Kober-Czerny, M.; Motti, S. G.; Holzhey, P.; Wenger, B.; Lim, J.; Herz, L. M.; Snaith, H. J. Excellent Long-Range Charge-Carrier Mobility in 2D Perovskites. *Adv. Funct. Mater.* **2022**, *32* (36), 2203064.
(233) Stoumpos, C. C.; Cao, D. H.; Clark, D. J.; Young, J.; Rondinelli, J. M.; Jang, J. I.; Hupp, J. T.; Kanatzidis, M. G. Ruddlesden-Popper Hybrid Lead Iodide Perovskite 2D Homologous Semiconductors. *Chem. Mater.* **2016**, *28* (8), 2852−2867.

Downloaded from pubs.acs.org/chreav/article-pdf/doi/10.1021/acs.chemrev.6c00202/68805793/acs.chemrev.6c00202.pdf by guest on 10 October 2026

(234) Proppe, A. H.; Elkins, M. H.; Voznyy, O.; Pensack, R. D.; Zapata, F.; Besteiro, L. V.; Quan, L. N.; Quintero-Bermudez, R.; Todorovic, P.; Kelley, S. O.; Govorov, A. O.; Gray, S. K.; Infante, I.; Sargent, E. H.; Scholes, G. D. Spectrally Resolved Ultrafast Exciton Transfer in Mixed Perovskite Quantum Wells. *J. Phys. Chem. Lett.* **2019**, *10* (3), 419−426.
(235) Lei, L.; Seyitliyev, D.; Stuard, S.; Mendes, J.; Dong, Q.; Fu, X.; Chen, Y.-A.; He, S.; Yi, X.; Zhu, L.; Chang, C.-H.; Ade, H.; Gundogdu, K.; So, F. Efficient Energy Funneling in Quasi-2D Perovskites: From Light Emission to Lasing. *Adv. Mater.* **2020**, *32* (16), 1906571.
(236) Proppe, A. H.; Quintero-Bermudez, R.; Tan, H.; Voznyy, O.; Kelley, S. O.; Sargent, E. H. Synthetic Control over Quantum Well Width Distribution and Carrier Migration in Low-Dimensional Perovskite Photovoltaics. *J. Am. Chem. Soc.* **2018**, *140* (8), 2890−2896.
(237) Amoroso, D.; Nasti, G.; Sutter-Fella, C. M.; Villone, M. M.; Maffettone, P. L.; Abate, A. The Central Role of Colloids to Explain the Crystallization Dynamics of Halide Perovskites: A Critical Review. *Matter* **2024**, *7* (7), 2399−2430.
(238) He, T.; Li, S.; Jiang, Y.; Qin, C.; Cui, M.; Qiao, L.; Xu, H.; Yang, J.; Long, R.; Wang, H.; Yuan, M. Reduced-Dimensional Perovskite Photovoltaics with Homogeneous Energy Landscape. *Nat. Commun.* **2020**, *11* (1), 1672.
(239) Bai, Y.; Huang, Z.; Zhang, X.; Lu, J.; Niu, X.; He, Z.; Zhu, C.; Xiao, M.; Song, Q.; Wei, X.; Wang, C.; Cui, Z.; Dou, J.; Chen, Y.; Pei, F.; Zai, H.; Wang, W.; Song, T.; An, P.; Zhang, J.; Dong, J.; Li, Y.; Shi, J.; Jin, H.; Chen, P.; Sun, Y.; Li, Y.; Chen, H.; Wei, Z.; Zhou, H.; Chen, Q. Initializing Film Homogeneity to Retard Phase Segregation for Stable Perovskite Solar Cells. *Science* **2022**, *378* (6621), 747−754.
(240) Guo, Z.; Liang, Y.; Ni, D.; Li, L.; Liu, S.; Zhang, Y.; Chen, Q.; Zhang, Q.; Wang, Q.; Zhou, H. Homogeneous Phase Distribution in Q-2D Perovskites via Co-Assembly of Spacer Cations for Efficient Light-Emitting Diodes. *Adv. Mater.* **2023**, *35* (38), 2302711.
(241) Feng, S.-C.; Hu, X.-M.; Shen, Y.; Li, Y.-Q.; Tang, J.-X.; Lee, S.-T. Phase Regulation of Layered Perovskites toward High-Performance Light-Emitting Diodes. *Adv. Funct. Mater.* **2025**, *35* (21), 2310220.
(242) Kong, L.; Zhang, X.; Li, Y.; Wang, H.; Jiang, Y.; Wang, S.; You, M.; Zhang, C.; Zhang, T.; Kershaw, S. V.; Zheng, W.; Yang, Y.; Lin, Q.; Yuan, M.; Rogach, A. L.; Yang, X. Smoothing the Energy Transfer Pathway in Quasi-2D Perovskite Films Using Methanesulfonate Leads to Highly Efficient Light-Emitting Devices. *Nat. Commun.* **2021**, *12* (1), 1246.
(243) He, B.; Liu, T.; Wang, C.; Wen, Z.; Sun, B.; Wen, W.; Xing, G.; Gao, X.; Chen, S. Improving Crystallinity and Out-of-Plane Orientation in Quasi-2D Ruddlesden-Popper Perovskite by Fluorinated Organic Salt for Light-Emitting Diodes. *Small* **2023**, *19* (49), 2303255.
(244) Yuan, S.; Fang, T.; Han, B.; Shan, Q.; Wei, C.; Zheng, X.; Li, X.; Xu, B.; Zeng, H. Ordered Phase Distribution of Quasi-2D Perovskites Controlled by a Supramolecular Approach Enables Efficient Blue Light-Emitting Diodes. *Adv. Funct. Mater.* **2024**, *34* (25), 2316206.
(245) He, H.; Zhao, D.; Yin, J.; Xing, Y.; Tian, P.; Mei, S.; Zhang, W.; Guo, R. Enhancing Quasi-2D Perovskite Blue Light-Emitting Diodes via a Bifunctional Small-Molecule Agent. *Mater. Today Energy* **2025**, *52*, 101926.
(246) Li, Z.; Wei, Q.; Wang, Y.; Tao, C.; Zou, Y.; Liu, X.; Li, Z.; Wu, Z.; Li, M.; Guo, W.; Li, G.; Xu, W.; Gao, F. Highly Bright Perovskite Light-Emitting Diodes Enabled by Retarded Auger Recombination. *Nat. Commun.* **2025**, *16* (1), 927.
(247) McMeekin, D. P.; Wang, Z.; Rehman, W.; Pulvirenti, F.; Patel, J. B.; Noel, N. K.; Johnston, M. B.; Marder, S. R.; Herz, L. M.; Snaith, H. J. Crystallization Kinetics and Morphology Control of Formamidinium-Cesium Mixed-Cation Lead Mixed-Halide Perovskite via Tunability of the Colloidal Precursor Solution. *Adv. Mater.* **2017**, *29* (29), 1607039.
(248) Peng, S.; Miao, Z.; Liang, Y.; Zhao, R.; Yuan, F.; Zhu, H.; Liang, W.; Shi, Y.; Li, P.; Zhang, Y.; Song, Y. Governing the Dispersion of Quasi-2D Perovskite Phases toward Efficient and Stable Perovskite Solar Cells. *Matter* **2024**, *7* (10), 3500−3517.
(249) Hu, X.-M.; Shen, Y.; Feng, S.-C.; Su, Z.-H.; Zhang, K.; Cao, L.-X.; Wang, B.-F.; Gao, X.; Tang, J.-X.; Li, Y.-Q. Unveiling the Role of Additive Molecular Characteristics in Regulating Chlorine Loss and Phase Distribution for Blue Perovskite Light-Emitting Diodes. *Adv. Funct. Mater.* **2024**, *34* (51), 2410143.
(250) Sheng, T.; Mao, Y.; Guo, J.; Wu, G.; Xia, J.; Zhang, Z.; Wang, B.; Li, S.; Pang, P.; Zeng, M.; Hong, W.; Yu, D.; Xing, G. Unveiling Additive-Driven Crystallization-Kinetics Control for Efficient Ultra-pure Red Perovskite Light Emitting Diodes. *Chem. Eng. J.* **2025**, *504*, 158817.
(251) Kuang, Y.; Xue, Y.; Zhang, Z.; Yang, L.; Bie, T.; Li, R.; Liang, W.; Zhou, N.; Shao, M. Strategic Regulation of Crystallization Kinetics to Achieve Efficient Pure-Red Quasi-2D Perovskite Light-Emitting Diodes. *Chem. Eng. J.* **2025**, *507*, 160278.
(252) Munir, R.; Sheikh, A. D.; Abdelsamie, M.; Hu, H.; Yu, L.; Zhao, K.; Kim, T.; Tall, O. El; Li, R.; Smilgies, D.-M.; Amassian, A. Hybrid Perovskite Thin-Film Photovoltaics: In Situ Diagnostics and Importance of the Precursor Solvate Phases. *Adv. Mater.* **2017**, *29* (2), 1604113.
(253) Jang, G.; Ma, S.; Kwon, H.-C.; Goh, S.; Ban, H.; Kim, J. S.; Kim, J.-H.; Moon, J. Elucidation of the Formation Mechanism of Highly Oriented Multiphase Ruddlesden-Popper Perovskite Solar Cells. *ACS Energy Lett.* **2021**, *6* (1), 249−260.
(254) de Gennes, P. G. Solvent Evaporation of Spin Cast Films: "Crust" Effects. *Eur. Phys. J. E* **2002**, *7* (1), 31−34.
(255) Yan, Y.; Yang, Y.; Liang, M.; Abdellah, M.; Pullerits, T.; Zheng, K.; Liang, Z. Implementing an Intermittent Spin-Coating Strategy to Enable Bottom-up Crystallization in Layered Halide Perovskites. *Nat. Commun.* **2021**, *12* (1), 6603.
(256) Chen, A. Z.; Shiu, M.; Ma, J. H.; Alpert, M. R.; Zhang, D.; Foley, B. J.; Smilgies, D.-M.; Lee, S.-H.; Choi, J. J. Origin of Vertical Orientation in Two-Dimensional Metal Halide Perovskites and Its Effect on Photovoltaic Performance. *Nat. Commun.* **2018**, *9* (1), 1336.
(257) Nah, Y.; Solanki, D.; Dong, Y.; Röhr, J. A.; Taylor, A. D.; Hu, S.; Sargent, E. H.; Kim, D. H. Narrowing the Phase Distribution of Quasi-2D Perovskites for Stable Deep-Blue Electroluminescence. *Adv. Sci.* **2022**, *9* (24), 2201807.
(258) He, S.; Yuan, F.; Zhu, P.; Ali, F.; Tang, H.; Zhang, S.; Wu, P.; Deng, W.; Dong, H.; Wu, Z. Divergent Optoelectronic Tuning in Sky-Blue Quasi-2D Perovskites via Spacers Conjugation and Fluorination. *Adv. Funct. Mater.* **2026**, *36* (26), No. e23282.
(259) Bao, Z.; Yu, S.; Guo, X.; Wang, Y.; Lv, Y.; Zou, D.; Song, L.; Liu, X. Regulating the Continuous and Concentrated Distribution of Quasi-2D Perovskite Phases to Achieve Sky-Blue Light-Emitting Diodes with Efficiency Approaching 17%. *Chem. Eng. J.* **2024**, *482*, 148875.
(260) Sun, C.; Jiang, Y.; Cui, M.; Qiao, L.; Wei, J.; Huang, Y.; Zhang, L.; He, T.; Li, S.; Hsu, H.-Y.; Qin, C.; Long, R.; Yuan, M. High-Performance Large-Area Quasi-2D Perovskite Light-Emitting Diodes. *Nat. Commun.* **2021**, *12* (1), 2207.
(261) Wang, C.; Han, D.; Wang, J.; Yang, Y.; Liu, X.; Huang, S.; Zhang, X.; Chang, S.; Wu, K.; Zhong, H. Dimension Control of in Situ Fabricated CsPbClBr2 Nanocrystal Films toward Efficient Blue Light-Emitting Diodes. *Nat. Commun.* **2020**, *11* (1), 6428.
(262) Xiu, Y.; Liu, Y.; Niu, K.; Cui, J.; Qi, Y.; Lin, C.; Chen, D.; Li, Y.; He, H.; Ye, Z.; Jin, Y. Solvent-Vapor Atmosphere Controls the in Situ Crystallization of Perovskites. *ACS Mater. Lett.* **2021**, *3* (8), 1172−1180.
(263) Park, S.; Kim, J.; Kim, G.-M.; Park, J.; Lee, S.; Lee, D. C.; Kim, N.; Cho, B.-G.; Shin, B. Controlling the Phase Distribution of Single Bromide Quasi-2-Dimensional Perovskite Crystals via Solvent Engineering for Pure-Blue Light-Emitting Diodes. *ACS Appl. Mater. Interfaces* **2024**, *16* (29), 38395−38403.
(264) Yu, A.; Wang, J.; Huo, Y.; Wang, S.; Zhang, X.; He, T.; Yang, S.; Jiang, Y.; Zhang, L.; Liu, Z.; Yuan, M.; Sun, C. Promoting Phase Transition in Quasi-2D Perovskites For High-Performance Pure-Red LEDs. *Adv. Mater.* **2025**, *37* (28), 2503704.
(265) Zhuang, L.; Wei, Q.; Li, C.; Ren, H.; Li, Y.; Shi, F.; Zhai, L.; Leng, K.; Li, M.; Lau, S. P. Efficient Light-Emitting Diodes via Hydrogen Bonding Induced Phase Modulation in Quasi-2D Perovskites. *Adv. Opt. Mater.* **2022**, *10* (21), 2201180.
(266) Guo, Y.; Tang, Z.; Li, Z.; Wang, Q.; Fu, Y.; Xie, Z. Efficient Perovskite Light-Emitting Diodes Processed with Green Solvents

Downloaded from pubs.acs.org/chreav/article-pdf/doi/10.1021/acs.chemrev.6c00202/68805793/acs.chemrev.6c00202.pdf by guest on 10 October 2026

Enabling a Wide Anti-solvent Time Window. *Adv. Funct. Mater.* **2024**, *34* (49), 2408973.
(267) Kwak, D.-H.; Cho, S.-B.; Li, C.-X.; Choi, Y.-N.; Park, I.-K. Multifunctional FA-Triflate Treatment for Efficiency and Reliability Enhancements of Quasi-2D Perovskite Light-Emitting Diodes. *Adv. Funct. Mater.* **2025**, *35* (23), 2422368.
(268) Han, P.; Han, Q.; Zhang, R.; Wang, D.; Zhang, Y. Synchronous Optimization via Multifunctional Small Molecular Salt for Efficient Quasi-2D Pure Green Perovskite Light-Emitting Diodes. *Adv. Funct. Mater.* **2026**, *36* (7), No. e13530.
(269) Qi, H.; Tong, Y.; Zhang, X.; Wang, H.; Zhang, L.; Chen, Y.; Wang, Y.; Shang, J.; Wang, K.; Wang, H. Homogenizing Energy Landscape for Efficient and Spectrally Stable Blue Perovskite Light-Emitting Diodes. *Adv. Mater.* **2024**, *36* (46), 2409319.
(270) Liu, H.; Gong, M.; Li, W.; Zeng, X.; Meng, C.; Luo, J.; Yang, W.; Zhang, S. Holistic Synergistic Modulation for Efficient Blue Quasi-2D Perovskite Light-Emitting Diodes. *ACS Appl. Mater. Interfaces* **2025**, *17* (33), 47141−47152.
(271) Seop Shin, Y.; Jin Yoon, Y.; Hyeon Kweon, S.; Hak Oh, S.; Beom Park, C.; Yuk, D.; Song, T.; Geon Son, J.; Seo, J.; Lee, W.; Kyu Kwak, S.; Kim, G.-H.; Young Kim, J. Controlling the Formation Energy of Perovskite Phase via Surface Polarity of Substrate for Efficient Pure-Blue Light-Emitting Diodes. *Chem. Eng. J.* **2023**, *464*, 142707.
(272) Ren, Z.; Xiao, X.; Ma, R.; Lin, H.; Wang, K.; Sun, X. W.; Choy, W. C. H. Hole Transport Bilayer Structure for Quasi-2D Perovskite Based Blue Light-Emitting Diodes with High Brightness and Good Spectral Stability. *Adv. Funct. Mater.* **2019**, *29* (43), 1905339.
(273) Xu, L.; Wu, Z.; Jiang, C.; Liu, M.; Li, B.; Lin, H.; Liu, W.; Peng, H.; Luo, C. Low-Dimensional Phase Distribution of Quasi-2D Perovskites Induced by Interfacial Effect Enables Efficient Blue Light-Emitting Diodes. *Adv. Opt. Mater.* **2024**, *12* (4), 2301615.
(274) Dong, W.; Zhang, X.; Yang, F.; Zeng, Q.; Yin, W.; Zhang, W.; Wang, H.; Yang, X.; Kershaw, S. V.; Yang, B.; Rogach, A. L.; Zheng, W. Amine-Terminated Carbon Dots Linking Hole Transport Layer and Vertically Oriented Quasi-2D Perovskites through Hydrogen Bonds Enable Efficient LEDs. *ACS Nano* **2022**, *16* (6), 9679−9690.
(275) Shen, C.; Wang, H.; Liang, X.; Chen, H.; Cai, B.; Wei, Y.; Hu, S.; Luo, Y.; Zhang, F.; Xu, Q.; Hou, L.; Zhang, J. Simultaneous Interfacial Modification and Crystallization Regulation for High-Performance Pure-Blue Quasi-2D Perovskite Light-Emitting Diodes. *ACS Energy Lett.* **2025**, *10* (8), 3638−3646.
(276) Kong, L.; Luo, Y.; Turyanska, L.; Zhang, T.; Zhang, Z.; Xing, G.; Yang, Y.; Zhang, C.; Yang, X. A Spacer Cation Assisted Nucleation and Growth Strategy Enables Efficient and High-Luminance Quasi-2D Perovskite LEDs. *Adv. Funct. Mater.* **2023**, *33* (2), 2209186.
(277) Chu, Z.; Zhang, W.; Jiang, J.; Qu, Z.; Ma, F.; Zhao, Y.; Chu, X.; Shen, Y.; Li, Y.; Yin, Z.; Zhang, X.; You, J. Blue Light-Emitting Diodes Based on Quasi-Two-Dimensional Perovskite with Efficient Charge Injection and Optimized Phase Distribution via an Alkali Metal Salt. *Nat. Electron.* **2023**, *6* (5), 360−369.
(278) Dong, J.; Yang, W.; Cho, K.; Jung, J. H.; Zhou, H.; Yoon, E.; Chen, H.; Lee, H.-D.; Jo, S. H.; Park, J.-M.; Zeng, Q.; Long, T.; Jang, K. Y.; Chang, S. E.; Park, C.-Y.; Sung, M.-J.; Kim, J. S.; Kim, H.; Song, D.; Xu, Z.; Park, J.; Sun, J.-Y.; Lee, T.-W. Interfacial Decoupling Layer Enabled Low-n Phase Enrichment for Blue Quasi-2D Perovskites. *ACS Energy Lett.* **2024**, *9* (12), 5879−5887.
(279) Tang, J.; Zhang, G.; Wang, C.; Deng, L.; Zhu, X.; Yu, H.; Wang, K.; Li, J. Investigation of the Role of K2SO4 Electrolyte in Hole Transport Layer for Efficient Quasi-2D Perovskite Light-Emitting Diodes. *J. Phys. Chem. Lett.* **2024**, *15* (4), 1112−1120.
(280) Cao, L.-X.; Shen, Y.; Zhang, K.; Su, Z.-H.; Feng, S.-C.; Hu, X.-M.; Zhang, Y.-H.; Wang, B.-F.; Li, Y.-Y.; Gao, X.; Wang, W.-J.; Kera, S.; Ueno, N.; Li, Y.-Q.; Tang, J.-X. In Situ Interface Reaction Enables Efficient Deep-Blue Perovskite Light-Emitting Diodes. *Angew. Chem., Int. Ed.* **2025**, *64* (39), No. e202513617.
(281) Dong, J.; Lu, F.; Wang, J.; Zhang, Y.; Ma, X.; Zhou, J.; Han, D.; Zang, Z.; Wang, N. Perovskite Light-Emitting Diodes with Low Roll-off Efficiency via Interfacial Ionic Immobilization. *Chem. Eng. J.* **2022**, *429*, 132347.
(282) Wang, H.; Zhang, B.; Wang, B.; Bai, S.; Cheng, L.; Hu, Y.; Lu, S. Efficient Quasi-2D Perovskite Based Blue Light-Emitting Diodes with Carbon Dots Modified Hole Transport Layer. *Nano Lett.* **2024**, *24* (28), 8702−8708.
(283) Ding, S.; Wang, Q.; Gu, W.; Tang, Z.; Zhang, B.; Wu, C.; Zhang, X.; Chen, H.; Zhang, X.; Cao, R.; Chen, T.; Qian, L.; Xiang, C. Phase Dimensions Resolving of Efficient and Stable Perovskite Light-Emitting Diodes at High Brightness. *Nat. Photonics* **2024**, *18* (4), 363−370.
(284) Wu, X.; Sun, S.; Song, T.; Zhang, X.; Wang, C.; Yang, Y.; Wang, S.; Zhong, H. Revealing the Vertical Structure of In-Situ Fabricated Perovskite Nanocrystals Films toward Efficient Pure Red Light-Emitting Diodes. *Fundam. Res.* **2024**, *4* (2), 362−368.
(285) Liu, Y.; Yu, Z.; Chen, S.; Park, J. H.; Jung, E. D.; Lee, S.; Kang, K.; Ko, S.-J.; Lim, J.; Song, M. H.; Xu, B.; Snaith, H. J.; Park, S. H.; Lee, B. R. Boosting the Efficiency of Quasi-2D Perovskites Light-Emitting Diodes by Using Encapsulation Growth Method. *Nano Energy* **2021**, *80*, 105511.
(286) Pang, P.; Zeng, G.; Mao, Y.; Wang, B.; Zhang, Z.; Liao, J.; Deng, X.; Chen, J.; Ma, D.; Xing, G. Improving Performance of Quasi-2D Perovskite Light-Emitting Diodes by Solvent Atmospheric Post-Treatment. *ACS Appl. Mater. Interfaces* **2025**, *17* (29), 42108−42117.
(287) Xia, Y.; Song, B.; Zhang, Z.; Wang, K.-L.; Li, Y.-H.; Li, N.; Chen, C.-H.; Chen, J.; Xing, G.; Wang, Z.-K. Vertically Concentrated Quantum Wells Enabling Highly Efficient Deep-Blue Perovskite Light-Emitting Diodes. *Angew. Chem., Int. Ed.* **2024**, *63* (22), No. e202403739.
(288) Septianto, R. D.; Miranti, R.; Kikitsu, T.; Hikima, T.; Hashizume, D.; Matsushita, N.; Iwasa, Y.; Bisri, S. Z. Enabling Metallic Behaviour in Two-Dimensional Superlattice of Semiconductor Colloidal Quantum Dots. *Nat. Commun.* **2023**, *14*, 2670.
(289) Protesescu, L.; Yakunin, S.; Bodnarchuk, M. I.; Krieg, F.; Caputo, R.; Hendon, C. H.; Yang, R. X.; Walsh, A.; Kovalenko, M. V. Nanocrystals of Cesium Lead Halide Perovskites (CsPbX3, X = Cl, Br, and I): Novel Optoelectronic Materials Showing Bright Emission with Wide Color Gamut. *Nano Lett.* **2015**, *15* (6), 3692−3696.
(290) Kim, Y.-H.; Lee, G.-H.; Kim, Y.-T.; Wolf, C.; Yun, H. J.; Kwon, W.; Park, C. G.; Lee, T.-W. High Efficiency Perovskite Light-Emitting Diodes of Ligand-Engineered Colloidal Formamidinium Lead Bromide Nanoparticles. *Nano Energy* **2017**, *38*, 51−58.
(291) Wang, Y. K.; Wan, H.; Teale, S.; Grater, L.; Zhao, F.; Zhang, Z.; Duan, H. W.; Imran, M.; Wang, S. D.; Hoogland, S.; Liao, L. S. Long-Range Order Enabled Stability in Quantum Dot Light-Emitting Diodes. *Nature* **2024**, *629* (8012), 586−591.
(292) Kagan, C. R.; Lifshitz, E.; Sargent, E. H.; Talapin, D. V. Building Devices from Colloidal Quantum Dots. *Science* **2016**, *353* (6302), aac5523.
(293) Whitham, K.; Yang, J.; Savitzky, B. H.; Kourkoutis, L. F.; Wise, F.; Hanrath, T. Charge Transport and Localization in Atomically Coherent Quantum Dot Solids. *Nat. Mater.* **2016**, *15* (5), 557−563.
(294) Talapin, D. V.; Lee, J.-S.; Kovalenko, M. V.; Shevchenko, E. V. Prospects of Colloidal Nanocrystals for Electronic and Optoelectronic Applications. *Chem. Rev.* **2010**, *110* (1), 389−458.
(295) Li, H.; Zhang, J.; Wen, W.; Zhao, Y.; Gao, H.; Ji, B.; Wang, Y.; Jiang, L.; Wu, Y. Highly Efficient Light-Emitting Diodes via Self-Assembled InP Quantum Dots. *Nat. Commun.* **2025**, *16* (1), 4257.
(296) Imran, M.; Caligiuri, V.; Wang, M.; Goldoni, L.; Prato, M.; Krahne, R.; De Trizio, L.; Manna, L. Benzoyl Halides as Alternative Precursors for the Colloidal Synthesis of Lead-Based Halide Perovskite Nanocrystals. *J. Am. Chem. Soc.* **2018**, *140* (7), 2656−2664.
(297) Dutta, A.; Behera, R. K.; Pal, P.; Baitalik, S.; Pradhan, N. Near-Unity Photoluminescence Quantum Efficiency for All CsPbX3 (X = Cl, Br, and I) Perovskite Nanocrystals: A Generic Synthesis Approach. *Angew. Chem., Int. Ed.* **2019**, *58* (17), 5552−5556.
(298) Kim, D.-H.; Woo, S.-J.; Huelmo, C. P.; Park, M.-H.; Schankler, A. M.; Dai, Z.; Heo, J.-M.; Kim, S.; Reuveni, G.; Kang, S.; Kim, J. S.; Yun, H. J.; Park, J.; Park, J.; Yaffe, O.; Rappe, A. M.; Lee, T.-W. Surface-Binding Molecular Multipods Strengthen the Halide Perovskite Lattice and Boost Luminescence. *Nat. Commun.* **2024**, *15*, 6245.

Downloaded from pubs.acs.org/chreav/article-pdf/doi/10.1021/acs.chemrev.6c00202/68805793/acs.chemrev.6c00202.pdf by guest on 10 October 2026

(299) Zhang, F.; Zhong, H.; Chen, C.; Wu, X.; Hu, X.; Huang, H.; Han, J.; Zou, B.; Dong, Y. Brightly Luminescent and Color-Tunable Colloidal CH3NH3PbX3 (X = Br, I, Cl) Quantum Dots: Potential Alternatives for Display Technology. *ACS Nano* **2015**, *9* (4), 4533−4542.
(300) Kim, J. I.; Zeng, Q.; Park, S.; Lee, H.; Park, J.; Kim, T.; Lee, T.-W. Strategies to Extend the Lifetime of Perovskite Downconversion Films for Display Applications. *Adv. Mater.* **2023**, *35*, 2209784.
(301) Abe, H.; Uwano, M.; Kobayashi, R.; Narazaki, K.; Akiyama, T.; Ito, Y.; Yokota, D.; Oto, T.; Nishitsuji, S.; Yamakado, R.; Chiba, T. Boosting the Stability of FAPbI3 Perovskite Nanocrystal Near-Infrared Light-Emitting Diodes with Aromatic Ligands and Organic Host Dispersion. *Small* **2025**, *21* (31), 2501159.
(302) Hazarika, A.; Zhao, Q.; Gaulding, E. A.; Christians, J. A.; Dou, B.; Marshall, A. R.; Moot, T.; Berry, J. J.; Johnson, J. C.; Luther, J. M. Perovskite Quantum Dot Photovoltaic Materials beyond the Reach of Thin Films: Full-Range Tuning of A-Site Cation Composition. *ACS Nano* **2018**, *12* (10), 10327−10337.
(303) Li, H.; Lu, W.; Zhao, G.; Song, B.; Dong, W.; Han, G. Evolution and Mechanism of Cesium Lead Bromide Nanostructures in Oleylamine-Rich System by Hot-Injection Method. *Adv. Mater. Interfaces* **2023**, *10* (1), 2201916.
(304) De Roo, J.; Ibáñez, M.; Geiregat, P.; Nedelcu, G.; Walravens, W.; Maes, J.; Martins, J. C.; Van Driessche, I.; Kovalenko, M. V.; Hens, Z. Highly Dynamic Ligand Binding and Light Absorption Coefficient of Cesium Lead Bromide Perovskite Nanocrystals. *ACS Nano* **2016**, *10*, 2071.
(305) Jang, K. Y.; Hwang, S. Y.; Woo, S.-J.; Yoon, E.; Park, C.-Y.; Kim, S. Y.; Kim, D.-H.; Kim, H.; Park, J.; Sargent, E. H.; Lee, T.-W. Efficient Deep-Blue Light-Emitting Diodes Through Decoupling of Colloidal Perovskite Quantum Dots. *Adv. Mater.* **2024**, *36*, 2404856.
(306) Sun, X.; Yuan, L.; Liu, Y.; Shi, G.; Wang, Y.; Liu, C.; Zhang, X.; Zhao, Y.; Zhao, C.; Ma, M.; Shen, B.; Wang, Y.; Shen, Q.; Liu, Z.; Ma, W. Diffusion-Mediated Synthesis of High-Quality Organic-Inorganic Hybrid Perovskite Nanocrystals. *Nat. Synth.* **2025**, *4* (2), 167−176.
(307) Almeida, G.; Ashton, O. J.; Goldoni, L.; Maggioni, D.; Petralanda, U.; Mishra, N.; Akkerman, Q. A.; Infante, I.; Snaith, H. J.; Manna, L. The Phosphine Oxide Route toward Lead Halide Perovskite Nanocrystals. *J. Am. Chem. Soc.* **2018**, *140* (44), 14878−14886.
(308) Aldeen, T. S.; Sanvordenker, S.; Korgel, B. A. Rapid Synthesis of Fluorescent Perovskite CsPbI3 Nanocrystals in Open Air at Room Temperature. *J. Phys. Chem. C* **2025**, *129* (46), 20632−20640.
(309) Wang, T.; Li, X.; Fang, T.; Wang, S.; Song, J. Room-Temperature Synthesis of Perovskite-Phase CsPbI3 Nanocrystals for Optoelectronics via a Ligand-Mediated Strategy. *Chem. Eng. J.* **2021**, *418*, 129361.
(310) Akkerman, Q. A.; Nguyen, T. P. T.; Boehme, S. C.; Montanarella, F.; Dirin, D. N.; Wechsler, P.; Beiglböck, F.; Rainò, G.; Erni, R.; Katan, C.; Even, J.; Kovalenko, M. V. Controlling the Nucleation and Growth Kinetics of Lead Halide Perovskite Quantum Dots. *Science* **2022**, *377* (6613), 1406−1412.
(311) Kim, Y.-H.; Wolf, C.; Kim, Y.-T.; Cho, H.; Kwon, W.; Do, S.; Sadhanala, A.; Park, C. G.; Rhee, S.-W.; Im, S. H.; Friend, R. H.; Lee, T.-W. Highly Efficient Light-Emitting Diodes of Colloidal Metal-Halide Perovskite Nanocrystals beyond Quantum Size. *ACS Nano* **2017**, *11* (7), 6586−6593.
(312) Levchuk, I.; Osvet, A.; Tang, X.; Brandl, M.; Perea, J. D.; Hoegl, F.; Matt, G. J.; Hock, R.; Batentschuk, M.; Brabec, C. J. Brightly Luminescent and Color-Tunable Formamidinium Lead Halide Perovskite FAPbX3 (X = Cl, Br, I) Colloidal Nanocrystals. *Nano Lett.* **2017**, *17* (5), 2765−2770.
(313) Pan, A.; He, B.; Fan, X.; Liu, Z.; Urban, J. J.; Alivisatos, A. P.; He, L.; Liu, Y. Insight into the Ligand-Mediated Synthesis of Colloidal CsPbBr3 Perovskite Nanocrystals: The Role of Organic Acid, Base, and Cesium Precursors. *ACS Nano* **2016**, *10* (8), 7943−7954.
(314) Kumar, S.; Jagielski, J.; Kallikounis, N.; Kim, Y.-H.; Wolf, C.; Jenny, F.; Tian, T.; Hofer, C. J.; Chiu, Y.-C.; Stark, W. J.; Lee, T.-W.; Shih, C.-J. Ultrapure Green Light-Emitting Diodes Using Two-Dimensional Formamidinium Perovskites: Achieving Recommendation 2020 Color Coordinates. *Nano Lett.* **2017**, *17* (9), 5277−5284.
(315) Li, J.; Xu, L.; Wang, T.; Song, J.; Chen, J.; Xue, J.; Dong, Y.; Cai, B.; Shan, Q.; Han, B.; Zeng, H. 50-Fold EQE Improvement up to 6.27% of Solution-Processed All-Inorganic Perovskite CsPbBr3 QLEDs via Surface Ligand Density Control. *Adv. Mater.* **2017**, *29* (5), 1603885.
(316) Hoshi, K.; Chiba, T.; Sato, J.; Hayashi, Y.; Takahashi, Y.; Ebe, H.; Ohisa, S.; Kido, J. Purification of Perovskite Quantum Dots Using Low-Dielectric-Constant Washing Solvent "Diglyme" for Highly Efficient Light-Emitting Devices. *ACS Appl. Mater. Interfaces* **2018**, *10* (29), 24607−24612.
(317) Vighnesh, K.; Wang, S.; Liu, H.; Rogach, A. L. Hot-Injection Synthesis Protocol for Green-Emitting Cesium Lead Bromide Perovskite Nanocrystals. *ACS Nano* **2022**, *16* (12), 19618−19625.
(318) Dong, Y.; Wang, Y.-K.; Yuan, F.; Johnston, A.; Liu, Y.; Ma, D.; Choi, M.-J.; Chen, B.; Chekini, M.; Baek, S.-W.; Sagar, L. K.; Fan, J.; Hou, Y.; Wu, M.; Lee, S.; Sun, B.; Hoogland, S.; Quintero-Bermudez, R.; Ebe, H.; Todorovic, P.; Dinic, F.; Li, P.; Kung, H. T.; Saidaminov, M. I.; Kumacheva, E.; Spiecker, E.; Liao, L.-S.; Voznyy, O.; Lu, Z.-H.; Sargent, E. H. Bipolar-Shell Resurfacing for Blue LEDs Based on Strongly Confined Perovskite Quantum Dots. *Nat. Nanotechnol.* **2020**, *15* (8), 668−674.
(319) Li, M.; Wang, J.; Yao, J.; Wang, S.; Xu, L.; Song, J. Trade-Off Between Efficiency and Stability of CsPbBr3 Perovskite Quantum Dot-Based Light-Emitting Diodes by Optimized Passivation Ligands for Br/Pb. *Adv. Funct. Mater.* **2024**, *34* (3), 2308341.
(320) Liu, M.; Wan, Q.; Wang, H.; Carulli, F.; Sun, X.; Zheng, W.; Kong, L.; Zhang, Q.; Zhang, C.; Zhang, Q.; Brovelli, S.; Li, L. Suppression of Temperature Quenching in Perovskite Nanocrystals for Efficient and Thermally Stable Light-Emitting Diodes. *Nat. Photonics* **2021**, *15* (5), 379−385.
(321) Chiba, T.; Hayashi, Y.; Ebe, H.; Hoshi, K.; Sato, J.; Sato, S.; Pu, Y.-J.; Ohisa, S.; Kido, J. Anion-Exchange Red Perovskite Quantum Dots with Ammonium Iodine Salts for Highly Efficient Light-Emitting Devices. *Nat. Photonics* **2018**, *12* (11), 681−687.
(322) Pan, J.; Quan, L. N.; Zhao, Y.; Peng, W.; Murali, B.; Sarmah, S. P.; Yuan, M.; Sinatra, L.; Alyami, N. M.; Liu, J.; Yassitepe, E.; Yang, Z.; Voznyy, O.; Comin, R.; Hedhili, M. N.; Mohammed, O. F.; Lu, Z. H.; Kim, D. H.; Sargent, E. H.; Bakr, O. M. Highly Efficient Perovskite-Quantum-Dot Light-Emitting Diodes by Surface Engineering. *Adv. Mater.* **2016**, *28* (39), 8718−8725.
(323) Stelmakh, A.; Aebli, M.; Baumketner, A.; Kovalenko, M. V. On the Mechanism of Alkylammonium Ligands Binding to the Surface of CsPbBr3 Nanocrystals. *Chem. Mater.* **2021**, *33* (15), 5962−5973.
(324) Nong, Y.; Yao, J.; Li, J.; Xu, L.; Yang, Z.; Li, C.; Song, J. Boosting External Quantum Efficiency of Blue Perovskite QLEDs Exceeding 23% by Trifluoroacetate Passivation and Mixed Hole Transportation Design. *Adv. Mater.* **2024**, *36* (27), 2402325.
(325) Yang, D.; Li, X.; Zhou, W.; Zhang, S.; Meng, C.; Wu, Y.; Wang, Y.; Zeng, H. CsPbBr3 Quantum Dots 2.0: Benzenesulfonic Acid Equivalent Ligand Awakens Complete Purification. *Adv. Mater.* **2019**, *31* (30), 1900767.
(326) Jin, X.; Miao, Y.; Dong, J.; Wang, J.; Lu, Q.; Zhao, M.; Xu, B.; Guo, J. Trap States Engineering toward All-Inorganic CsPbBr3 Perovskite Nanocrystals for Highly Efficient Light-Emitting Diodes. *J. Mater. Chem. C* **2023**, *11* (29), 9996−10003.
(327) Li, D.; Lyu, B.; Sun, J.; Xiong, Q.; Zhu, H.; Jiang, Z.; Zhang, D.; Liu, C.; Choy, W. C. H. Ligands Optimization Governed by Solubility Principles for Pure Blue Emission in Mixed-Halide Perovskite LEDs. *ACS Energy Lett.* **2024**, *9* (7), 3261−3268.
(328) Zhao, H.; Chen, H.; Bai, S.; Kuang, C.; Luo, X.; Teng, P.; Yin, C.; Zeng, P.; Hou, L.; Yang, Y.; Duan, L.; Gao, F.; Liu, M. High-Brightness Perovskite Light-Emitting Diodes Based on FAPbBr3 Nanocrystals with Rationally Designed Aromatic Ligands. *ACS Energy Lett.* **2021**, *6* (7), 2395−2403.
(329) Zhou, W.; Ham, S.; Lee, H. B.; Ko, K.-J.; Luo, J.; He, S.; Lee, J.-H.; Kang, J.-W. Tuning Transition Dipole Moment Alignment via Bifunctional Ligands in Perovskite Nanocrystal Light-Emitting Diodes. *Adv. Mater.* **2026**, *38* (8), No. e17210.

Downloaded from pubs.acs.org/chreav/article-pdf/doi/10.1021/acs.chemrev.6c00202/68805793/acs.chemrev.6c00202.pdf by guest on 10 October 2026

(330) Fiuza-Maneiro, N.; Ye, J.; Sharma, S. K.; Chakraborty, S.; Gómez-Graña, S.; Hoye, R. L. Z.; Polavarapu, L. Unlocking Brightness in CsPbCl3 Perovskite Nanocrystals: Screening Ligands and Metal Halides for Effective Deep Trap Passivation. *ACS Energy Lett.* **2025**, *10* (4), 1623−1632.
(331) Shamsi, J.; Kubicki, D.; Anaya, M.; Liu, Y.; Ji, K.; Frohna, K.; Grey, C. P.; Friend, R. H.; Stranks, S. D. Stable Hexylphosphonate-Capped Blue-Emitting Quantum-Confined CsPbBr3 Nanoplatelets. *ACS Energy Lett.* **2020**, *5* (6), 1900−1907.
(332) Zhang, B.; Goldoni, L.; Zito, J.; Dang, Z.; Almeida, G.; Zaccaria, F.; de Wit, J.; Infante, I.; De Trizio, L.; Manna, L. Alkyl Phosphonic Acids Deliver CsPbBr3 Nanocrystals with High Photoluminescence Quantum Yield and Truncated Octahedron Shape. *Chem. Mater.* **2019**, *31* (21), 9140−9147.
(333) Wang, R.; Zhao, J.; Ma, J.; Lu, C.; Yu, Z.; Tu, G.; Zhang, J. Yttrium Cation Doping and Phenylphosphonic Acid Passivation for Pure-Red Perovskite Light-Emitting Diodes. *ACS Energy Lett.* **2024**, *9* (9), 4699−4707.
(334) Saleem, M. I.; He, S.; Kim, S. H.; Kang, J.-W.; Lee, J.-H. Perovskite Nanocrystals Passivated by Aromatic Phosphonic Acid for High-Performance Light-Emitting Diodes. *J. Mater. Chem. C* **2024**, *12* (42), 17289−17297.
(335) Feng, Y.; He, Y.; Zhu, M.; Li, H.; Cao, Q.; Huang, H.; He, H.; Ye, Z.; Dai, X. Surface Compensation Principles of Soft-Lattice Nanocrystals toward High-Performance Electroluminescence. *Adv. Mater.* **2025**, *37* (43), No. e10886.
(336) Li, H.; Feng, Y.; Zhu, M.; Gao, Y.; Fan, C.; Cui, Q.; Cai, Q.; Yang, K.; He, H.; Dai, X.; Huang, J.; Ye, Z. Nanosurface-Reconstructed Perovskite for Highly Efficient and Stable Active-Matrix Light-Emitting Diode Display. *Nat. Nanotechnol.* **2024**, *19* (5), 638−645.
(337) Shynkarenko, Y.; Bodnarchuk, M. I.; Bernasconi, C.; Berezovska, Y.; Verteletskyi, V.; Ochsenbein, S. T.; Kovalenko, M. V. Direct Synthesis of Quaternary Alkylammonium-Capped Perovskite Nanocrystals for Efficient Blue and Green Light-Emitting Diodes. *ACS Energy Lett.* **2019**, *4* (11), 2703−2711.
(338) Li, H.; Hua, Y.; Wang, X.; Ge, C.; Wang, Z.; Song, Y.; Li, X.; Wang, A.; Yang, Y.; Zhou, K.; Dong, W.; Zheng, W.; Zhang, L.; Zhang, X.; Dong, Q. Highly Stable O-Tolylbiguanide-CsPbI3 Quantum Dots and Light-Emitting Diodes by Synergistic Supramolecular Passivation. *Adv. Funct. Mater.* **2024**, *34* (23), 2311554.
(339) Feng, Y.; Zhu, M.; Cao, Q.; Li, H.; Zhu, X.; Lyu, X.; Dai, X.; He, H.; Ye, Z. P-π Conjugated L-Type Ligand for Pure-Red Perovskite Light-Emitting Diodes. *ACS Energy Lett.* **2024**, *9* (3), 1125−1132.
(340) Chen, J.; Chen, S.; Liu, X.; Zhu, D.; Cai, B.; Luo, X.; Feng, W.; Cheng, Y.; Xiong, Y.; Du, J.; Li, Z.; Zhang, D.; Duan, L.; Ma, D. Molecule-Induced Ripening Control in Perovskite Quantum Dots for Efficient and Stable Light-Emitting Diodes. *Sci. Adv.* **2025**, *11* (11), No. eads7159.
(341) Zhang, J.; Cai, B.; Zhou, X.; Yuan, F.; Yin, C.; Wang, H.; Chen, H.; Ji, X.; Liang, X.; Shen, C.; Wang, Y.; Ma, Z.; Qing, J.; Shi, Z.; Hu, Z.; Hou, L.; Zeng, H.; Bai, S.; Gao, F. Ligand-Induced Cation-π Interactions Enable High-Efficiency, Bright, and Spectrally Stable Rec. 2020 Pure-Red Perovskite Light-Emitting Diodes. *Adv. Mater.* **2023**, *35* (45), 2303938.
(342) Chen, J.; Liu, X.; Cai, B.; Cheng, Y.; Wen, H.; Zhu, D.; Xiong, Y.; Dai, L.; Yan, X.; Xiang, B.; Luo, X.; Feng, W.; Du, J.; Dong, S.; Shan, Q.; Chen, S.; Zeng, H.; Xiong, Q.; Duan, L.; Ma, D. Lattice-Matched Molecular-Anchor Design for High-Performance Perovskite Quantum Dot Light-Emitting Diodes. *Nat. Commun.* **2025**, *16* (1), 8201.
(343) Murray, C. B.; Kagan, C. R.; Bawendi, M. G. Self-Organization of CdSe Nanocrystallites into Three-Dimensional Quantum Dot Superlattices. *Science* **1995**, *270*, 1335−1338.
(344) Nagaoka, Y.; Zhu, H.; Eggert, D.; Chen, O. Single-Component Quasicrystalline Nanocrystal Superlattices through Flexible Polygon Tiling Rule. *Science* **2018**, *362*, 1396−1400.
(345) Toso, S.; Baranov, D.; Filippi, U.; Giannini, C.; Manna, L. Collective Diffraction Effects in Perovskite Nanocrystal Superlattices. *Acc. Chem. Res.* **2023**, *56* (1), 66−76.
(346) Lee, J. S.; Kovalenko, M. V.; Huang, J.; Chung, D. S.; Talapin, D. V. Band-like Transport, High Electron Mobility and High Photoconductivity in All-Inorganic Nanocrystal Arrays. *Nat. Nanotechnol.* **2011**, *6* (6), 348−352.
(347) Blach, D. D.; Lumsargis-Roth, V. A.; Chuang, C.; Clark, D. E.; Deng, S.; Williams, O. F.; Li, C. W.; Cao, J.; Huang, L. Environment-Assisted Quantum Transport of Excitons in Perovskite Nanocrystal Superlattices. *Nat. Commun.* **2025**, *16*, 1270.
(348) Zeng, Q.; Zhang, X.; Bing, Q.; Xiong, Y.; Yang, F.; Liu, H.; Liu, J. Y.; Zhang, H.; Zheng, W.; Rogach, A. L.; Yang, B. Surface Stabilization of Colloidal Perovskite Nanocrystals via Multi-Amine Chelating Ligands. *ACS Energy Lett.* **2022**, *7* (6), 1963−1970.
(349) Zeng, Q.; Zhao, Y.; Park, S.; Zhou, H.; Shim, H.-J.; Li, T.; Ryu, J.; Sung, M.-J.; Chua, X. W.; Yoon, E.; Lewis, B. A. I.; Woo, S.-J.; Forzatti, M.; Kim, M. J.; Kim, E. A.; Dai, L.; Jang, J.; Tang, Y.; Kweon, J. J.; Chen, H.; Jang, K. Y.; Kim, D.-H.; Jeong, W. J.; Kim, J. S.; Lee, H.; Lim, K.; Cho, S.-Y.; Park, C. B.; Lee, S. K.; Kim, M.; Bolink, H. J.; Hu, B.; Walsh, A.; Stranks, S. D.; Lee, T.-W. A Hierarchical Shell Locks and Stabilizes Perovskite Nanocrystals with Near-Unity Quantum Yield. *Science* **2026**, *391* (6782), No. eady1370.
(350) Huang, Q.; Yin, W.; Gao, B.; Zeng, Q.; Yao, D.; Zhang, H.; Zhao, Y.; Zheng, W.; Zhang, J.; Yang, X.; Zhang, X.; Rogach, A. L. Enhancing Crystal Integrity and Structural Rigidity of CsPbBr3 Nanoplatelets to Achieve a Narrow Color-Saturated Blue Emission. *Light Sci. Appl.* **2024**, *13*, 111.
(351) Bera, S.; Behera, R. K.; Pradhan, N. α-Halo Ketone for Polyhedral Perovskite Nanocrystals: Evolutions, Shape Conversions, Ligand Chemistry, and Self-Assembly. *J. Am. Chem. Soc.* **2020**, *142* (49), 20865−20874.
(352) Rainò, G.; Becker, M. A.; Bodnarchuk, M. I.; Mahrt, R. F.; Kovalenko, M. V.; Stöferle, T. Superfluorescence from Lead Halide Perovskite Quantum Dot Superlattices. *Nature* **2018**, *563* (7733), 671−675.
(353) Zhou, C.; M. Pina, J.; Zhu, T.; H. Parmar, D.; Chang, H.; Yu, J.; Yuan, F.; Bappi, G.; Hou, Y.; Zheng, X.; Abed, J.; Chen, H.; Zhang, J.; Gao, Y.; Chen, B.; Wang, Y.-K.; Chen, H.; Zhang, T.; Hoogland, S.; Saidaminov, M. I.; Sun, L.; Bakr, O. M.; Dong, H.; Zhang, L.; H. Sargent, E. Quantum Dot Self-Assembly Enables Low-Threshold Lasing. *Adv. Sci.* **2021**, *8*, 2101125.
(354) Tong, Y.; Yao, E. P.; Manzi, A.; Bladt, E.; Wang, K.; Döblinger, M.; Bals, S.; Müller-Buschbaum, P.; Urban, A. S.; Polavarapu, L.; Feldmann, J. Spontaneous Self-Assembly of Perovskite Nanocrystals into Electronically Coupled Supercrystals: Toward Filling the Green Gap. *Adv. Mater.* **2018**, *30*, 1801117.
(355) Jagielski, J.; Solari, S. F.; Jordan, L.; Scullion, D.; Blülle, B.; Li, Y. T.; Krumeich, F.; Chiu, Y. C.; Ruhstaller, B.; Santos, E. J. G.; Shih, C. J. Scalable Photonic Sources Using Two-Dimensional Lead Halide Perovskite Superlattices. *Nat. Commun.* **2020**, *11*, 387.
(356) Kumar, S.; Marcato, T.; Krumeich, F.; Li, Y. T.; Chiu, Y. C.; Shih, C. J. Anisotropic Nanocrystal Superlattices Overcoming Intrinsic Light Outcoupling Efficiency Limit in Perovskite Quantum Dot Light-Emitting Diodes. *Nat. Commun.* **2022**, *13*, 2106.
(357) Ye, J.; Ren, A.; Dai, L.; Baikie, T. K.; Guo, R.; Pal, D.; Gorgon, S.; Heger, J. E.; Huang, J.; Sun, Y.; Arul, R.; Grimaldi, G.; Zhang, K.; Shamsi, J.; Huang, Y. T.; Wang, H.; Wu, J.; Koenderink, A. F.; Torrente Murciano, L.; Schwartzkopf, M.; Roth, S. V.; Müller-Buschbaum, P.; Baumberg, J. J.; Stranks, S. D.; Greenham, N. C.; Polavarapu, L.; Zhang, W.; Rao, A.; Hoye, R. L. Z. Direct Linearly Polarized Electroluminescence from Perovskite Nanoplatelet Superlattices. *Nat. Photonics* **2024**, *18* (6), 586−594.
(358) Li, X.; Xue, Z.; Chen, X.; Qiao, X.; Mo, G.; Bu, W.; Guan, B.; Wang, T. Printable Assemblies of Perovskite Nanocubes on Meter-Scale Panel. *Sci. Adv.* **2022**, *8*, No. eadd1559.
(359) Krieg, F.; Sercel, P. C.; Burian, M.; Andrusiv, H.; Bodnarchuk, M. I.; Stöferle, T.; Mahrt, R. F.; Naumenko, D.; Amenitsch, H.; Rainò, G.; Kovalenko, M. V. Monodisperse Long-Chain Sulfobetaine-Capped CsPbBr3Nanocrystals and Their Superfluorescent Assemblies. *ACS Cent. Sci.* **2021**, *7* (1), 135−144.

Downloaded from pubs.acs.org/chreav/article-pdf/doi/10.1021/acs.chemrev.6c00202/68805793/acs.chemrev.6c00202.pdf by guest on 10 October 2026

(360) Filippi, U.; Toso, S.; Ferreira, M. G.; Tallarini, L.; Ivanov, Y. P.; Scattarella, F.; Lauciello, S.; Haghighat, V.; Chen, H.; Landberg, M.; Divitini, G.; Wallentin, J.; Giannini, C.; Manna, L.; Baranov, D. Sinusoidal Displacement Describes Disorder in CsPbBr3 Nanocrystal Superlattices. *ACS Nano* **2026**, *20*, 3867.
(361) Zhang, C.; Zeng, Q.; Li, H.; Guo, R.; Yu, Y.; Dai, L.; Turyanska, L.; Liu, Z.; Dai, J.; Yang, Y.; Zhao, Y.; Lu, J.; Wang, L.; Kong, L.; Sum, T. C.; Wu, Y.; Lee, T.-W.; Yang, X. Pixelated Quantum-Dot Superlattice LEDs. *Nature* **2026**, *652* (8112), 1173−1180.
(362) Yang, W.; Jo, S.-H.; Tang, Y.; Park, J.; Ji, S. G.; Cho, S. H.; Hong, Y.; Kim, D.-H.; Park, J.; Yoon, E.; Zhou, H.; Woo, S.-J.; Kim, H.; Yun, H. J.; Lee, Y. S.; Kim, J. Y.; Hu, B.; Lee, T.-W. Overcoming Charge Confinement in Perovskite Nanocrystal Solar Cells. *Adv. Mater.* **2023**, *35* (39), 2304533.
(363) Zhang, M.; Hu, J.; Xi, G.; Tu, J.; Yang, Q.; Fan, L.; Lu, Y.; Sui, M.; Sun, X.; Zhang, L.; Tian, J. Colloidal Perovskite Nanocrystal Superlattice Films with Simultaneous Polarized Emission and Orderly Electric Polarity via an In Situ Surface Cross-Linking Reaction. *ACS Nano* **2025**, *19* (7), 7283−7293.
(364) Zhao, Y.; Choi, B.-H.; Kim, E.; Zeng, Q.; Lee, T.-W. Advancing Perovskite Nanocrystals for High-Resolution LED Displays. *Commun. Mater.* **2025**, *6* (1), 281.
(365) Huo, Y.; He, T.; Yang, S.; Jiang, Y.; Sun, C. Halide Perovskite Heterostructures for High-Performance Light-Emitting Diodes. *Nano-micro Lett.* **2026**, *18* (1), 185.
(366) Min, H.; Wang, N.; Chen, N.; Tong, Y.; Wang, Y.; Wang, J.; Liu, J.; Wang, S.; Wu, X.; Yang, P.; Shi, H.; Zhuo, C.; Chen, Q.; Li, J.; Zhang, D.; Lu, X.; Zhu, C.; Peng, Q.; Zhu, L.; Chang, J.; Huang, W.; Wang, J. Spin Coating Epitaxial Heterodimensional Tin Perovskites for Light-Emitting Diodes. *Nat. Nanotechnol.* **2024**, *19* (5), 632−637.
(367) Peng, J.; Xue, X.; Liu, S.; Yang, Y.; Yang, T.; Zhu, B.; Wang, X.; Zhang, H.; Xie, W.; Chen, G.; Feng, S.; Li, L.; Tai, R.; Tang, A.; Lu, H.; Ji, W. Maximizing Perovskite Electroluminescence with Ordered 3D/2D Heterojunction. *Nature* **2026**, *651*, 76.
(368) Kim, H.; Kim, J. S.; Heo, J.-M.; Pei, M.; Park, I.-H.; Liu, Z.; Yun, H. J.; Park, M.-H.; Jeong, S.-H.; Kim, Y.-H.; Park, J.-W.; Oveisi, E.; Nagane, S.; Sadhanala, A.; Zhang, L.; Kweon, J. J.; Lee, S. K.; Yang, H.; Jang, H. M.; Friend, R. H.; Loh, K. P.; Nazeeruddin, M. K.; Park, N.-G.; Lee, T.-W. Proton-Transfer-Induced 3D/2D Hybrid Perovskites Suppress Ion Migration and Reduce Luminance Overshoot. *Nat. Commun.* **2020**, *11* (1), 3378.
(369) Wei, K.; Zhou, T.; Jiang, Y.; Sun, C.; Liu, Y.; Li, S.; Liu, S.; Fu, X.; Hu, C.; Tian, S.; Yang, Y.; Fu, X.; AlMasoud, N.; Qaid, S. M. H.; Nazeeruddin, M. K.; Hsu, H.-Y.; Li, W.-D.; Kim, J. T.; Long, R.; Zhang, W.; Chen, J.; Yuan, M. Perovskite Heteroepitaxy for High-Efficiency and Stable Pure-Red LEDs. *Nature* **2025**, *638* (8052), 949−956.
(370) Cho, S.; Yun, S. H. Structure and Optical Properties of Perovskite-Embedded Dual-Phase Microcrystals Synthesized by Sonochemistry. *Commun. Chem.* **2020**, *3* (1), 15.
(371) Bai, T.; Wang, S.; Zhang, K.; Chu, C.; Sun, Y.; Yi, L. High Stability and Strong Luminescence CsPbBr3-Cs4PbBr6 Thin Films for All-Inorganic Perovskite Light-Emitting Diodes. *RSC Adv.* **2023**, *13* (35), 24413−24422.
(372) Xia, Z.; Jiang, J.; Wang, A.; An, D.; Li, Z.; Zheng, H.; Yin, Z.; He, G.; You, J.; Zhang, X. Overall Performance Improvement of Perovskite Green LEDs by CsPbBr3&Cs4PbBr6 Nanocrystals and Molecular Doping. *Adv. Mater.* **2025**, *37* (34), 2506187.
(373) Liu, S.; Jiang, H.; Wang, J.; Liu, L.; Zhou, Z.; Chen, M. Scalable Manufacturing and Precise Patterning of Perovskites for Light-Emitting Diodes. *Nanomicro Lett.* **2026**, *18* (1), 183.
(374) Luo, J.; Li, J.; Grater, L.; Guo, R.; Mohd Yusoff, Abd. R. b.; Sargent, E.; Tang, J. Vapour-Deposited Perovskite Light-Emitting Diodes. *Nat. Rev. Mater.* **2024**, *9* (4), 282−294.
(375) Lian, X.; Wang, X.; Ling, Y.; Lochner, E.; Tan, L.; Zhou, Y.; Ma, B.; Hanson, K.; Gao, H. Light Emitting Diodes Based on Inorganic Composite Halide Perovskites. *Adv. Funct. Mater.* **2019**, *29* (5), 1807345.
(376) Li, J.; Du, P.; Li, S.; Liu, J.; Zhu, M.; Tan, Z.; Hu, M.; Luo, J.; Guo, D.; Ma, L.; Nie, Z.; Ma, Y.; Gao, L.; Niu, G.; Tang, J. High-Throughput Combinatorial Optimizations of Perovskite Light-Emitting Diodes Based on All-Vacuum Deposition. *Adv. Funct. Mater.* **2019**, *29* (51), 1903607.
(377) Du, P.; Wang, L.; Li, J.; Luo, J.; Ma, Y.; Tang, J.; Zhai, T. Thermal Evaporation for Halide Perovskite Optoelectronics: Fundamentals, Progress, and Outlook. *Adv. Opt. Mater.* **2022**, *10* (4), 2101770.
(378) Lee, M. H.; Kim, J.; Han, J.; Kim, Y. I.; Kim, D. H.; Choi, Y.-J.; Song, M. H. Fabrication of Conductive Perovskite-Additive Networks Via Sequential Vacuum Deposition for Perovskite Light-Emitting Diodes. *ACS Energy Lett.* **2025**, *10* (6), 2898−2905.
(379) Li, Y.; Meng, N.; Xu, Y.; Yu, B.; Liu, J.; Cui, Y.; Wang, Z.; Ke, X.; Pan, T.; Min, X.; Chen, J.; Ma, D.; Chao, L.; Hu, Z.; Xia, Y.; Guo, Q.; Chen, Y.; Huang, W. Sequential Layer-by-Layer Deposition for High-Performance Fully Thermal-Evaporated Red Perovskite Light-Emitting Diodes. *Nat. Commun.* **2025**, *16* (1), 6908.
(380) Peng, C.; He, Z.; Zhang, F.; Wang, N.; Xu, S.; Chen, B.; He, X.; Chen, J.; Zhu, W.; Guo, R.; Wang, J.; Wang, L. Organic Intercalation Strategy for Efficient All-Evaporated Perovskite Light-Emitting Diodes. *Nat. Photonics* **2026**, *20*, 673.
(381) Park, C.-Y.; Kim, J. S.; Chua, X. W.; Yoon, E.; Jung, Y.-K.; Song, J.; Sung, M.-J.; Kim, H.-W.; Jeong, W. J.; Chang, S. E.; Park, J.; Choi, B.-H.; Kim, S.; Lee, K.-H.; Stranks, S. D.; Lee, T.-W. Halide-Site-Substituting Spacer Creates Quasi-2D Perovskites for Vapor-Deposited LEDs. *Nat. Nanotechnol.* **2026**, *21*, 1121−1129.
(382) Yan, S.; Patel, J. B.; Lee, J. E.; Elmestekawy, K. A.; Ratnasingham, S. R.; Yuan, Q.; Herz, L. M.; Noel, N. K.; Johnston, M. B. A Templating Approach to Controlling the Growth of Coevaporated Halide Perovskites. *ACS Energy Lett.* **2023**, *8* (10), 4008−4015.
(383) Chen, B.; Peng, C.; Guo, R.; He, Z.; Sun, L.; Zhang, F.; He, X.; Zeng, H.; Wang, L. Dual-Function Self-Assembled Molecules as Hole-Transport Layers for Thermally Evaporated High-Efficiency Blue Perovskite Light-Emitting Diodes. *Adv. Mater.* **2025**, *37* (3), 2411451.
(384) Song, L.; Huang, L.; Liu, Y.; Guo, X.; Geng, C.; Xu, S.; Xia, Y.; Zhang, Y.; Luan, N.; Hu, Y. Efficient Thermally Evaporated Perovskite Light-Emitting Devices via a Bilateral Interface Engineering Strategy. *J. Phys. Chem. Lett.* **2021**, *12* (26), 6165−6173.
(385) Lee, M. H.; Kim, D.; Kim, J.; Kim, D.; Yang, J.; Choi, Y.-J.; Song, M. H. Thermally Evaporated 0D/3D Perovskite Heterostructures with LiF Interlayer for Spectrally Stable Pure-Red Perovskite Light-Emitting Diodes. *ACS Mater. Lett.* **2026**, *8* (2), 628−635.
(386) Wu, Y.-J.; Chen, C.-Y.; Chuang, Y.-T.; Lin, H.-C.; Jan, P.-E.; Chen, H.-M.; Tsai, P.-H.; Li, C.-H.; Chen, B.-H.; Chen, K.; Yang, S.-D.; Lu, J.-W.; Lu, M.-Y.; Wong, K.-T.; Lin, H.-W. Efficient and Bright All-Vacuum-Deposited Perovskite Light Emitting Diode via Guanidinium Doping and an Ultrathin Lithium Bromide Interfacial Layer. *ACS Energy Lett.* **2026**, *11* (2), 1983−1992.
(387) Zhou, Y.; Peng, W.; Xiang, G.; Liu, Y.; Zhang, J.; Zhang, J.; Li, R.; Zhu, X.; Wang, H.; Zhao, Y. All-Inorganic Green Light-Emitting Diode Based on p-NiO/CsPbBr3/n-GaN Heterojunction Structure. *J. Lumin.* **2023**, *258*, 119826.
(388) Ma, Z.-Y.; Song, Y.-H.; Zhu, B.-S.; Yin, Y.-C.; Xiao, Y.; Rahman, S. U.; Ding, G.-J.; Yao, H.-B. Perovskite Light Emitting Diodes Based on Zinc Oxide Electron Transport Layers: Recent Advances and Challenges. *Adv. Opt. Mater.* **2025**, *13* (29), No. e01468.
(389) Kuang, C.; Hu, Z.; Yuan, Z.; Wen, K.; Qing, J.; Kobera, L.; Abbrent, S.; Brus, J.; Yin, C.; Wang, H.; Xu, W.; Wang, J.; Bai, S.; Gao, F. Critical Role of Additive-Induced Molecular Interaction on the Operational Stability of Perovskite Light-Emitting Diodes. *Joule* **2021**, *5* (3), 618−630.

Downloaded from pubs.acs.org/chreav/article-pdf/doi/10.1021/acs.chemrev.6c00202/68805793/acs.chemrev.6c00202.pdf by guest on 10 October 2026